

Physik Department



**Dual-Channel STED Microscope
with Pulsed Interleaved Excitation**

Dissertation

von

Heinrich Ernst Paul Grabmayr



TECHNISCHE UNIVERSITÄT MÜNCHEN

TECHNISCHE UNIVERSITÄT MÜNCHEN

Lehrstuhl für Biophysik E27

Dual-Channel STED Microscope with Pulsed Interleaved Excitation

Heinrich Ernst Paul Grabmayr

Vollständiger Abdruck der von der Fakultät für Physik der Technischen Universität München zur Erlangung des akademischen Grades eines

Doktors der Naturwissenschaften

genehmigten Dissertation.

Vorsitzender: Univ.-Prof. Dr. M. Zacharias

Prüfer der Dissertation:

1. Univ.-Prof. Dr. A. Bausch
2. Univ.-Prof. Dr. Th. Hugel

Die Dissertation wurde am 26.09.2013 bei der Technischen Universität München eingereicht und durch die Fakultät für Physik am 22.11.2013 angenommen.

Summary

The hierarchical nature of living matter has fascinated researchers for millennia. Ever more complex devices have been developed to pry into ever finer and more wondrous structures. This ongoing development led to the emergence of super-resolution fluorescence microscopy. Yet unprecedented images of living cells and biomaterials in their innate environment are obtained by that means. Thereby procured insight into structural details leads to a deeper understanding of functions and interrelations of the levels of hierarchy. One of the methods to accomplish super-resolution is termed STED microscopy. This technique achieves an increase in resolution by depleting the excited states in the outer regions of a confocally excited spot using stimulated emission.

Here, a newly developed STED microscope is described. The setup uniquely combines the possibility to quasi-simultaneously acquire one confocal and two STED channels without the need of post-processing. To that end, pulsed interleaved excitation was implemented and a time-gating device was designed to correctly discriminate between properly detected photons and cross detection photons during the acquisition process.

The polarizational state of incident light is crucial to a good signal in STED microscopy. This empirical knowledge is confirmed by a theoretical examination of the electric field vectors in the focus. Objectives with a high numerical aperture introduce axial components. These interfere destructively only with correctly orientated circular polarization. Careful alignment of circular polarization of the STED beams resulted in a decrease of the peak signal value in typical STED images by only 15% compared to confocal mode.

The resolution achieved in STED microscopy depends on the peak intensity of the beam that stimulates emission. For a large number of detected

Summary

photons, emission needs to take place as soon as possible after the end of the detector’s dead time which follows a detection event. To unite these two requirements, an ‘advanced laser platform’ is employed which emits 100 ps pulses of super-continuum light at a repetition rate of 20 MHz and a mean beam power above one watt. The combination with a fast beam scanner facilitates pixel exposure times down to 10 μ s. Therefore, an area of 5 μ m \times 5 μ m can be scanned at a pixel resolution of 50 $\frac{\text{px}}{\mu\text{m}}$ with a frame rate of nearly two hertz. With STED beam powers of 40 mW, both STED channels feature resolutions down to about 50 nm.

The high resolution achieved with the setup pose new challenges to chromatic correction. The optics induce slight chromatic aberrations which cause the co-alignment of the incident beams to deteriorate when the beam is deflected from the optical axis during scanning. After the optimization of all relevant elements, co-alignment errors are negligible for a STED image size of up to 20 μ m.

In addition to the setup itself, the combination of two advanced light microscopy techniques—these being STED and FRET—was established. Strategies for further development of this chimeric technology were identified.

Steps towards understanding processes leading to Parkinson’s and Legionnaires’ diseases were taken by investigating the structure of cytoskeletal proteins in infested cells. This aided the discovery of a yet unknown process of progression in Legionnaires’ disease.

Additionally, a deeper insight into cellular motility and shape formation was achieved by investigating reconstituted *in vitro* keratin networks.

Lastly, self assembled structures of DNA snippets were utilised to develop a novel strategy against fluorophore bleaching (PAINT-STED). Additionally, the device was employed to characterize similarly formed structures developed for synthetic nanomotility.

A route to tackle bleaching—one of the greatest hurdles in STED microscopy—has been pointed out with PAINT-STED and the field of

super-resolution microscopy is expected to benefit from its further development.

The studies presented here path the way for more investigations that profit from three-colour imaging with high spectral, spatial, and temporal resolution. The modular architecture of the setup readily facilitates an extension towards axial resolution enhancement.

Contents

Summary	i
1 Introduction	1
2 Optical microscopy of biomaterials - concepts	3
2.1 Wide field microscope	4
2.1.1 Resolution criteria	8
2.1.2 Depth of field	11
2.1.3 Contrast	11
2.2 Photophysics of fluorophores	12
2.3 Confocal microscope	16
2.3.1 Resolution	17
2.3.2 Depth of field	19
2.4 STED microscope	19
2.4.1 Depletion pattern and polarization	22
2.4.2 Resolution	26
2.4.3 Impact of STED microscopy on the life sciences	28
2.4.4 Recent developments in STED technology	29
3 Optical microscopy of biomaterials - technical aspects	31
3.1 STED setup design	31
3.1.1 Spectral design	31
3.1.2 Timing design	39
3.1.3 Beam paths	41
3.1.4 Control and acquisition electronics	45
3.2 Characterization	46
3.2.1 STED pulse timing	46

Contents

3.2.2	Polarization dependence of the donut	50
3.2.3	Time-gating	52
3.2.4	Chromatic aberration	60
3.2.5	Resolution scaling	63
3.2.6	Detection efficiency	70
3.2.7	Issues to improve on	72
4	Investigations	75
4.1	DNA based approaches to STED microscopy	75
4.1.1	DNA filaments	76
4.1.2	Infinite imaging <i>via</i> DNA-PAINT	78
4.1.2.1	Bleach rates	80
4.1.2.2	Background and contrast	84
4.1.2.3	Imager surface interaction	87
4.1.2.4	Synopsis	89
4.1.2.5	Outlook	91
4.2	STED microscopy and cytoskeletal proteins	92
4.2.1	Legionella	92
4.2.2	α -synuclein	93
4.2.3	Keratin	103
4.3	STED-FRET	104
4.3.1	FRET	105
4.3.2	Implementation	105
4.3.3	Prerequisites for doubleSTED-FRET	109
Appendix	111
A	Protocols	112
A.1	Flow chamber immobilization protocol	112
A.2	Gold bead preparation	112
A.3	Mowiol antifade fixation protocol	112
A.4	STED pulse timing	113
A.5	Chromatic aberration	113
A.6	Resolution scaling	114
A.7	Detection efficiency	114
A.8	PAINT	114

A.9	STED-FRET on actin networks	115
A.10	DNA filaments	115
B	List of dyes that have been used in the system	115
C	Alignment	116
C.1	Workflow for daily alignment	116
C.2	Workflow for big alignment	118
C.3	Workflow for alignment from scratch	119
D	Hardware	125
D.1	Intensity photodiode	125
D.2	Circular polarization analyzer	126
D.3	Timegating device	126
D.4	Counter	128
D.5	Servo microcontroller	128
E	Software	130
E.1	Acquisition software — usage	130
E.1.1	Microstage movement	130
E.1.2	General Description of STEDAcquirator	131
E.1.3	Modes of acquisition	134
E.2	Acquisition software — design	134
E.2.1	Some LabView constructs used	134
E.2.2	‘STEDAcquirator.vi’	135
E.2.3	‘MicrostageSteuerung.vi’	137
E.3	ImageJ plugins	137
E.4	Spectraviewer and other matlab scripts	137
E.5	OME-TIFF dll	137
F	Definitions	139
A	Bibliography	145
Index		155

Chapter 1

Introduction

Structure and function are very closely linked in most biomaterials. Therefore, researchers investigating biological function should take care to think about the structure as well. The method of choice here is light microscopy. It quickly yields easily interpretable structural information. The tool features compatibility to aqueous samples and does not rely on toxic contrast agents. Furthermore, it can provide image sequences in real time. There have been some drawbacks to conventional light microscopy, however. A poor contrast in bright field microscopy has led to the development of dark field, phase contrast and fluorescence microscopies. The latter yields the best contrast, only showing structures that have been targeted by the imaged molecules, so-called fluorophores, beforehand. This technique has been consequently developed further to resolve finer structures. Development reached the classical diffraction limit proposed by Abbe [1873], and subsequently, there was little progress concerning resolution for a long while. For many investigations, images above the diffraction limit were satisfactory, but there were quite a few unresolved questions that emphasized the need for better resolution in far field fluorescence microscopy. It was only around the year 2000 that this barrier was overcome [Rust et al., 2006; Betzig et al., 2006; Klar and Hell, 1999]. Several techniques exist and all of them use nonlinear quantum properties of dyes for their gain in resolution. Here we shall discuss only the technology implemented in the Bausch lab during the course of this dissertation, which is stimulated emission depletion (STED) microscopy.

Chapter 1 Introduction

To provide acquaintance with the subject, concepts of optical microscopy are discussed in chapter 2. It offers all the facts needed to understand the idea of STED microscopy, which is introduced in the very end.

The gained knowledge is put in practise in the following chapter 3. Its first part conveys design considerations that led to the setup as it has been built. The second part describes characterization and specification evaluations performed on the setup to assess its performance.

Adressed scientific questions are revealed in chapter 4.

The appendix provides protocols developed or followed for sample preparation. Alignment details and information on self-developed hard- and software are included as well.

Chapter 2

Optical microscopy of biomaterials - concepts

By definition, a microscope is supposed to image small objects. Naturally, one of the most important questions one may ask about a microscope is, down to which length scale are structures still discernible by the apparatus? In physical terms, the relevant specification is called the resolution of the device. Already in 1873 when Ernst Abbe first described microscopic imaging analytically, he particularly focused on that property. From that point until the mid-1990s, a lower limit of the resolution due to the wave nature of light was accepted.

In the following paragraphs, the ideas that lead to Abbe's notion of optical resolution being limited by diffraction are recalled. This discussion conceptually follows two sources [Gross, 2003; Hecht, 2002a]. According to convention in the field, when directions in space are mentioned, the Cartesian coordinate system is chosen such that z points along the direction of propagation of light.

After this brief stroll through conventional microscopic techniques (sections 2.1 and 2.3), a pragmatic view on quantum physical properties and processes in fluorescent molecules is provided (section 2.2). These molecules are important to most imaging techniques in the life sciences and essential to the details of STED microscopy explained thereafter (section 2.4).

2.1 Wide field microscope

A wide field microscope basically consists of three collective lenses. These are the objective, the tube lens, and the ocular. In a so-called infinity-corrected microscope, the specimen is located in the focal plane of the objective, and all successive lenses are situated such that their focal planes overlap. This situation is visualized in Fig. 2.1. If a camera is used for image construction instead of a human eye, the eye lens does not have to be compensated by the ocular and therefore the latter can be omitted. The camera is then positioned at the back focal plane of the tube lens.

In the introduction to this chapter, the reason for the conventional resolution limit has been stated already. It is caused by the wave nature of the probing beam. That can consist of light as in this case, electrons in electron microscopy, or indeed any relativistic particle in high energy physics. Insight into how diffraction affects a microscope is gained more easily by first investigating its effects with a single lens and only then adding the complexity of a system of multiple lenses.

The relevant observable is the intensity pattern generated by objects illuminated by a source of light. In diffraction theory, briefly, interference of waves stemming from all transparent positions in the object plane is calculated for every point at the plane of observation. Various solutions exist for special cases¹. In the Fraunhofer approximation, the diffraction pattern observed at an infinite distance is the Fourier transform of the object causing diffraction.

To elucidate whether and how Fraunhofer diffraction can be applied to a lens, it is enough to find two planes between which the light pattern is Fourier transformed. To that end, it helps to consider simple cases. The Fourier transform of a Dirac- δ function is a constant value and vice versa. Speaking in terms of optics, that translates to a single spot of light being the Fourier transform of a plane wave. Light from a point source positioned in the focal plane of a perfect lens becomes a collimated beam

¹The Fraunhofer approximation is also called the far field approximation of diffraction, in contrast to the Fresnel approximation, which discusses the electromagnetic field near the diffracting object.

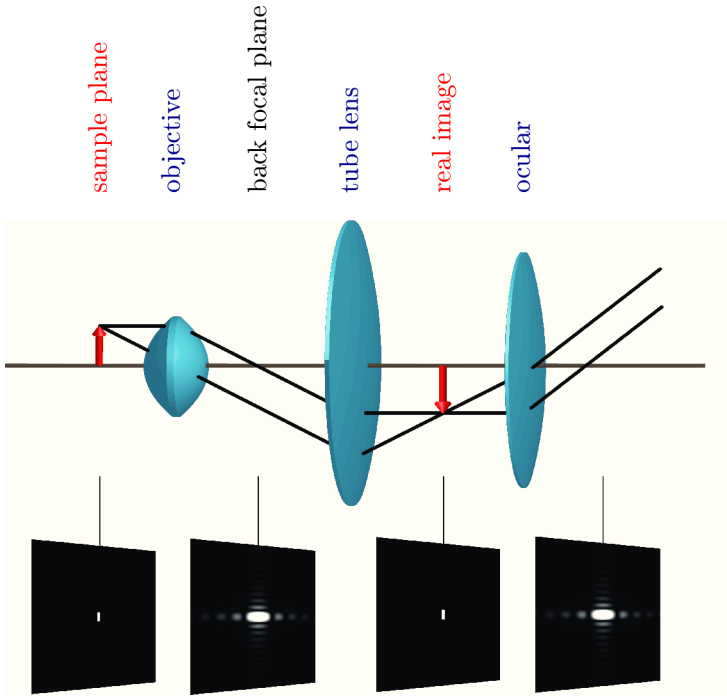


Fig. 2.1 **Schematic drawing of an infinity corrected wide field microscope:**

An objective, a tube lens and an ocular (blue discs, left to right) make up a wide field microscope. For better readability, all lenses are drawn in a biconvex shape. The objective Fourier-transforms the specimen (red arrow on the left) into its back focal plane, and the tube lens applies a reverse Fourier-transform into the corresponding plane and thereby forms a real image of the specimen (right red arrow). The ocular serves as a magnifying glass to make this image accessible to the human eye. The Fourier transforms are apodized by the lens apertures, which is the reason for the diffraction limit. For visualization, the images of a rectangularly shaped object in various focal planes is shown. (Apodization not shown)

behind the lens, while a plane wave passing a lens is focused to one single spot on the back focal plane. Thus, a lens can be thought to apply a Fourier transform from one to the other focal plane. To make the analogy to Fraunhofer diffraction, the front focal plane of a lens can be identified with the diffraction plane in diffraction theory, while the back focal plane corresponds to the screen at infinite distance. This holds true for lenses with a very large radius. A real lens with a finite radius cuts off some of the light that would contribute to the diffraction pattern. This cut-off can be modelled by an apodization, cutting off the high frequencies of the Fourier transform.

Accordingly, the pattern in the back focal plane of a real lens illuminated by a plane wave can be calculated via Fraunhofer diffraction on a circular aperture of corresponding size. The latter is a standard problem in diffraction theory discussed in various textbooks (see for example [Hecht, 2002b]) and results to

$$I(\vartheta) = I(0) \left(\frac{2 J_1(kr \sin \vartheta)}{kr \sin \vartheta} \right)^2 \quad (2.1)$$

With the Bessel function of first order J_1 , the aperture radius r , the wave number $k = 2\pi/\lambda$, and the angle of observation ϑ . In the focal plane, the spherical coordinates are conveniently replaced by their Cartesian counterparts. Due to symmetry, only one axis is of interest. Hence, $x = f \tan \vartheta$. For small angles ϑ , $\tan \vartheta \approx \sin \vartheta$ can be substituted:

$$I(x) = I(0) \left(\frac{2 J_1\left(\frac{2\pi r}{\lambda f} x\right)}{\frac{2\pi r}{\lambda f} x} \right)^2 \quad (2.2)$$

This description is visualized in Fig. 2.2 by the red rings and in Fig. 2.3 by the black line. It describes the intensity distribution in the back focal plane of a small lens with focal length f illuminated by a plane wave.

This plane wave might be produced by a point source in the focal plane of a non-apodizing lens (see Fig. 2.2, left). Mathematically, this process from point source to diffraction pattern involves a Fourier transform, an apodization, and an inverse Fourier transform. Interestingly, switching the

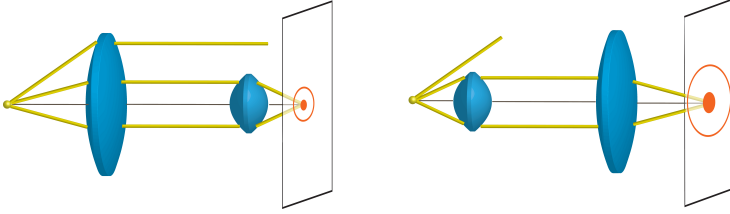


Fig. 2.2 Diffraction and lens: Left: A light source (yellow dot) illuminates a big lens, which generates plane waves. A small lens Fourier transforms this onto a screen introducing apodization. The image on the screen is an Airy pattern (red). Right: Lens succession is the other way around. Then, the pattern on the screen is the same, but differently scaled according to the focal lengths of the lenses.

lenses does not make a difference qualitatively: A point source is placed in the focal plane of a small lens and the image is acquired behind a large lens (see Fig. 2.2, right). Hence, in the latter case, the electromagnetic field between the two lenses cannot be described by a plane wave due to diffraction at the collimating lens. For the image, however, the process of Fourier transform, apodization, and reverse Fourier transform remains the same, and thus the result is unchanged.

In the microscope presented in Fig. 2.1, the described Fourier transform combined with apodization takes place twice or thrice in the apparatus, depending on whether imaging takes place with the eyes or a camera. The apodization of the Fourier transform reduces the spacial resolution because high Fourier frequencies are responsible for reconstructing small length scale structures. On the other hand, the apodization of the Fourier back transform, as performed by the tube lens, only reduces the field of view. So, the tube lens diameter and focal length are not of interest with regard to the resolution. The ocular does not play a limiting role either. Its source pattern is the real image in its front focal plane, and that is an image of the sample which is already magnified by a factor in the range of $M = 10 - 100$. Let d_{min} be the minimal distance resolvable by the objective. Then, the ocular only needs to resolve distances as big as $M \times d_{min}$. Thus only the

apodization by the objective lens needs to be considered for the resolution of a wide field microscope.

As discussed above, the optical path limits resolution *via* diffraction. Correspondingly, the image of a single point source is not a single spot, but it is smeared out in three dimensions. The light distribution in the image is called the point spread function (PSF) of the optical setup. The actual image can be calculated by a convolution of the specimen with the PSF. The transverse cut of the PSF through the center is called the Airy pattern. In the early days of the discovery of the resolution limit, its most prominent aspect was the bright circular spot which is the area inside the first minimum of the Airy pattern. This area is dubbed the Airy disc.

Taking these considerations together, the term in equation (2.2) describes the Airy pattern of a microscope when f is the focal length of the objective.

As a side remark, it may be noted that although the basic principles of this discussion have been developed for the theory of optics, they are not restricted to visible light. They pertain to any scattering process even at highest energies of subatomic particles. Even the naming has been adopted.

The discussion up to now has been limited to single point sources. For describing more complex objects, no further thoughts need to be invested, however. This is because according to the principle of Huygens, every optical object can be modelled by a superposition of single point sources.

2.1.1 Resolution criteria

Whether a beholder of an image can tell structures apart that lie close to each other depends on many and partly subjective factors. To render the decision process objective, clear criteria are needed that define the limiting distance at which two objects can be just resolved. Several criteria have been proposed. Four of these are presented here, the most prominent being the Rayleigh and the Sparrow criteria.

(i) The Rayleigh criterion states that the images of two points can be resolved if the main maxima of their diffraction patterns are farther apart

than the distance between the first minimum to the main maximum of one diffraction pattern [Rayleigh, 1902]. Accordingly, the minimal resolvable distance d_{min} equals the position of the Airy pattern (see equation 2.2 and Fig. 2.3) where J_1 first vanishes. As pointed out in mathematical tables [Bronstein et al., 2001], this first minimum of J_1 occurs where the argument amounts to 3.83. Typically, the half opening angle of the objective $\tan \alpha = r/f$ is used instead of the focal length and radius.

$$\frac{2\pi r}{\lambda f} d_{\min,R} = 3.83 \quad (2.3)$$

$$d_{\min,R} = 1.22 \frac{\lambda f}{2r} = 1.22 \frac{\lambda}{2n \tan \alpha} \quad (2.4)$$

$$\approx 0.61 \frac{\lambda}{NA} \quad (2.5)$$

Where the numerical aperture (NA) was introduced as $NA = n \sin \alpha$ with the refractive index of the immersion medium n . The approximation $\tan \alpha = \sin \alpha$ holds true for objectives with a low numerical aperture.

(ii) Carroll Sparrow defined that the images of two points can be resolved when there is a minimum in the resulting intensity curve [Sparrow, 1916]. When both points have the same intensity, the second derivative of the intensity curve is zero at half of the minimal resolvable distance. It is evaluated as

$$d_{\min,S} = 0.48 \frac{\lambda}{NA} \quad (2.6)$$

(iii) A third way to define the resolution is by assuming that the minimal resolvable distance equals the full width at half maximum (FWHM) of the point spread function. Especially in scanning microscopy, this can be measured very conveniently. The Airy pattern (equation 2.2) has its half maximal value at

$$\frac{\pi D}{\lambda f} \frac{\text{FWHM}}{2} = 1.616 \quad (2.7)$$

$$\text{FWHM} = 0.51 \frac{\lambda}{NA} \quad (2.8)$$

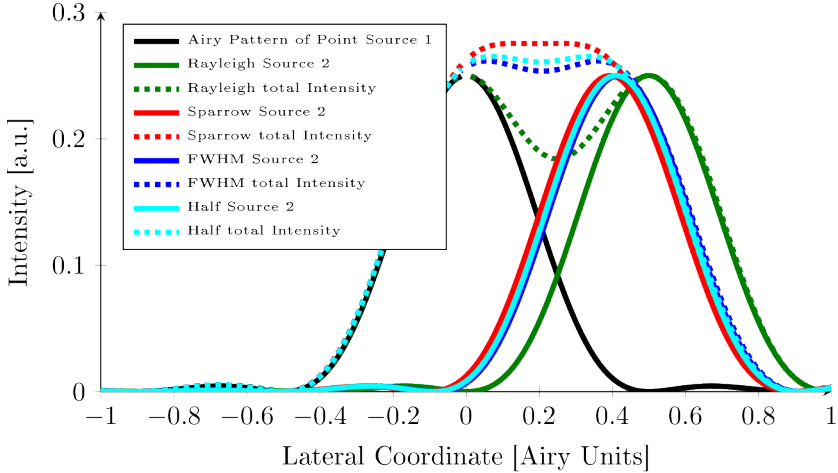


Fig. 2.3 Airy patterns at minimal distances of various resolution criteria: The black line represents the image of a point source. The solid lines in other colours show a second point source at minimal distances according to the discussed criteria. Resulting images of the two point sources are shown as dotted lines. The lateral coordinate is given in Airy units. One Airy unit corresponds to the diameter of the central area of non-zero intensity in an Airy pattern.

(iv) It might be worth mentioning that in literature sometimes resolution is defined without a special justification as

$$d_{\min} = \frac{\lambda}{2NA} \quad (2.9)$$

Fig. 2.3 illustrates the different resolution criteria. All of them assume that noise is negligible. It is worth keeping in mind that the noisier the data, the harder it gets to discern the PSF, hence the resolution worsens.

Furthermore, discretization occurring in digitized images is not taken into account by the criteria. According to the Nyquist-Shannon sampling

theorem [Nyquist, 2002], data needs to be oversampled by a factor of about 2.3 in order to safely identify features. Due to this fact, the imaging resolution of digitized images needs to be at least 2.3 times better than the structures to be resolved.

Note that the resulting image of two dots depends on whether their light emission is coherent or not. In case of coherence, the amplitudes of the two images are added up before calculating the intensity by applying a square. For incoherent illumination, only the intensities are added. The latter yields a better resolution and the resolution can be calculated using the equations given above. A maximally incoherent illumination can be achieved in bright field microscopy by using Köhler illumination [Köhler, 1893]. Note that in fluorescence microscopy, all emitters are incoherent with respect to each other, so no special care has to be taken regarding this issue.

2.1.2 Depth of field

The resolution discussed up to now was only referring to the lateral direction. Axially, microscopes have a much lower resolution, called depth of field. It is the maximal distance two objects can have axially and still be imaged in focus in the same image. The corresponding term in the image plane of the objective is called depth of focus.

There are various expressions using different approximations, all of them agreeing in the order of magnitude but differing in detail [Sheppard, 1988; Shillaber, 1944; Tkaczyk, 2010].

One well accepted approach uses diffraction theory of aberrations [Born and Wolf, 1993b] and results in

$$d_z = \frac{n \lambda}{NA^2} \tag{2.10}$$

2.1.3 Contrast

Apart from resolution, a further important aspect of imaging is contrast. If different regions in an image have too similar signal values, they cannot be

recognized even if the resolution is very high. There are many quantities describing contrast. One of them is the Weber contrast

$$K_W = \frac{S_{\max} - S_{\min}}{S_{\min}} \quad (2.11)$$

with the maximum and minimum signal values S . Its value varies between zero and infinity. It is commonly accepted that the threshold to discerning structures is a Weber contrast of 1 % to 2 %. This, however, applies when noise is negligible. Structures in noisy images can only be discerned with a higher Weber contrast.

2.2 Photophysics of fluorophores

There are various methods for generating contrast in microscopic imaging. One of the most powerful, most widely used and to the presented setup crucial methods is to make use of fluorescence. This paragraph is dedicated to the physics governing the involved processes.

Fluorescence is the emission of light accompanying a quantum mechanical transition of molecules. Molecules are assemblies of atoms bound together by their outermost electrons which share atomic orbitals, thereby forming covalent bonds. These assemblies can be regarded as entities, and molecular orbitals can be introduced in extension to atomic orbitals. These molecular orbitals are connected to well-defined electronic binding energies, and electrons can undergo transitions between orbitals just like in atoms, thereby lifting or lowering the energy of the molecule. A long-lived molecule has an even number of electrons, otherwise it would quickly find a reaction partner to form a different molecule. Thus all orbitals are occupied by two electrons of opposite spin when the molecule is in the ground state. Hence it is then in a singlet state. As binding energies are smaller than in atoms, the photon emitted during a transition from the lowest unoccupied molecular orbital (LUMO) to the highest occupied molecular orbital (HOMO) is not in the X-ray but in the ultra violet to infrared range [Turro,

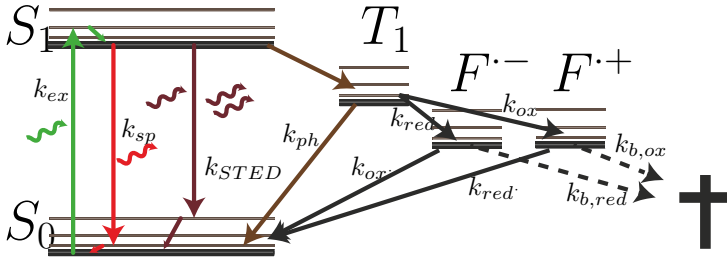


Fig. 2.4 Jablonski diagram: Vibronic states of a fluorophore with vertical position representing binding energy. The ground state (S_0) of a molecule has the highest binding energy, and is shown lowest in the diagram. The electron with highest energy is in the HOMO. Vibrational sub-levels increase the molecule's energy slightly and are shown as thin lines in all electronic states. When the electron is excited to the LUMO, the molecule has a higher energy and is in the first excited state (S_1). In addition to the singlet states, the electron in the LUMO can undergo a spin-flip, thereby bringing the molecule into the first triplet state T_1 . Higher states exist but are left out in the diagram. Within the ROXS scheme, ionic forms $F^{\cdot-}$ and $F^{\cdot+}$ of the molecule are exploited. If the anion is further reduced or the cation oxidized, the molecule becomes permanently deactivated (cross). Higher groups of states exist but are left out in this diagram. Transition processes are shown as arrows, and their probability can be quantified by means of the transition rates k_i . Transitions involving photons are shown with wavy arrows

1978]. In addition to electronic states, however, a molecule can have various vibrational states, describing the energy stored in modes of oscillatory movement of its constituting atoms. The combination of electronic and vibrational states are termed vibronic, and can be visualized in a so-called Jablonski diagram as depicted in Fig. 2.4.

The difference in energy between vibrational levels is smaller than between electronic levels. For this reason, the molecule is said to be in state S_0 when its highest electron is in the HOMO without regard to the specific mode the atoms are vibrating with (bottom left part of Fig. 2.4). Accord-

ingly, S_1 describes the state of the molecule when the electron is in the LUMO (top left part of Fig. 2.4).

When the molecule incorporates heavy atoms or appropriate reaction partners are in the vicinity, chance allows that the electron in the LUMO undergoes a spin-flip. Then, the molecule is not in a singlet, but in a triplet state. The according state is called T_1 (center top part of Fig. 2.4) and the molecule is said to have undergone inter-system crossing. Simple quantum mechanical descriptions neglect the spin-orbit interaction necessary for this spin-flip, which is why the process violates the QM rules of the simple system. This violation explains a low probability for the process.

Transitions between states occur when interactions with photons or other molecules take place. Molecules with many delocalized electrons typically have a high probability for photon-mediated transitions. These molecules are called fluorophores and can be used as dyes to label structures of interest. The transition from S_0 to S_1 , induced by the absorption of a photon, is termed excitation (see Fig. 2.4, green). A fluorophore in S_1 has a certain probability to emit a photon and go back to any vibrational level of S_0 . The process is called spontaneous fluorescent emission and typically occurs within a few nanoseconds (see Fig. 2.4, red). As in transitions, the additional or lacking energy of the system is carried by photons, it becomes clear that the emission wavelength is always longer than the excitation wavelength. The transition can be induced, too. A photon with an energy in the emission spectrum can interact with a fluorophore in S_1 , thereby causing it to jump to S_0 and simultaneously emit a second photon with the same characteristics as the first; the two exiting photons are entangled. This process is called stimulated emission (see Fig. 2.4, dark red). Transitions including a spin-flip are quantum mechanically forbidden and occur only when a factor comes into play that is neglected in the corresponding fundamental calculations. For this reason, spontaneous emission from T_1 is much less probable than from S_1 . Accordingly, the state has a higher lifetime, in the range of microseconds to hours. The process is then called phosphorescence (see Fig. 2.4, brown).

Typically, fluorophores are used in aqueous solution. Therefore, the

probability of mechanical interaction with the surrounding medium is high. That is why vibrational levels decay quickly and nonradiatively to the vibrational ground state in a process called internal conversion, dissipating the energy to the surrounding medium. The corresponding lifetime is in the order of a picosecond [Penzkofer et al., 1976].

For fluorescence imaging, transitions between S_0 and S_1 are used. Fluorophores in the sample are excited by light in the absorption spectrum and the subsequent spontaneous fluorescence is detected. This way, fluorophore density in the sample is mapped onto the image.

However, spontaneous fluorescence competes with intersystem crossing when the molecule is in its excited state. If the molecule moves into the triplet state, it is shut off for a while because phosphorescence has a high life time as mentioned before. Under certain conditions, this happens with a relatively high probability. The dye is then said to blink. This reduces signal and is therefore undesirable in conventional fluorescence imaging. Even worse, the triplet state is a starting point for the most common photobleaching pathway. Photobleaching describes a process that renders the dye incapable of fluorescence. If not prepared specially, an aqueous solution contains a high amount of dissolved oxygen molecules. These are present in a triplet state and therefore likely to react with the fluorophore in T_1 . This reaction leaves the dye ionized, and a following interaction with an excitation photon enables reactions that alter the structure of the molecule in such a way that the states S_0 and S_1 move to different levels.

To reduce the probability of photobleaching, oxygen scavenging systems can be introduced into the solution. A novel version of these is pyranose oxidase-catalase, a combination of enzymes that catalyse the binding of oxygen to glucose to form a ketone [Swoboda et al., 2012]. One drawback of this system is that, blinking times increase. For this reason, a general scheme of a reducing and oxidizing system (ROXS) has been put forward [Vogelsang et al., 2008]. Reducing and oxidizing agents are added to the solution in millimolar concentrations to depopulate the triplet state quickly. A reducing agent reduces the triplet molecule to a radical anion $F^{\cdot-}$ (see Fig. 2.4, right side) which in turn is oxidized by the oxidizing agent back

to S_0 . Alternatively, an oxidizing agent can oxidise T_1 to yield a radical cation F^+ , followed by reduction to the singlet ground state. A concentration in the millimolar range corresponds to about a molecule per cube of 10 nm edge length. Thus, oxidizing and reducing rates $k_{\text{red}}, k_{\text{ox}}, k'_{\text{red}}, k'_{\text{ox}}$ are very fast and fluorescence recovery is high. The signal of a dye in ROXS conditions typically increases by one to two orders of magnitude with respect to a normal buffer.

2.3 Confocal microscope

Confocal microscopy is a technique patented in the 1960s [Minsky, 1961] but it has started to be of use only in the 1980s to 1990s due to its demand for high detection efficiency and laser quality. Compared to wide field microscopy, its main benefit is the better axial sectioning. It permits to image thin optical slices and create 3D reconstructions of thick samples.

There are different implementations of the technique. Most widely used are the spinning disk and the confocal laser scanning microscope (CLSM).

For the latter variant, excitation light is sent to an excitation pinhole and collimated to a single mode parallel beam bundle. Then it is transmitted through a dichroic beam splitter and focused into the sample to the focal point of the objective. There, it causes dyes to fluoresce. The emitted light is collected by the objective, reflected by a dichroic beam splitter, and focused to a second pinhole. The photons passing through are detected on a point detector. The process is shown in Fig. 2.5. Out of focus contributions do not pass the pinhole. The detected intensity corresponds to the fluorophore density in the probed spot. The sample is scanned by moving the probing volume to positions on a predefined grid. This is achieved either by moving the sample (stage-scanning), or by deflecting the beam (beam-scanning). The recorded intensities are displayed by assigning different brightness values to squares corresponding to the position in the grid, yielding an image of the fluorophore density in the sample. Each spot in such an image is called pixel for two dimensional images and voxel for three dimensional images.

A spinning disk microscope is a parallelized variation of this scheme.

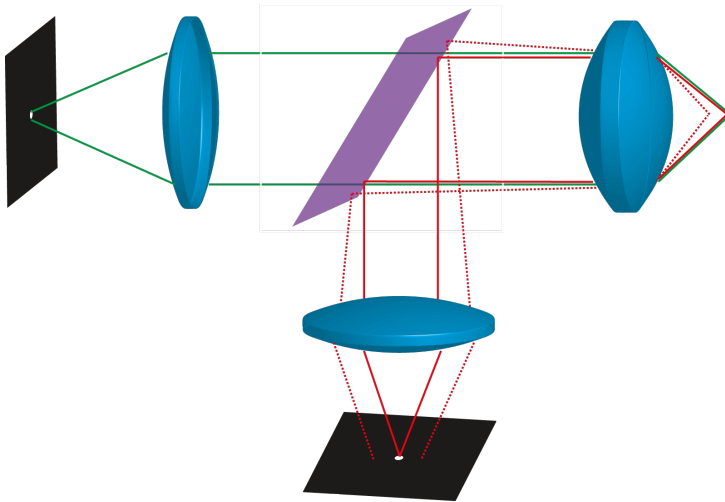


Fig. 2.5 Schematic drawing of a confocal microscope: Light is collimated from a point source (left pinhole) and focused on a spot in the specimen (right). The emitted light (shown in red) is collected by the objective and reflected by a dichroic mirror (purple). Light from the focal spot is focused on a second pinhole (bottom), and detected thereafter. Light emitted from a different spot does not pass the detection pinhole (broken line) and is therefore not registered.

Here, light passing a rotating disk of pinholes is imaged on a camera and each spot on the camera is acquired as one pixel in the eventual image. The next frame of the camera fills neighbouring pixels for the image. This approach yields a little lower resolution than CLSM but allows for faster imaging.

2.3.1 Resolution

The various resolution criteria (*i*) to (*iv*) in section 2.1.1 emphasize different aspects of the PSF. Accordingly, confocal microscopy shows different degrees of resolution improvement, depending on the criterion applied. In

general, the PSF of the system is the product of the excitation and detection path PSFs.

(i) The Rayleigh resolution depends on the zero point and therefore does not increase simply because of the multiplication of excitation and detection PSFs. It can be increased insignificantly with respect to wide field microscopy by reducing pinhole sizes, however. But this increase comes with great cost in the number of detected photons.

(ii) If both excitation and detection beam pass through the same objective, and its aperture is filled, the PSF in the focal plane is the square of the Airy pattern in wide field microscopy. For that reason, the Sparrow resolution decreases to

$$d_{\min,S} = 0.32 \frac{\lambda}{NA},$$

with conceptually the same calculations as in the bright field case.

(iii) Due to the multiplication of the two PSFs, the FWHM decreases to

$$\text{FWHM} = 0.37 \frac{\lambda}{NA},$$

which reduces the minimum resolvable distance by a factor of $1/\sqrt{2}$ with respect to the bright field case.

Note that these calculations have been based on Fraunhofer diffraction theory. However, when dealing with high NA objectives, Fraunhofer diffraction theory does not hold true any more. The z components of the electric field in the sample plane have to be taken into account. These result from the high angles of incidence the objective manages to collect. Debye diffraction theory considers this fact. The resulting PSF can be calculated numerically quite easily. A method has been described in Leutenegger [2006]². For qualitative comparisons, however, the analytical results obtained along the lines of Fraunhofer's thoughts are more instructive.

²An implementation of the algorithm presented in this paper has been written in MATLAB[®] during the course of this work. It can take into account many freely selectable parameters and initial conditions, amongst these the phase of the incoming wave front, thus being able to calculate depletion patterns for STED microscopy as described in section 2.4. The script is accessible in the central MATLAB[®]SVN repository at `\Heinrich\trunk\matlab_calcs\Focus_Field_calculation\calcFocusField.m`

2.3.2 Depth of field

Terms for the depth of field for confocal microscopy are derived the same way as for wide field microscopy. Here, the overall axial resolution is calculated as a harmonic mean value of a diffraction optical and a geometric optical term.

$$d_{z,\text{conf}} = \sqrt{\left(\frac{n \lambda}{NA^2}\right)^2 + \left(\frac{\sqrt{2} n PH}{NA}\right)^2} \quad (2.12)$$

with, PH denoting the pinhole diameter. A suitable mathematical description covering the form of a confocal PSF in more detail is presented in [Dertinger et al., 2007].

Interestingly, the axial resolution of a confocal microscope does not differ in essentials from that of a wide field microscope. Still, the main advantage of this technique lies in 3D imaging. This apparent contradiction can be explained by an additional concept coming into play. In wide field microscopy, light emitted from an out of focus plane still reaches the image. Hence, no optical sectioning takes place. A confocal microscope, on the other hand, cuts off out of focus contributions using the detection pinhole as depicted in Fig. 2.5. Keeping in mind that confocal 3D images show much more details, it becomes clear that for 3D imaging, axial sectioning is even more important than the depth of field. Related to that, axial sectioning explains the better contrast of confocal images with respect to wide field images.

2.4 STED microscope

STED microscopy is one of several superresolution far-field fluorescence microscopy techniques. Basically, fluorescence is confined to a controlled region of sub-diffraction size and this region is scanned through the sample much like in confocal microscopy.

Due to diffraction, it is not possible to confine the excitation light more than into the confocal volume. However, it is possible to excite a confocal

spot and then quench excited molecules in the outer regions of that spot. This is what is achieved in STED microscopy. In order to implement that, an additional beam comes into play as compared to a confocal setup, dubbed the STED beam. Its beam profile does not have the usual Gaussian shape but is formed in a way that it features a point of zero intensity in the focus of the objective. The most efficient and widely used beam profile is the so-called donut depletion pattern, which shows a toroidal intensity distribution around the focus (see section 2.4.1 for details). The beam temporarily switches off fluorophores. This is achieved by using stimulated emission as a quenching process, which has been introduced in section 2.2. Dyes that are supposed to be shut off are irradiated by light to induce stimulated emission. Then, the processes of spontaneous and stimulated emission compete. Their relative efficiencies can be quantified using the corresponding rates. The probability to de-excite a fluorophore *via* stimulated emission as opposed to spontaneous emission is

$$p_{\text{STED}} = \frac{k_{\text{STED}}}{(k_{\text{STED}} + k_{\text{spont}})}, \quad (2.13)$$

so a very high STED rate ensures that spontaneous emission becomes negligible. The wavelength of this light is chosen away from the maximum of the emission spectrum, and filters are used to block it from detection. This way, only spontaneously emitted light is detected. Significant spontaneous emission can only originate from the central region where the STED intensity vanishes. The idea is visualized in Fig. 2.6.

The rate of stimulated emission depends linearly on the intensity of STED light *via*

$$k_{\text{STED}} = \sigma_{\text{STED}} \cdot I_{\text{STED}} \cdot \frac{\lambda_{\text{STED}}}{hc} \quad (2.14)$$

where the cross-section for stimulated emission σ_{STED} , intensity I_{STED} , and wavelength λ_{STED} of the STED beam have been used. For a measure of probability to quench the dye, the saturation factor $\zeta = I_{\text{STED}}/I_s$ can be defined. Herein, the saturation intensity I_s is defined as the STED intensity which reduces the probability of spontaneous emission to half its initial value.

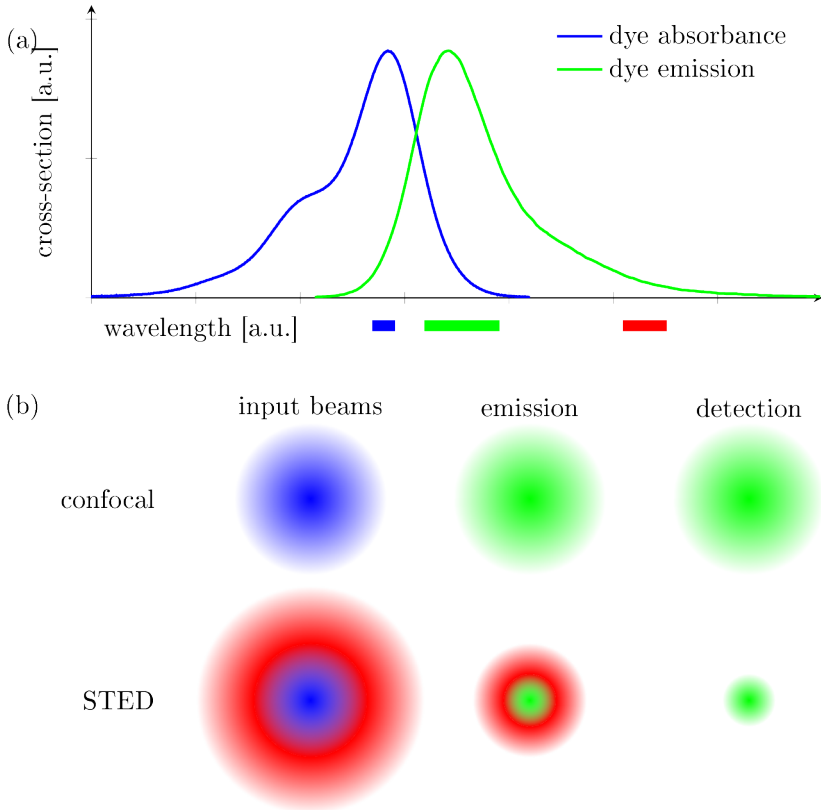


Fig. 2.6 Working principle of STED microscopy: (a) Typical excitation and emission spectra of a fluorophore are shown. Wavelengths used for excitation, detection, and stimulated emission are highlighted as blue, green, and red bars, respectively. (b) Comparison of the formation of the effective PSF for confocal and STED microscopies. In confocal microscopy, the excitation beam excites a confocal volume of dyes and their spontaneous fluorescence is detected. In STED microscopy, the sample is illuminated with an excitation and a depletion beam. The toroidally shaped depletion beam stimulates emission in the wavelength applied in the outer part of the spot. The central part is left to emit spontaneously, while stimulated emission occurs in the region where both excitation and STED light coincide. Filters block the stimulatedly emitted light and only the spontaneously emitted light reaches the detector. The wavelengths of the spots are set in the ranges in which the bars in corresponding colours are drawn in (a).

Cross sections for stimulated emission are in the range of $\sigma_{\text{STED}} = 10^{-17} \text{ cm}^2$ to 10^{-16} cm^2 and the decay time constant for fluorescence usually amounts to a few nanoseconds [Leutenegger et al., 2010]. Thus, STED intensities of $\langle I_{\text{STED}} \rangle \gg I_s \approx 5 \text{ MW/cm}^2$ render spontaneous emission very improbable.

Taking this together, spontaneous emission can be neglected in regions of the donut where $I_{\text{STED}} \gg I_s$. In the center, where $I_{\text{STED}} = 0$, the fluorescence probability is unperturbed. As the PSF describes the probability of where a detected photon stems from, the result is a narrowed PSF, thus an increased resolution.

2.4.1 Depletion pattern and polarization

The depletion pattern is most often generated with a vortex phase mask. This is a ramp of plastic mould that increases in thickness with the azimuthal angle around an axis perpendicular to the surface, and which is brought into the center of a Gaussian beam. Due to the difference in refractive index between the mould and air, the phase of the rays of light is shifted depending on the optical path length through the mask. The pitch of the pattern is chosen such that the relative phase covers a range of 2π along the azimuth. Figure 2.7a visualizes the pattern.

There are two ways to calculate the intensity pattern of such a phase modulated Gaussian beam. On the one hand, the incoming field in the plane of the objective lens $E_i(\varrho, \Phi)$ can be viewed as starting point for spherical waves according to Huygens' principle. Thus, the field in the focus $E_f(r, \varphi)$ on every point of interest is the interference pattern of all those waves (for coordinate systems, see Fig. 2.7b). While the calculation is easy for the focal point, it becomes tiresome at off-axis points of interest. However, this line of thought is resumed later in this section.

A second method is based on the results from section 2.1 and regards the objective lens as a Fourier transformer. Then,

$$E_f(r, \varphi) = \mathcal{F}(E_i(\varrho, \Phi)) \quad (2.15)$$

$$= \mathcal{F}\left(\exp\left(i\Phi - \frac{\varrho^2}{2\sigma^2}\right)\right). \quad (2.16)$$

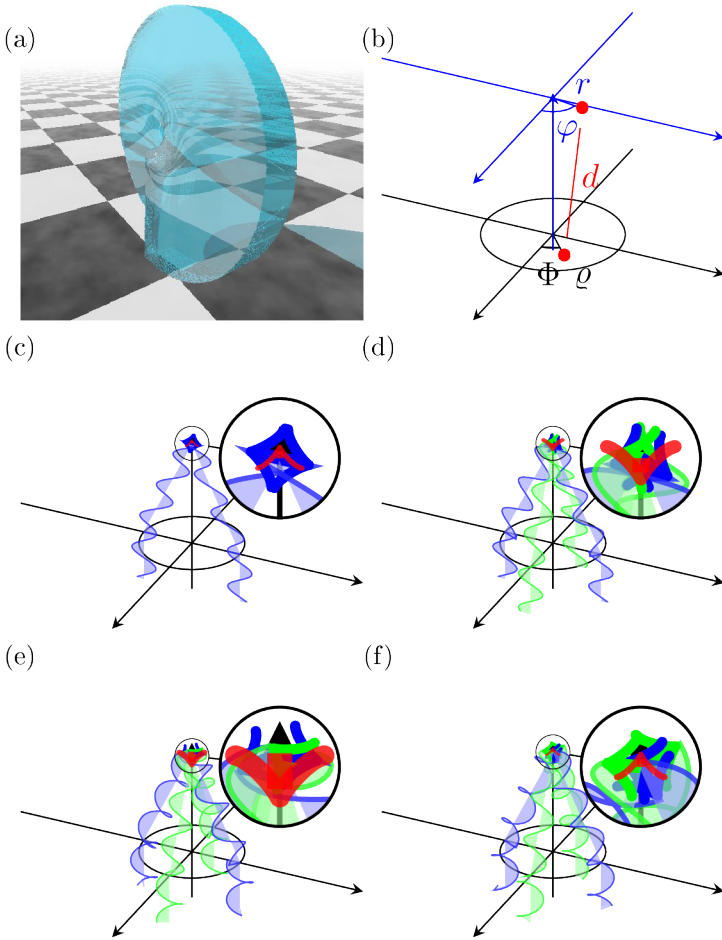


Fig. 2.7 Depletion pattern generation: (a) vortex phase plate used to phase-shape the input beam. (b) coordinate definitions. blue: focal plane. black: objective plane. (c)-(f) rays of light from a phase shaped beam, focused by the objective. Blue and green arrows depict the field vectors at the focus. The red arrow represents the sum of the four field vectors. (c) linear polarization, low NA. Donut center vanishes. (d) linear polarization, high NA. (e) left-handed circular polarization, high NA. (f) right-handed circular polarization, high NA. Donut center vanishes. See text for details.

The incoming field is not rotational symmetric. Thus, even a Fourier transform in polar coordinates needs to be expanded to higher Bessel functions. Numerical evaluation of the Fourier transform yields a toroidally shaped PSF.

The most crucial aspect of the depletion pattern is the lack of intensity in the focal spot. It turns out that the polarization state of the input beam is of highest importance. In order to understand under which circumstances the donut minimum is achieved best, the interference-based approach is of good use. For a gain in physical insight, the calculation is not done explicitly, but symmetry considerations and visualizations are applied.

The field in the focus $E_f(0, 0)$ is supposed to vanish.

$$E_f(0, 0) = \int d\Phi \int r dr e^{-2\pi i r \varrho \cos(\varphi - \Phi)} E_i(\varrho, \Phi) \stackrel{!}{=} 0 \quad (2.17)$$

If that is the case, it is very probable that already the integration over the azimuth yields zero, independent of the radius ϱ . Due to symmetry, it can be assumed that already two opposing rays, from the points $[(\varrho, \Phi), (\varrho, \Phi + \pi/2)]$ have a particular resulting field vector. The next paragraphs show that situations can be brought about where it vanishes. For more complex cases, the field vectors of the four points $[(\varrho_1, \Phi_1 + 1/2), (\varrho_1, \Phi_1 + 3\pi/2)]$ cancel out.

When an objective with a low numerical aperture is used, the change in orientation of the electrical field vectors does not need to be taken into account. Hence the field vector can be assumed to remain perpendicular to the optical axis even when the rays are focused. Consequently, they are not perpendicular to the direction of propagation. The situation is shown in Fig. 2.7c with a linearly polarized input beam. Note the distorted appearance of the waves in the focused part and that the field vectors in the focus (blue arrows) are perpendicular to the z -axis. Due to the phase plate, opposite rays are phase shifted by π as can easily be seen in the objective plane (round disc). The two field vectors shown have the same amplitude because $\|E_i(\varrho, \Phi)\| = \|E_i(\varrho, \Phi + \pi)\|$ for the phase-modulated Gaussian input beam. Because the field vectors point in opposite direc-

tions, they cancel out. Integration over all such pairs of rays of light yields zero intensity in the donut center.

However, for best resolution combined with a low STED intensity, a high NA is desirable. With a high numerical aperture, z -components of the rays refracted by the objective become non-negligible. Accordingly, the field vectors cannot be assumed to be perpendicular to the optical axis any more after refraction by the objective. Instead, they stay perpendicular to the propagation of light. Thus, for visualization, the rays have to be tilted as shown in Fig. 2.7d. Here two pairs of opposing rays with linearly polarized input light are shown. One pair is polarized parallel to its plane of refraction (blue) while the other is polarized perpendicularly to it (green). In the latter case, the tilt does not affect the orientation of the field vectors. Hence, the green rays still cancel out. However, the blue field vectors are tilted towards the optical axis. Thus, they cancel out in x and y , but a resulting z component remains. This contribution is positive for all positions in the (ϱ, Φ) plane at the point in time visualized. Hence, the resulting field $\mathbf{E}_f(0,0)$ does not vanish. A donut with finite intensity in the center is the result. Accordingly, stimulated emission takes place in the region to be detected, and the contrast decreases.

Circular polarization can solve this issue. Circularly polarized light results when the relative phase between the x and y components is $\pm\pi/2$. Consequently, the visualization looks like a left handed (see Fig. 2.7e, best conceivable below the objective plane) or like a right handed spiral (see Fig. 2.7f, below the objective plane). Depending on whether the rotational direction of circular polarization matches the phase plate orientation or not, the resulting field vectors of the pairs of rays have the same or opposing z -components. If the z -components are the same (Fig. 2.7e), the donut has a non-vanishing center. Its intensity even amounts to 20 % of the donut crest with a numerical aperture of 1.4. On the other hand if the z -components oppose each other, the four field vectors point towards the corners of an equilateral tetrahedron, causing the sum to vanish (Fig. 2.7f).

Hence, it is of crucial importance to impose the right orientation of circular polarization on the beam.

2.4.2 Resolution

The last paragraphs showed qualitatively that STED microscopy features a resolution superior to that of confocal microscopy. This section's aim is to quantify this property.

In order to calculate the resolution in STED microscopy, a quadratic dependence of STED intensity with the distance from the focus can be assumed in first approximation. This holds true only for the donut center, where the details of the resolution are determined. For convenience, it can be formulated as

$$I_{\text{STED}}(x) = 4 I_{\text{STED}} a^2 x^2 \quad (2.18)$$

with a the pattern steepness set by details of donut formation and I_{STED} the maximum STED intensity.

At this point, different degrees of approximation can be applied. More extensive calculations can be found elsewhere [Harke et al., 2008; Leutenegger et al., 2010]. Here, a short route is developed to focus on the essentials.

In general, the probability for spontaneous fluorescence p_{fl} can be derived from the probability to find a fluorophore in the excited state p_{ex} via the quantum yield for spontaneous fluorescence η_{fl}

$$p_{\text{fl}} = p_{\text{ex}} \cdot \eta_{\text{fl}} \approx p_{\text{ex}} \frac{k_{\text{fl}}}{k_{\text{fl}} + k_{\text{STED}}}, \quad (2.19)$$

with the rates for spontaneous and stimulated emission k_{fl} and k_{STED} , respectively. The approximation holds true when the rates for other decay paths of the excited state are negligibly low.

Per definition of the saturation intensity, the rate of spontaneous fluorescence can be related to that of stimulated emission as follows.

$$\frac{k_{\text{fl}}}{k_{\text{fl}} + k_{\text{STED}} \Big|_{I_{\text{STED}}=I_s}} = \frac{1}{2} \quad (2.20)$$

$$k_{\text{fl}} = k_{\text{STED}} \Big|_{I_{\text{STED}}=I_s} = \sigma_{\text{STED}} \frac{\lambda_{\text{STED}}}{hc} I_s \quad (2.21)$$

The position dependent quantum yield thus becomes with equations 2.14 and 2.18 and the definition of the saturation factor introduced before, $\zeta =$

$I_{\text{STED}}/I_{\text{s}}$

$$\frac{k_{\text{fl}}}{k_{\text{fl}} + k_{\text{STED}}(x)} = \frac{I_{\text{s}}}{I_{\text{s}} + I_{\text{STED}}(x)} = \frac{1}{1 + 4 \zeta a^2 x^2}. \quad (2.22)$$

This result can be used to calculate the position dependent fluorescence probability in STED microscopy from equation 2.19.

$$p_{\text{fl}}(x) = p_{\text{ex}}(x) \cdot \frac{1}{1 + 4 \zeta a^2 x^2} \quad (2.23)$$

For STED imaging, just as for confocal imaging, the PSF is the product of detection and fluorescence probabilities.

$$\text{PSF}_{\text{STED}}(x) = \text{PSF}_{\text{fl}}(x) = p_{\text{fl}}(x) \cdot p_{\text{det}}(x). \quad (2.24)$$

Excitation and detection probabilities can be linked to the confocal PSF as mentioned in section 2.3

$$p_{\text{ex}}(x) = p_{\text{det}}(x) = \sqrt{\text{PSF}_{\text{c}}} = \exp\left(-\frac{x^2}{4\sigma_{\text{c}}^2}\right). \quad (2.25)$$

Here, the PSF is normalized to a value of one in the center for convenience.

Combining equations 2.23 through 2.25, one gets

$$\text{PSF}_{\text{STED}}(x) = \frac{\exp\left(-\frac{x^2}{2\sigma_{\text{c}}^2}\right)}{1 + 4 \zeta a^2 x^2}. \quad (2.26)$$

The FWHM of this PSF serves as a measure of resolution.

$$\text{PSF}_{\text{STED}}(x_{1/2}) \stackrel{!}{=} 1/2 \quad (2.27)$$

$$2 \exp\left(-\frac{x_{1/2}^2}{2\sigma_{\text{c}}^2}\right) = 1 + 4 \zeta a^2 x_{1/2} \quad (2.28)$$

$$2 \left(1 - \frac{x_{1/2}^2}{2\sigma_{\text{c}}^2} + \dots\right) = 1 + \zeta a^2 x_{1/2} \quad (2.29)$$

$$x_{1/2} = \frac{1}{2\sqrt{\frac{1}{4\sigma_{\text{c}}^2} + \zeta a^2}} \quad (2.30)$$

Where the Taylor expansion of the Gaussian function has been employed until the second term. To bring this result into a more standardized form, $x_{1/2}$ and σ_c are replaced by their respective FWHM.

$$\text{FWHM}_{\text{STED}} = \frac{\text{FWHM}_c}{\sqrt{2 \ln 2 + \text{FWHM}_c^2 \zeta a^2}} \quad (2.31)$$

This result approximates the accepted law obtained after rigorous calculation [Harke et al., 2008]

$$\text{FWHM}_{\text{STED}} = \frac{\text{FWHM}_c}{\sqrt{1 + \text{FWHM}_c^2 \zeta a^2}} \quad (2.32)$$

reasonably well. An error of % at zero STED intensity is introduced due to the Taylor expansion of the exponential function. This mismatch decreases for higher values of ζ .

2.4.3 Impact of STED microscopy on the life sciences

Fluorescence sub-diffraction resolution imaging techniques are still young techniques and not ubiquitous yet. Still, a few discoveries with a high impact have been made with STED microscopy already. Here, some of them are mentioned very briefly. More examples can be found elsewhere [Müller et al., 2012].

(i) Neuronal vesicles carrying neurotransmitters between synapses have been imaged and their movement characterized for the first time. To that end, STED microscopy has been employed with a resolution of 60 nm and a frame rate of 28 Hz [Westphal et al., 2008].

(ii) Cristae in microtubules have been investigated only in electron microscopy up to now. Recently, they were investigated in intact cells using STED microscopy [Schmidt et al., 2009]. A heterogeneous distribution of cristae was observed: Regions of stacked cristae lamellae alternate with relatively large regions of up to $10 \times 10^5 \text{ nm}^2$ that were devoid of cristae.

(iii) The bacterial microtubule homologue FtsZ in *Bacillus subtilis* is thought to be a precursor of the eucaryotic Z-ring for cell division. It was imaged with STED microscopy and unexpectedly, a highly irregular helical structure was uncovered. Furthermore, a so-far unknown intermediate structure was found [Jennings et al., 2011].

(iv) In plants, PIN proteins are responsible for maintaining cell polarity. The mechanisms of this process are not well understood and a recent study investigated them using STED microscopy in live *Arabidopsis thaliana* cells. The results suggest that the regulation of lateral diffusion and spatially defined endocytosis, but not super-polar exocytosis have primary importance for PIN polarity maintenance [Kleine-Vehn et al., 2011].

2.4.4 Recent developments in STED technology

The field of STED microscopy has seen many advances addressing different issues in the past few years, mostly by one laboratory. Some of the more interesting are portrayed briefly in this paragraph.

(i) One persistent challenge of STED microscopy is the high intensity needed for stimulated emission. It is high because it is applied at the very long-wavelength tail of the emission spectrum, where the cross-sections for stimulated emission is low. The tail is chosen to prevent excitation by the STED beam that would then be detected and even decrease resolution. Here, the authors put up with the excitation and calculated the STED image from two images: one acquired with the STED beam on only and one with both excitation and STED on. This way, they can use lower STED powers. [Vicidomini et al., 2012]

(ii) Multichannel STED imaging is quite hard to perform because the three wavelengths - excitation, detection, and STED - for each fluorophore need to be accommodated in the visible spectrum. Additionally, care must be taken not to harm one kind of dye with the STED beam of the other. Bückers et al. [2011] overcame this challenge by discriminating the dyes not only by their spectrum but also by their fluorescence lifetimes. Thus, they can use the same set of wavelengths for two different dyes with differing lifetimes of 1.8 ns and 3.1 ns.

(iii) Aligning two donuts for two STED channels with high precision can be challenging. Göttfert et al. [2013] used one STED wavelength on two dyes, so the two channels had the very same donut and thus the channels were intrinsically coaligned.

(iv) To overcome the need of complex laser systems or the cumbersome synchronization of two lasers, Bianchini et al. [2012] used one laser for both excitation and STED. Using a femtosecond laser that allows for two photon excitation, they could stretch part of the pulses to efficiently stimulate emission without exciting.

(v) The combination of advanced fluorescence microscopy techniques has some attractiveness and so, Leutenegger et al. [2012] implemented a combination of TIRF, STED, and FCS.

(vi) Another combination of advanced fluorescence microscopy techniques combines STED with optical tweezers [Heller et al., 2013].

(vii) Speed being among the main advantages of STED microscopy over other subdiffraction techniques, the idea to parallelize the process in a spinning-disk like manner is self-evident. As STED microscopy needs high intensities, there are limitations to the degree of parallelization. For that reason, Chmyrov et al. [2013] used reversibly switching fluorescent proteins to accomplish the task.

Apart from establishing STED microscopy in a laboratory new to the technique, the setup described here brings two new technological aspects to the community.

1. It is the first three channel setup without the need for computational channel separation, even if one of the channels has confocal resolution.
2. STED and FRET have been combined here for the first time.

Chapter 3

Optical microscopy of biomaterials - technical aspects

With the insights obtained from the last section, technical details of a custom-built STED microscope can be discussed. The microscope has been built as part of this thesis. It is capable of imaging three channels quasi-simultaneously, two of these in sub-diffraction resolution. Furthermore, a gating electronics device was constructed which eliminates cross-detection and features a separate cross-detection output that can be used to acquire confocal reflectance as well as FRET data (see section 4.3).

3.1 STED setup design

A complex optical setup needs to be planned carefully. Many aspects have to be taken into account, of which only the most important can be described here. To structure these aspects, they are subdivided into spectral, temporal, and spatial categories in the following paragraphs.

3.1.1 Spectral design

The described microscope is built to facilitate three-channel fluorescence measurements in which one features a confocal resolution of approximately 250 nm and two feature STED resolutions of down to 50 nm. In the design phase, several demands had to be kept in mind. Firstly, the wavelengths for excitation, detection, and STED should be separated spectrally far enough

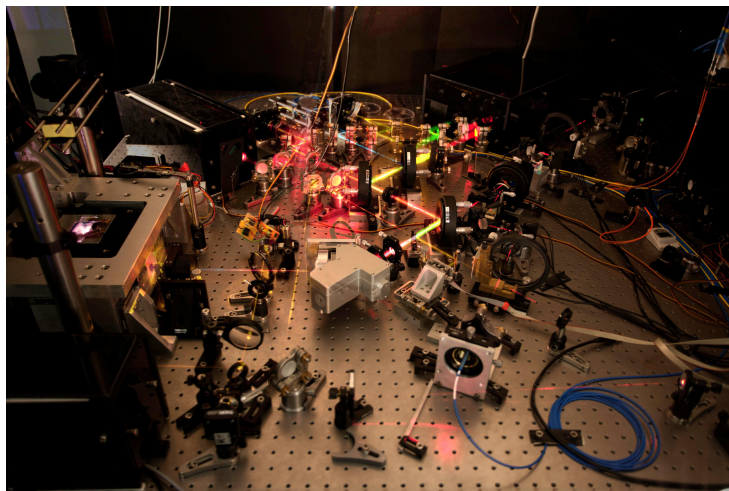


Fig. 3.1 STED Setup: The photograph shows the microscope part of the STED setup.

in order to minimize crosstalk while allowing for the windows to be broad enough to get good excitation and, more importantly, detection efficiencies. Secondly, dyes employed for one channel should not get bleached by incident light for a different fluorophore. Thirdly, the dyes should have properties suitable for high-quality imaging. And lastly, the availability of dichroics was an additional challenge.

To keep photobleaching to a minimum, certain issues have been accounted for. In STED microscopy, excited dyes are exposed to a high intensity of STED light. This bears the risk of inducing excitation to higher states which can lead to side reactions resulting in a deactivated or even permanently dysfunctional dye. To reduce the probability for this disadvantageous path, the photon energy should be kept low. For that reason, dyes in the red wavelength regime tend to be a better choice for STED microscopy. A further consequence of the high STED intensities is that regions of high cross-section in the excitation spectra of all dyes in

the sample should be far away from all STED wavelengths. Differently phrased, the STED wavelengths should not overlap significantly with any of the excitation spectra.

For the confocal channel, a low wavelength is preferable because the confocal resolution scales linearly with the wavelength.

Good properties for STED dyes alongside a high quantum yield and photostability are long fluorescence lifetimes, which correspond to low rates of spontaneous fluorescence. The issue is discussed more thoroughly in section 2.4. Amongst other companies, Atto Tec GmbH manufactures suitable dyes. It has been selected to be the prime supplier for labelling samples to be used in the setup.

The beforehand mentioned considerations resulted in the following spectral layout. The setup has been tailored to the dyes Atto 488 (confocal), Atto 590 (STED), and Atto 647N (STED). The corresponding channels are henceforth called *Blue*, *Orange*, and *Red* channels, respectively. Beam paths are named by a preceding '*Ex*', '*Det*', or '*STED*'. To give an example, *DetOrange* denotes the detection path for Atto 590. The respective spectra are shown in Fig. (3.2).

The two STED dyes are spectrally close together and in the red regime. Consequently, the two STED wavelengths are the highest wavelengths present in the setup, thus not lying in the absorbance spectrum of any dye employed. The confocal dye in contrast is quite far in the blue region of the visible spectrum in order to minimize crosstalk and to increase its channel's resolution.

The laser has been chosen on the basis of published work [Wildanger et al., 2008] but has been updated to a more powerful and reliable laser source (see Fig. 3.3) (ALP, Fianium Ltd.). It is based on a pulsed infrared fiber laser master oscillator which feeds three amplifiers and photonic crystal fibers. Nonlinear processes take place in the photonic crystal fibers which convert the infrared input light to a super-continuum or more tailored output spectrum. The advantage of this approach over others is the need for only one laser source and the intrinsic synchronization of all beam pulses. Due to the laser's architecture, the beam paths do not only have to

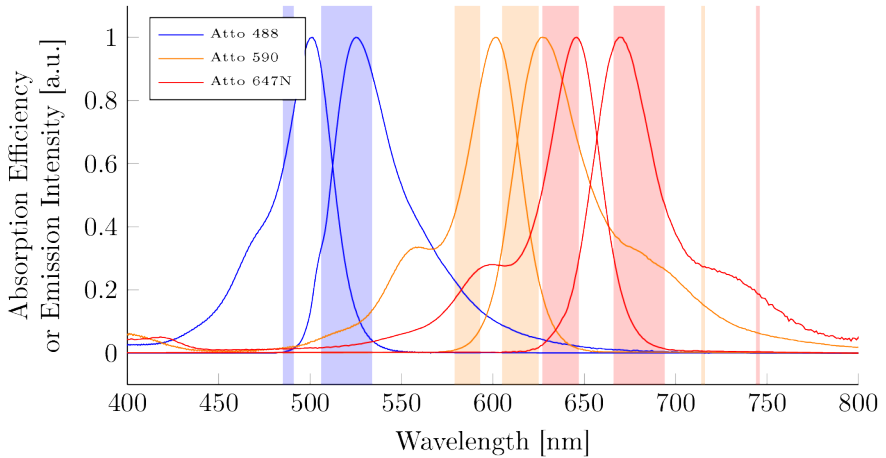


Fig. 3.2 Absorption and Emission Spectra of the design dyes: The colors blue, orange and red represent the spectra for Atto 488, Atto 590, and Atto 647N, respectively. Colored boxes represent wavelength windows for excitation, detection, and STED from left to right for all channels, respectively.

be combined, but they also need to be separated from the super-continuum beam. Therefore, the setup was split into two parts. The ‘pre-fiber’ part serves to provide the correct wavelengths for the five input beams: three excitation and two STED beams. The selected wavelengths are fed into single mode optical fibers. The other end of these fibers is situated in the ‘post-fiber’ part, which represents the real microscope. Fig. 3.4 shows the succession of dichroics used in the two parts of the setup. All dichroics and filters have been purchased from AHF Analysetechnik.

As the wavelengths used for excitation, detection, and stimulated emission of the two STED channels lie very close together, the system of dichroic mirrors had to be chosen with prudence. Special care has been taken to open the windows for detection as wide as possible, even if that meant decreasing excitation beam path efficiencies. The latter are of less importance because they can be compensated for by increasing the laser power.



Fig. 3.3 ALP laser source: The system consists of three parts: A rack chassis (left) contains an infrared fibre master oscillator and super-continuum amplifier. A photonic crystal fibre guides light to a free-space collimator (center) for super-continuum output. More electronic and optical cables connect the chassis with the remote head (right). Here, amplification and spectral tailoring takes place for the two STED outputs. Image courtesy of Fianium Ltd.

Fig. 3.5 shows the transmission efficiencies through all excitation and emission beam paths, excluding filters.

The angle of incidence to the dichroics has been chosen to be 45° for a convenient design of the optical path for most dichroics. In two cases - for the combination of the two STED beams and of the *Red* excitation and detection beams - the angle has been decreased to 10° . This decreases the wavelength interval between a good reflection and a good transmission¹.

¹The filters and dichroics work on the basis of interference. Light is refracted and transmitted through multiple layers of thin films with different refractive index. The transmitted beam consists of the interference of all waves reflected an even number of times while the reflected beam is made up of those that were reflected an odd number of times. The thickness and refractive index of each of those films is chosen to tune the transmitted and reflected wavelengths to the desired values. The characteristics can be calculated according to multiple beam interference [Lissberger and Wilcock, 1959]. Due to Fresnel's equations, the edge between transmission and reflection is centred at different wavelengths for s- and p-polarized light (perpendicular and parallel to the plane of incidence). Furthermore, the angle of incidence plays an interesting role.

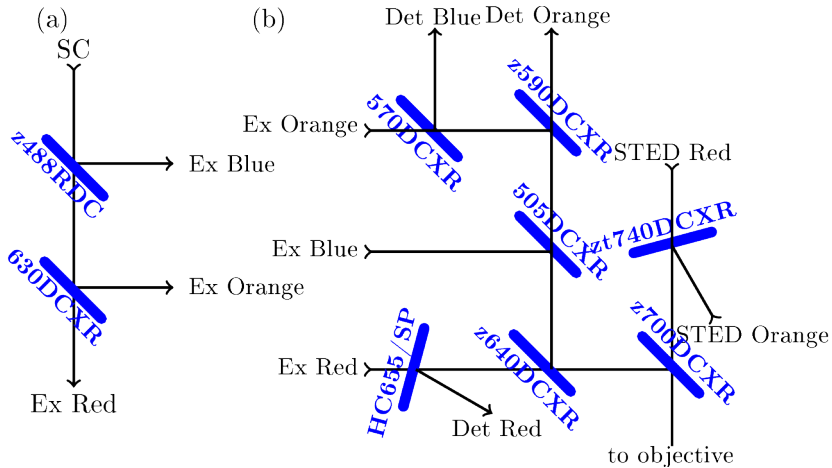


Fig. 3.4 **Dichroic mirrors:** Schematic representation of the system of dichroic mirrors used in the setup. (a) in the part splitting excitation beams from the super-continuum output. (b) in the microscope part.

The effect can be observed nicely in Fig. 3.5: *DetOrange* and *Ex/DetRed* are combined with a dichroic at 45° , and the resulting edge extends over 20 nm (*DetOrange* trans, right side and *DetRed* trans, left side). *ExRed* and *DetRed*, on the other hand, are separated with a dichroic mirror at 10° . The two dichroic mirrors have nearly the same central wavelength. Due to the steeper edge of the latter mirror (*ExRed* trans, right side and *DetRed* trans, left side), a small window is opened up for *ExRed*. Its transmission doesn't exceed 50%, but that can be compensated with laser power. With this design, the widest possible detection windows can be achieved for the two channels.

The beams split by the dichroic mirrors in the 'pre-fiber' part of the

The optical path length through the thin films changes with the angle: Therefore the edge is moved to shorter wavelengths with a decrease in angle of incidence, and the edge becomes steeper, resulting in a smaller range of wavelengths that are partly transmitted and partly reflected.

3.1 STED setup design

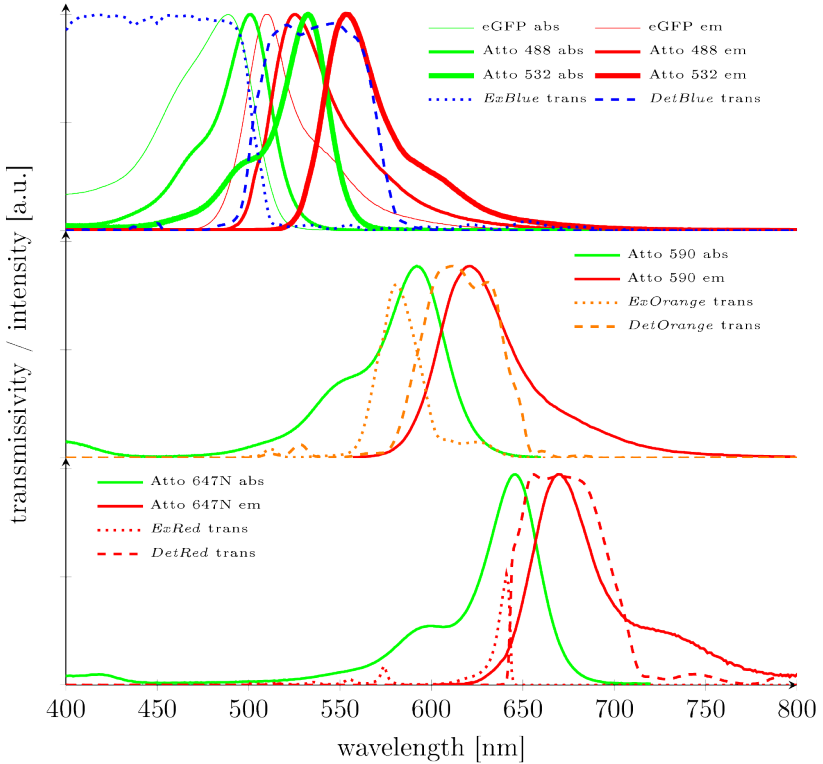


Fig. 3.5 Spectral transmittivity of beam paths: Excitation and detection beam paths of the STED microscope. Only the beam path transmittivity of dichroic mirrors are considered while the filters are omitted. Absorption and emission spectra of the dyes employed are plotted for comparison. Top: *Blue* channel. Its confocal nature allows for a wider range of fluorophores; center: *Orange* channel; bottom: *Red* channel. Spectra from fluorophores.org

excitation channel	transmission wavelength	Model number
<i>Blue</i>	(488 ± 3) nm	HC488/6
	(497 ± 8) nm	BrightLine497/16
<i>Orange</i>	(586 ± 7) nm	HC586/15
<i>Red</i>	(637 ± 5) nm	Z637/10x

Tab. 3.1 Excitation Filters: transmission wavelength and model number for all available excitation filters.

setup do not have a narrow spectrum *per se*. Laser clean up filters in front of the fiber coupling units are used to provide well-defined beam spectra for excitation. Tab. 3.1 lists the filters employed for the three channels. The *Blue* channel has a second filter for samples that are labeled with a green-shifted dye, like Atto 532.

Compared to excitation beam powers, fluorescence detection beam powers are extremely low. Therefore, it is of utmost importance to prevent any back-scattered input light from reaching the detectors. For standard fluorescence microscopy, detection filters are usually manufactured to block with an optical density (OD)² of six. A higher value should be applied to block STED light due to its higher beam power. Detection filters are employed for this task, listed in Tab. 3.2. Filters with the optimum specifications for this system were not commercially available. With the available filters, *DetOrange* is either truncated too narrowly, resulting in a low signal, or *ExRed* is not blocked. Correspondingly, the high beam power of *STEDOrange* leaks through the *DetRed* filters. Both of these cross-detection signals can be filtered out with the time-gating electronics described in section 3.1.2, but it may happen that the detectors are overexposed. To optically filter out these wavelengths while still keeping the detection windows open as wide as possible, the dependence of interference filters on the tilt angle as mentioned above was used. The broad detection filters were

²The OD is defined as the negative logarithm to the base of ten of the quotient of incident to transmitted intensity.

detection channel	transmission wavelengths	model number
<i>Blue</i>	(520 ± 14) nm	HC520/28
	(545 ± 15) nm	ET545/30
<i>Orange</i>	(615 ± 10) nm	HC615/20
	(624 ± 20) nm	HC624/40 (inclined)
<i>Red</i>	(680 ± 14) nm	HC680/26
	(685 ± 20) nm	HC685/40 (inclined)

Tab. 3.2 **Detection Filters:** specifications of the detection filters in use.

put into the beam path and tilted far enough to block the back scattered light (labelled with ‘inclined’ in Tab. 3.2).

3.1.2 Timing design

The ALP laser emits pulses of about 200 ps at a repetition rate of 20 MHz. Excitation and stimulated emission light need to irradiate the sample at the same time in order to be effective. Thus, the corresponding optical paths need to have the same lengths within about 3 mm, corresponding to 10 ps. The dependence of the STED efficiency on the path length difference is investigated in section 3.2.1.

Additionally, the pulsed radiation has been exploited for crosstalk reduction. Dyes of one channel may partially emit at a wavelength passing the detection filters for a different channel, thus giving a false signal. In the current setup, the optical paths for different channels vary in length, thus ensuring alternating excitation, separated in time by 14 ns to 18 ns³. The idea of alternating excitation (ALEX) has been put forward in the context of single molecule FRET measurements to quantify acceptor signal simultaneously to the energy transfer [Kapanidis et al., 2005]. For pulsed laser sources, the corresponding scheme is called pulsed interleaved excitation (PIE)[Müller et al., 2005]. To implement such a detection scheme, the sig-

³Pulse delay has been confirmed in a characterization measurement, see Fig. 3.8

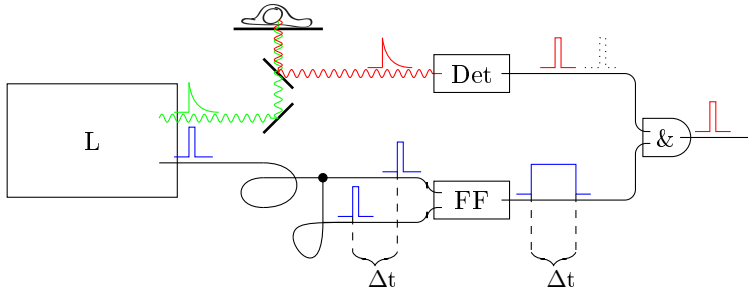


Fig. 3.6 Time-gating schematic: Synchronously to the emission pulses, the laser (L) issues electrical pulses (blue). For time-gating, two cables of different length are connected to the corresponding output to get pulses separated in time by Δt (lower part). A flip-flop (FF) is applied to these signals to yield one long pulse of length Δt . The emission light (green) excites fluorophores in the sample (top), whose emission (red) is converted to an electrical pulse by the detector (Det). Cable lengths are adjusted such that the signal (red) and the detection window reach the AND gate (&) simultaneously. This way, the signal passes while noise or cross-detection (dotted pulse) are rejected. The schematic describes a one channel setup. Colors employed in this schematic only represent different processes and do not correspond to channels.

nals coming from the detectors pass a custom made time-gating electronic circuit. This device lets the detector signals pass if they come at the right time for the respective channel, otherwise it rejects them or it relays them to a separate output (schematic of the mode of working in Fig. 3.6). It is based on flip-flops⁴ for each channel that determine time windows. During these channel assignment windows, the signal for the respective channel is expected. Detector signals coming at different times are regarded as noise or crosstalk and thus rejected. The time-gating output is generated by connecting the detector and flip-flop outputs by an AND gate. Thus, signal pulses pass only when the time window is open. For acquiring cross signals,

⁴Flip flops are electronic memory devices whose output can be switched by input signals. After such a trigger event, the output remains constant until the next switch is triggered.

flip-flops and detectors that represent different channels are connected. The flip-flops are synchronized with the laser pulses *via* a photodiode output of the laser source. The exact timing of flip-flop rising and falling edges can be adjusted by coaxial cable lengths ⁵.

3.1.3 Beam paths

As mentioned in section 3.1.1, the microscope consists of two parts. The ‘pre-fiber’ part extracts the wavelengths needed from the super-continuum laser source and couples them into single mode fibers. The ‘post-fiber’ part represents the microscope itself. Those two parts are connected by single mode optical fibers whose lengths have been chosen such that they guarantee the temporal succession of the pulses as described in section 3.1.2 without the need for excessive free-space collimated beam path length.

A schematic representation of the ‘pre-fiber’ beam paths is shown in Fig. 3.7. For clarity, the fibers connecting the ‘pre-fiber’ and the ‘post-fiber’ parts are not depicted. However, all fiber couplings in the ‘pre-fiber’ part and all beam collimations in the ‘post-fiber’ part are labelled with the respective beam names.

The ALP laser system features two outputs that are seeded from the same fiber laser source but have different frequency conversion and amplification characteristics.

A super-continuum output emits a broad spectrum in the range of 470 nm to 950 nm with an average power of 0.75 W. It is used to extract the excitation wavelengths and a beam with a broad spectrum for alignment. For a quick readjustment in case of laser exchange, there is a set of beam walk mirrors after the super-continuum source. Two iris diaphragms ensure that the beam can be realigned quickly.

A kinematic flip base enables a 50:50 splitting pellicle to be moved in and out of the beam quickly and with a high repeatability (below 100 μ rad). The reflected beam is coupled into a single mode alignment fiber. This fiber

⁵Further details of the device are presented in appendix D.3

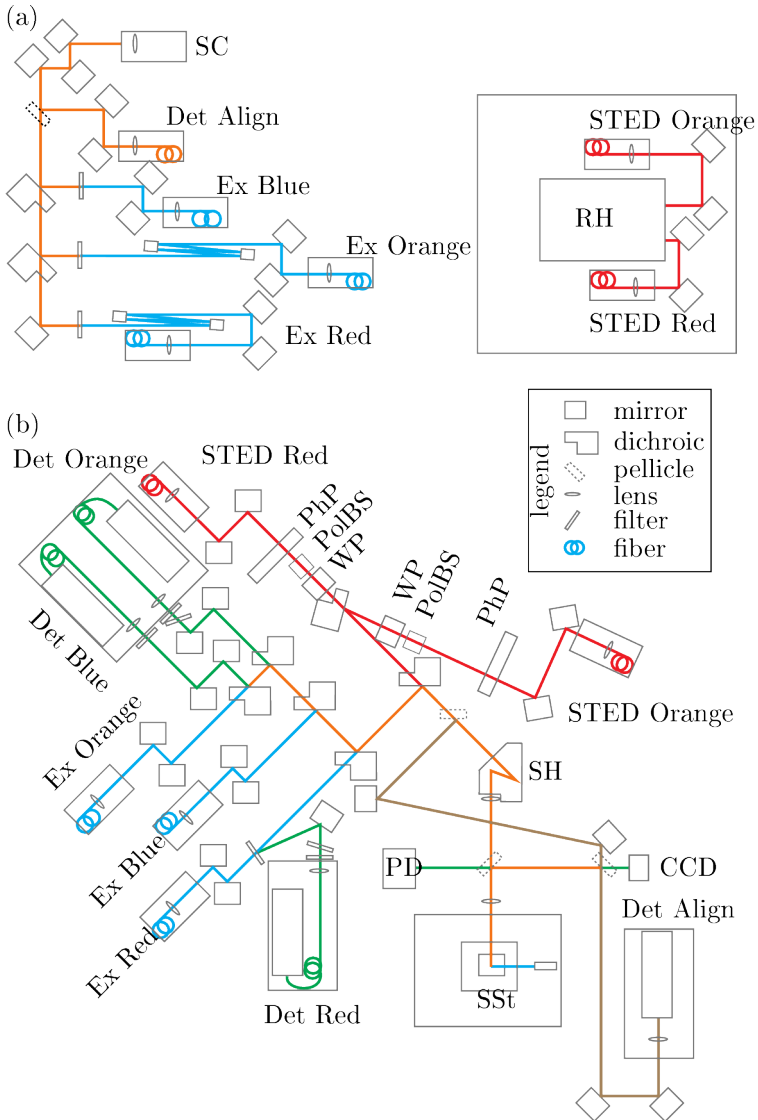


Fig. 3.7 Beam path schematic: Beam paths (a) before and (b) after the fibers are shown. Colored lines: beams. Blue: excitation beams; green: detection beams; red: STED beams; brown: alignment detection path; orange: multiple purposes. SC: supercontinuum output; RH: remote head for STED output; PhP: phase plate; WP: wave plate; PolBS: polarizing beam splitter; SH: scan head; PD: photo diode; SSt: sample stage; CCD: camera.

is then used to align the detection paths⁶. If high excitation intensities are needed, the pellicle is moved out of the beam.

The transmitted path is split with dichroic mirrors (see Fig. 3.4a) and cleaned up with the filters mentioned in section 3.1.1. The excitation paths for the two STED channels additionally feature a delay line that is built in a slimmer version than usual⁷ due to spatial requirements. Two rectangular mirrors oppose each other and the beam is reflected back and forth between them n times. One of the mirrors is located on a translation stage. Moving the stage by a distance d alters the path length by $2 n d$ ⁸.

The second output of the ALP is the remote head which has two separate amplifiers for the STED wavelengths. Emission occurs at two separate apertures. Cooling of the remote head is achieved via air fans which introduce vibrations to the platform the head is mounted to. For this reason, the remote head cannot be placed on the optical table that incorporates the rest of the setup. A separate breadboard had to be introduced and the free space optical path to the coupling unit is chosen as short as possible to ensure coupling efficiencies as stable as possible. The beams are coupled into polarization maintaining single mode fibers. For the beams not to be depolarized within the fibers, the input polarization needs to match the slow axis of the fiber. Half-wave plates in front of the coupling unit adjust the polarizational orientation appropriately.

All beams are equipped with a shutter and a dimmer. They are all controlled by a self made microcontroller-based device explained in detail in appendix D.5. The shutters move a sheet of black painted aluminium in and out of the beam to block it. The dimmers do essentially the same. However, they are not limited to two but can be set to 2^{16} positions. The aluminium sheet intercepts the beam partially, depending on the position the dimmer is set to. The sheet has a contour compensating the Gaussian

⁶See appendix C.1 for details.

⁷Delay lines are often built by putting two mirrors on one translation stage. The beam is deflected by 180° in total and the beam path length changes by twice the change in position of the translation stage. The advantage of this approach is that only little realignment is needed after a change in position. However, more space is needed in the setup and the beam is delayed by less optical path length.

⁸Appendix C.3 provides more alignment details.

profile in such a way that the beam power passing the dimmer depends linearly on the angle of the aluminium sheet. By including both shutters and dimmers, beams can be shut off and on again without any change in beam power. The truncation of the beams introduced by these devices does not harm the performance because the subsequent single mode optical fibers clean up the beam profile.

The microscope part of the setup is schematically visualized in Fig. 3.7b. Here, collimators with a focal length of 20 mm hold the fiber ends to form free-space collimated beams with a beam diameter of 3.6 mm. Two mirrors next to each collimator and detection unit enable the fine alignment needed to compensate for the daily thermal drift (see appendix C.1 for details). The STED beams undergo beam phase manipulation in the spiral phase plates (PhP) and circular polarization tuning (see section 2.4.1 for requirements and appendix C.1 for alignment) in the half and quarter wave plates (WP). All beams are combined using the set of dichroic mirrors mentioned in Fig. 3.4b. A pellicle reflecting 45% can be flipped into the beam to detect back reflected light for alignment purposes. A scan head (Yanus IV, Till Photonics) provides the possibility to acquire images via beam-scanning. It is followed by a telescope that increases the beam size by a factor of four, yielding a beam diameter of 7.1 mm in the back aperture of the objective (HCX 100x/1.4, Leica Microsystems) when the reduction of the beam diameter by the scan head by a factor of 0.488 is taken into account. A mirror in front of the objective directs the beam vertically upwards to allow for the sample to be placed horizontally on the sample stage (SSt).

Another pellicle reflecting 45% can be introduced in the beam between the two lenses of the telescope. It serves for intensity measurements using the reflection of direct light from the incident beams on a photo diode (PD). Furthermore, it reflects light from a collimated light emitting diode hanging above the objective for acquisition of bright field images on a CCD camera (WB-5400, Trust). Additionally, back scattered light reflected on either of the pellicles can be detected for alignment on a photo multiplier (Det Align). To reduce drift, the beam paths have been designed to be

kept as short and the number of mirrors as small as possible for a system of this complexity.

The sample stage comprises three servo-motorized linear stages (M404.1PD, Physik Instrumente) with a travel range of 25 mm and repeatability of about one micron. The fine position of the sample can be adjusted with a 3D piezo stage (P517.3CL, Physik Instrumente). The top surface of the sample stage is a 20×20 cm area that can easily accommodate bulky sample manipulation devices like shear or load chambers. The linear stage for the vertical axis is disburdened with springs which can be adjusted to the mass of the device put on top of the stage.

3.1.4 Control and acquisition electronics

The core building block managing all time sensitive hardware operations in the microscope is a data acquisition (DAQ) board (M-6259, National Instruments). Three of its analog outputs are used to control the scan position in three dimensions via piezo or scan head.

For detection, fluorescence light is collected using a multimode optical fiber with a diameter of $62.5 \mu\text{m}$, corresponding to 1.1 Airy units. Detection is performed with avalanche photo diodes (APD) (SPCM-AQRH-13, Perkin Elmer; CountBlue, LaserComponents). These are single photon counting modules and output 15 ns TTL⁹ pulses for every photon detected. This signal is optionally fed through the time-gating device (see section 3.1.2) and eventually enters the counting unit. Four channels can be detected simultaneously, these being *Blue*, *Orange*, and *Red* fluorescence and one additional cross-detection channel. The DAQ board used only incorporates two counters. Therefore, two additional counters are brought about by a programmed complex programmable logic device (CPLD) (see appendix D.4 for details) with two 16 bit outputs. These outputs are fed into the digital IO lines of the DAQ board. Synchronization of the four counters with the scanning device is achieved with an analog output trigger from the DAQ board which issues a rising edge with every new output value.

⁹low: below 2.1 V, high: above 2.3 V

3.2 Characterization

Before setting to work with a newly built setup, it is essential to fine tune and characterize it and determine its performance concerning various aspects. Many of the observables defined in the previous chapters are inaccessible to the experimenter, so other, but related, parameters need to be found to optimize the system. For example, when the conditions for a good donut were discussed in section 2.4.1, it was stated that the right orientation of circular polarization is needed. This section is concerned with means of quantifying this polarization and finding criteria to decide which level of alignment quality is required and sufficient.

Polarization being but one example, special care has been taken to characterize the system concerning timing issues, the resolution achievable, and the efficiency of detection.

3.2.1 STED pulse timing

The excitation pulses for the three channels were delayed in time with respect to each other as mentioned in section 3.1.2 to provide pulse interleaved excitation. To verify the time offset between the pulses, they were measured on a time correlated single photon counting (TCSPC) setup. Conveniently, this detection scheme was available on a setup in the same room and the combined beams could be directed on the corresponding detectors (PDM, PicoQuant GmbH, 1 ps timing accuracy) easily. Synchronization of the TCSPC detection unit with the STED laser enabled pulse timing measurements with a time resolution of 16 ps. Fig. 3.8 shows the resulting plot. The time axis covers the whole repetition time of 50 ns. Consequently, the three pulse times are equidistantly distributed.

For an efficient deployment of the STED photons, the time delay between the two pulses for the STED channels, displayed at 5 and 22 ns need to be aligned accurately. An early STED pulse wastes photons that cannot de-excite any molecules because they have not yet been excited by the excitation photons. If, on the other hand, the STED pulse starts too late, the probability of spontaneous fluorescence becomes unacceptably high, resulting in confocal background. In order to determine the best time lag

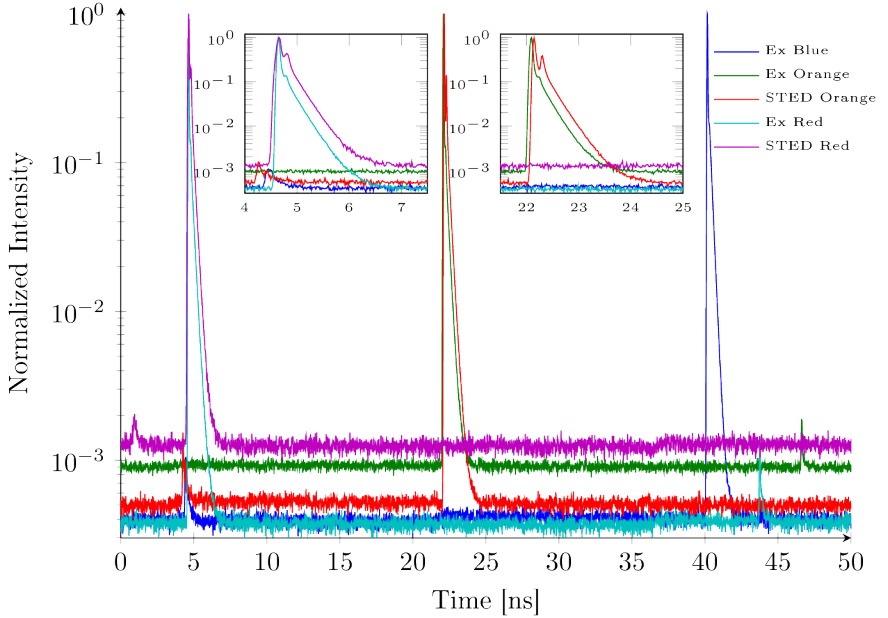


Fig. 3.8 Pulse timing of input beams: Beams for one channel essentially radiate at the same time; for different channels, they are offset in time by about a third of the repetition rate.

between excitation and STED pulses, the STED efficiency was measured as a function of delay time (Fig. 3.9). For each time lag value, a μM solution of free dye was probed with the excitation alone and both excitation and STED beams on. The acquisition took place at a constant point in space, and 10^4 data points were acquired, each for 1 ms. The traces had a constant level, indicating that bleaching was not an issue and the dye molecules diffused out of the focus before getting bleached. The mean value of these traces yielded the signals S_{ex} and $S_{\text{ex+STED}}$. As a measure of how efficiently the STED photons are employed, the STED efficiency is introduced as the

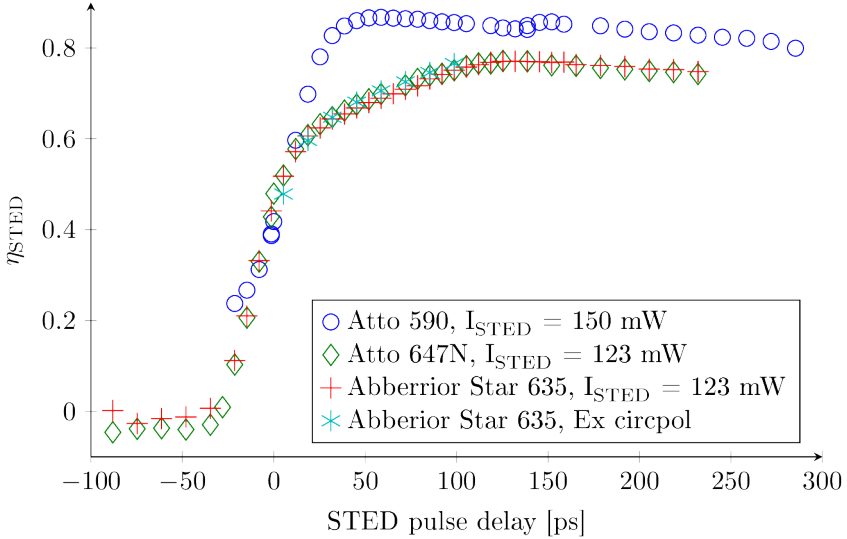


Fig. 3.9 STED efficiency and pulse delay: For the *Orange* channel (Atto 590) and the *Red* channel (Atto 647N and Abberrior Star 635), the details of the curve differ. This does not depend on the dye employed or the polarizational state of excitation.

normalized loss of signal due to stimulated emission,

$$\eta_{\text{STED}} = \frac{S_{\text{ex}} - S_{\text{ex+STED}}}{S_{\text{ex}}}. \quad (3.1)$$

Time lags were set by adjusting the delay lines of the excitation beams described in section 3.1.3. To calculate the absolute time lags, the time lags of the pulses in the TCSPC measurement (Fig. 3.8) were added to the difference in delay line length.

When the STED pulse delay has large negative values, all STED light hits the sample before the dyes are excited. Therefore, no stimulated emission can take place. Indeed, the STED efficiency even assumes negative

values. This accounts for the fact that the STED beam does excite the fluorophores. The excitation cross-section at the STED wavelength is very low but the the STED beam power is about three orders of magnitude higher than the excitation beam power, which partly compensates the difference in cross-section.

As the STED pulse delay approaches simultaneity with the excitation pulse, the STED efficiency rises steeply. This happens due to the fact that excitation is an instantaneous process and internal conversion from excited vibronic states of S_1 to its vibronic ground state occurs very fast. For rhodamine dyes, it happens within a picosecond [Penzkofer et al., 1976]. The order of magnitude can be expected to be the same for all organic fluorophores.

For long delays of the STED pulse, the efficiency slowly decreases, reflecting the decay of S_1 by spontaneous fluorescence with a lifetime of typically 3 ns to 5 ns.

Interestingly, the shape of the curve differs substantially between the *Orange* and the *Red* channel for moderate delays. For the *Orange* channel, the two processes of increase and decrease that were just mentioned directly follow each other while the *Red* channel shows an intermediate flat increase in STED efficiency. This intermediate does not depend on the dye used, nor on the polarization state of the excitation beam. Dyes from two different manufacturers were investigated and measurements with elliptical and with circular excitation polarization were performed. The plot shows that all those measurement curves overlap. However, a different trend of the curve can arise from pulses shaped differently in time. As perceivable in the insets of Fig. 3.8, especially the STED beams have a different shape. The difference probably arises from different multiple reflections in the setup but the case was not investigated further.

The maximum of the STED efficiency curve corresponds to the optimal pulse delay and the delay lines were set to 50 ps for the *Orange* and 100 ps for the *Red* channel.

3.2.2 Polarization dependence of the donut

The signal to noise ratio (SNR) in STED images is inherently lower than in confocal images because the effective PSF is narrower, so fewer photons contribute to the signal. To keep the SNR to a maximum level for a given resolution, the peak of the STED PSF needs to be maintained as high as possible. That means the detection probability at the focus is to be maximized. The main cause for its decrease is residue STED light in the donut minimum that causes excited fluorophores to undergo stimulated instead of spontaneous emission and thus do not contribute to the detected signal. Therefore, a point of major concern for best quality imaging is to form a donut with a center that approaches zero intensity. Section 2.4.1 introduced the importance of polarization to the donut center. Here, the impact of STED beam polarization to the detected signal is investigated.

The investigation is performed by tuning the STED beam to adopt various states of elliptical polarization. To realize that, the orientation of linear polarization incident to a quarter wave plate is altered.

Quantification of the polarizational state of the STED beam is performed with a custom built analyzer. It consists of a linear polarizer mounted on a motor, followed by a photodiode. The intensity transmitted originates from the polarizational fractions of the beam which are parallel to the current orientation of transmission of the polarizer. The rotating polarizer probes all directions in succession. Thus, linearly polarized light yields sinusoidal intensity characteristics, while the transmitted intensity becomes constant with circular polarization. A power spectrum of the acquired data has an according peak at twice the frequency of rotation. The height of this peak serves as a measure of circular polarization alignment quality. The more circular the polarization, the lower the peak gets¹⁰.

This peak height, the donut minimum relative to the rim value, as well as the resulting fluorescence signal of a sample of labelled beads is plotted against the angle of linear polarization incident to the quarter wave plate in Fig. 3.10. Images of the depletion pattern are shown for three points. It can be seen at once that donuts with a low minimum value additionally have a

¹⁰For details of the device, see appendix D.2.

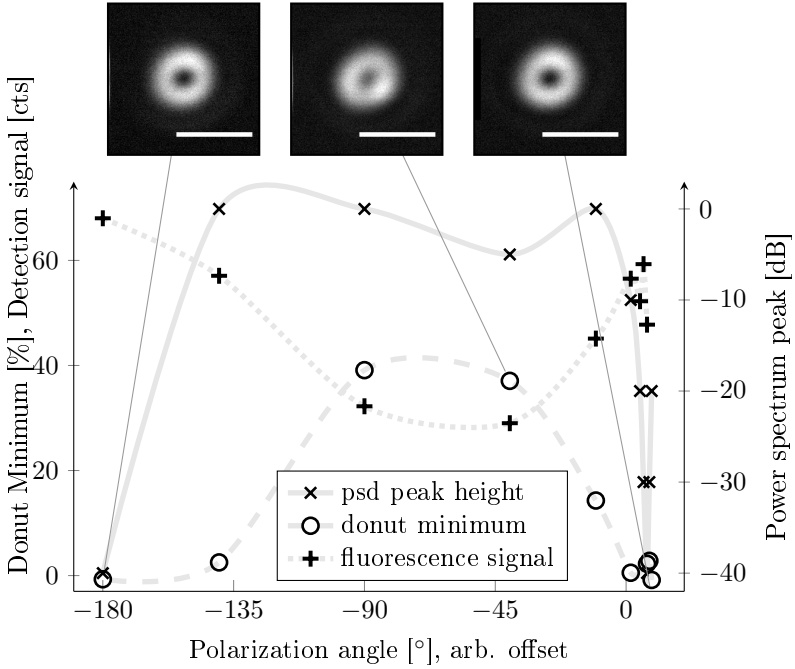


Fig. 3.10 Polarization and depletion pattern: Circular polarization quality (x), donut minimum quality (o), and the resulting signal (+) are plotted against the angle of linear polarization incident to the $\lambda/4$ -plate. To give an impression of the evolution of the quantities, splines to the data points are plotted in grey. These do not have any physical implication and are included only to guide the eye. The donut minimum is lowest when the circular polarization is best and its power spectrum peak is lowest. Then, the signal is highest. Images of depletion patterns at selected points are included. scale bars: 1 μm .

higher symmetry, resulting in a more symmetric STED PSF. Furthermore, they occur when the PSD peak value is low and yield best detection signals.

The circular polarization is measured with the objective removed. Fluorescence signal and depletion pattern acquisition need different samples. Therefore, the measurement needed to be performed in three steps. First, the polarizational state was measured for a set of angles. Then, the objective was put in place and a sample of gold beads was mounted. After the measurement of depletion patterns, the fluorescence signal was collected for different angles with a sample of fluorescent beads mounted. This procedure increased the error in angle position. Another issue of concern is that when the setup has been in operation for less than 24 h non-stop, the system has not stabilized. Thus, the angle for best circular polarization tends to change slightly. Therefore, the data points for a PSD peak lower than -20 dB need to be considered with caution¹¹. To conclude the investigation, however, it is safe to suggest the alignment of circular polarization to -20 dB. This is easy to do after laser warm-up of half an hour and yields good signal values.

3.2.3 Time-gating

As already proposed in section 3.1.2, the time-gating electronics serves two functions: for one, it decreases unwanted crosstalk between the channels, and for another, it facilitates the disentanglement of two different kinds of signal out of one detector. Examples for these are FRET (section 4.3) and reflectance signals, called cross detection signals in the following. These originate from the same detector, but are issued at times dedicated to different excitations.

To correctly extract regular detection from cross detection signals, careful adjustment of the coaxial cable lengths was necessary. The device

¹¹Additionally, fluorescence data has been acquired from low to high angles. To be able to compare the signal results, the same area had to be scanned. Therefore, bleaching may influence the results. For a more significant measurement, the laser should be emitting for at least a day, and the fluorescence should be acquired in two spots and in opposing succession of the input angles. Then, the results can be normalized by confocal signal and added to circumvent the influence of photobleaching.

was aligned and characterized using a 400 MHz low-noise oscilloscope (WaveRunner 44MXi-A, LeCroy). All alignment measurements were performed with a timing reference triggered with the input laser trigger signal¹². For all measurements, signals were fed through coaxial cables of the same length to ensure correct timing assignment. In this way, all acquired data were automatically synchronized to the same time base.

In order to be able to use cross detection signals, detector pulses provoked by one light pulse in the sample in different detectors need to enter the time gating electronics at the same time. That ensures each channel assignment window to work on pulses from all detectors. Fig. 3.11 shows traces from all detectors. The emission was synchronized by ensuring that incident light only came from *ExBlue*. For every channel, 50 traces are displayed to roughly visualize the timing probability distribution. The width of this distribution is inconveniently large, especially when one keeps in mind that the pulse repetition time is 50 ns.

The following paragraph shows that this distribution is due to photo-physical properties of the dye and cannot be narrowed down by tuning the detection electronics. Cumulative histograms of the occurrence of the rising edges in Fig. 3.11 are plotted in Fig. 3.12. To fit an exponential decay to a cumulative histogram, the corresponding function needs to be integrated under consideration of the starting time,

$$N = A \cdot \tau \cdot \left(1 - e^{-\frac{t-t_0}{\tau}}\right) \cdot \Theta(t - t_0). \quad (3.2)$$

For fitting, the data is normalized, thus the factors can be omitted. Θ stands for the Heaviside step function. The fitted onset times show a synchronization of the detectors that fits well to the needs of the time-gating

¹²With a simple trigger set at the laser signal, a trigger event is executed when the laser signal arrives, without regard to the signal in the channel under investigation. This signal mostly stems from fluorescence, and is issued only from a small fraction of laser pulses. Thus, most recorded traces are empty of relevant data. When the trigger is set to the relevant channel on the other hand, more effort is needed to extract the right timing.

The WaveRunner oscilloscope features a very useful trigger mode that allows to trigger at the rising edge of the laser signal, but only when the investigated signal has a rising edge within the previous 50 ns. This ensures that there is a trace of the signal under investigation, but with the correct timing offset.

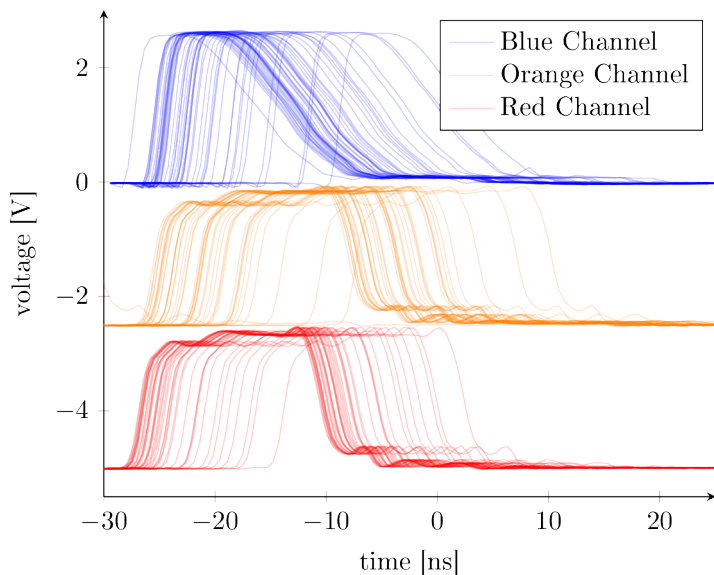


Fig. 3.11 Detector Synchronization: For efficient cross-signal detection, pulses from various detectors issued by the same pulse need to reach the time gating electronics at the same time. Here, detector signals from blue, orange, and red detectors are shown in corresponding colours. The latter are offset by 2.5 V and 5 V, respectively, for better visibility. All signals were caused by blue excitation. The finite fluorescence lifetime of the dyes causes the various traces for the same channel not to overlap exactly.

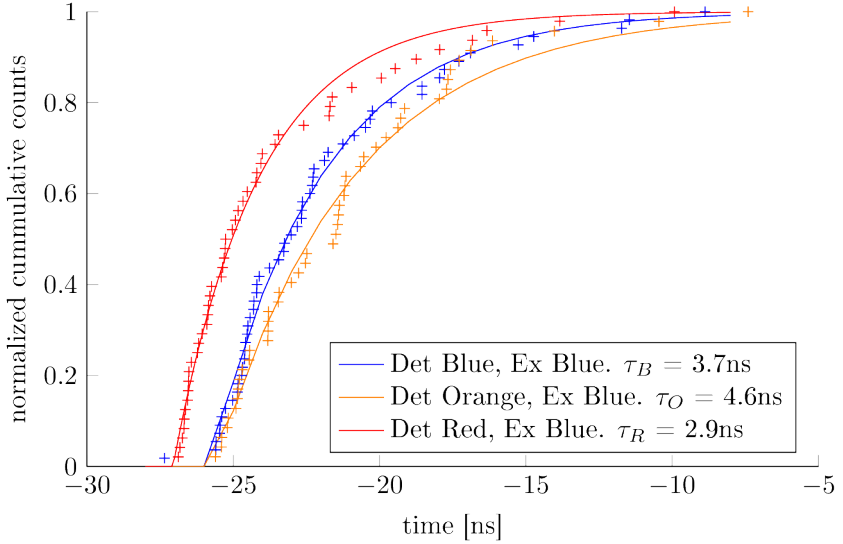


Fig. 3.12 Detector Pulse Distribution: Time distribution of detector pulse rising edges. An exponential decay fits accurately and reveals the fluorescence lifetimes of the dye. Onset times are -25.8 ns, -25.6 ns, and 27.1 ns for the *Blue*, *Orange*, and *Red* channels, respectively.

input. The lifetime of the fluorophore employed (FluoroSpheres540/560, Invitrogen, Life Technologies) is not known. However, the fitted decay times are in the regime of typical fluorophore excited state lifetimes. The input laser pulse width and detector timing precision are one to three orders of magnitude shorter. Hence, the distribution of detector signals is limited by the fluorophore characteristics and cannot be narrowed down any more.

For the correct adjustment of the channel assignment windows via coaxial cables, their signal propagation velocity was determined. It is lowered compared to stranded wire cables due to capacitive coupling. Because of the high timing accuracy needed, the influence of BNC connectors joining

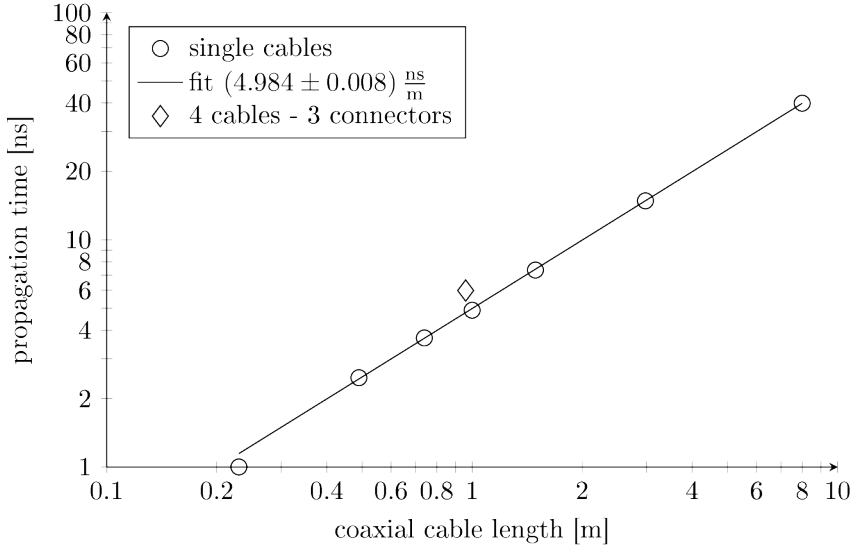


Fig. 3.13 **Pulse propagation velocity:** Propagation of pulses through coaxial cables of various length. Four cables connected by 3 BNC connectors delay the pulses by 1.2 ns with respect to one cable of the same length.

coaxial cables was of interest, too. Fig. 3.13 shows that the velocity is $20 \frac{\text{cm}}{\text{ns}}$, which equals two thirds of the speed of light. One BNC connector delays the pulse by further 400 ps.

The channel assignment windows were recorded by applying a constant voltage of 5 V to the detector inputs of the time-gating device, thereby ensuring that the AND gate always followed the channel assignment windows and monitoring the channel outputs. Thereby, however, the signal passed the AND gate whereas the recorded signal for recording the detection did not. Hence, for comparing the detector and the channel assignment window signals, the passage time through the AND gate of 3 ns has to be taken into consideration. Fig. 3.14 shows the detector signals delayed by 3 ns, the channel assignment windows, and the time gating outputs from top to

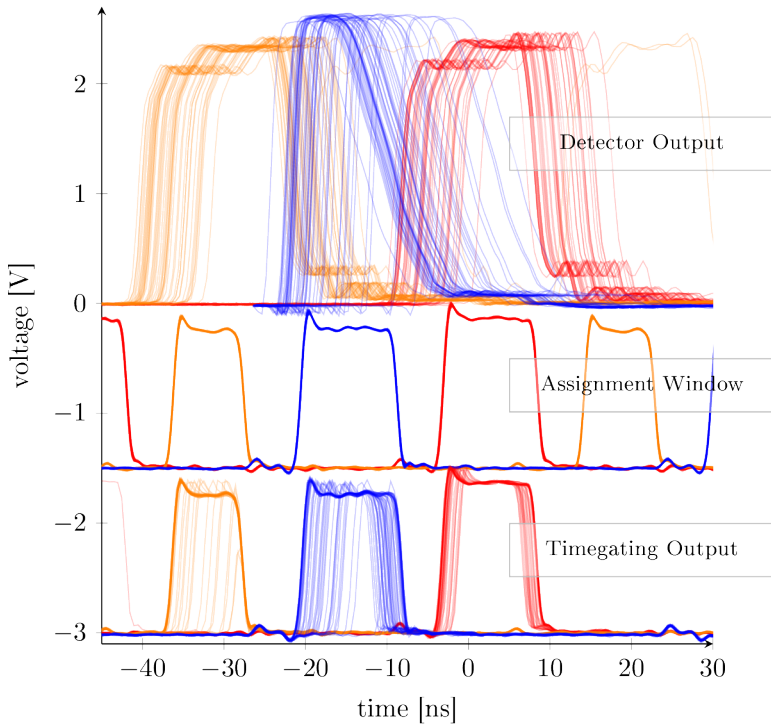


Fig. 3.14 **Time Gating:** Detector pulses (upper part, shifted by 3 ns to correct for the AND gate propagation time), Detection assignment windows (middle, offset by -1.5 V), and time gating output (lower part, offset by -3 V).

channel	detector	delay	window
<i>Blue</i>	1.5 m	10.25 m + 2 conn.	3.5 m + 1 conn.
<i>Orange</i>	4.75 m + 2 conn.	6.5 m + 1 conn.	3.5 m + 2 conn.
<i>Red</i>	2.5 m	3.75 m + 2 conn.	3.5 m + 1 conn.

Tab. 3.3 Detection Time Gating Cable Lengths: Coaxial cable lengths for all relevant parts of the time gated detection. detector: cable between detector and time-gating device. delay: cable to delay the laser clock for the single channels within the time-gating device. window: cable determining the length of the channel assignment windows.

bottom, respectively. The lower traces are offset by -1.5 V each for better readability. For a measurement, only the corresponding excitation beam was in operation. The cable lengths at the time of measurement are listed in Tab. 3.3¹³

To investigate the effect of the time gating device, fluorescently labelled beads were scanned and detected directly as well as using the time gating device. Hereby, the excitation beam was chosen to match the absorption spectrum of the respective dye, while all detector channels were monitored. Fig. 3.15 compares not timegated with timegated acquisition. Note that crosstalk is most prominent between the two STED channels. This is because they have been chosen to be spectrally close to accommodate the STED wavelengths. Hence, for good-quality two-colour STED imaging without the need of post processing methods like spectral unmixing, time gating is essential. By using the time gating device, crosstalk becomes negligible.

However, the timing requirements push the scheme to the limits. With

¹³The cable connecting the laser clock output with the time-gating device measured 17 m. Keep in mind that these synchronization were performed with the orange and red signals being fed through their detector power supply (DSN 102, SN: 01014632, PicoQuant GmbH) which monitors and thereby delays the pulses by a few nanoseconds. Due to individual passing times, the serial numbers B8326 for the *Blue*, 17855 for the *Orange*, and 19966 for the *Red* detector are relevant.

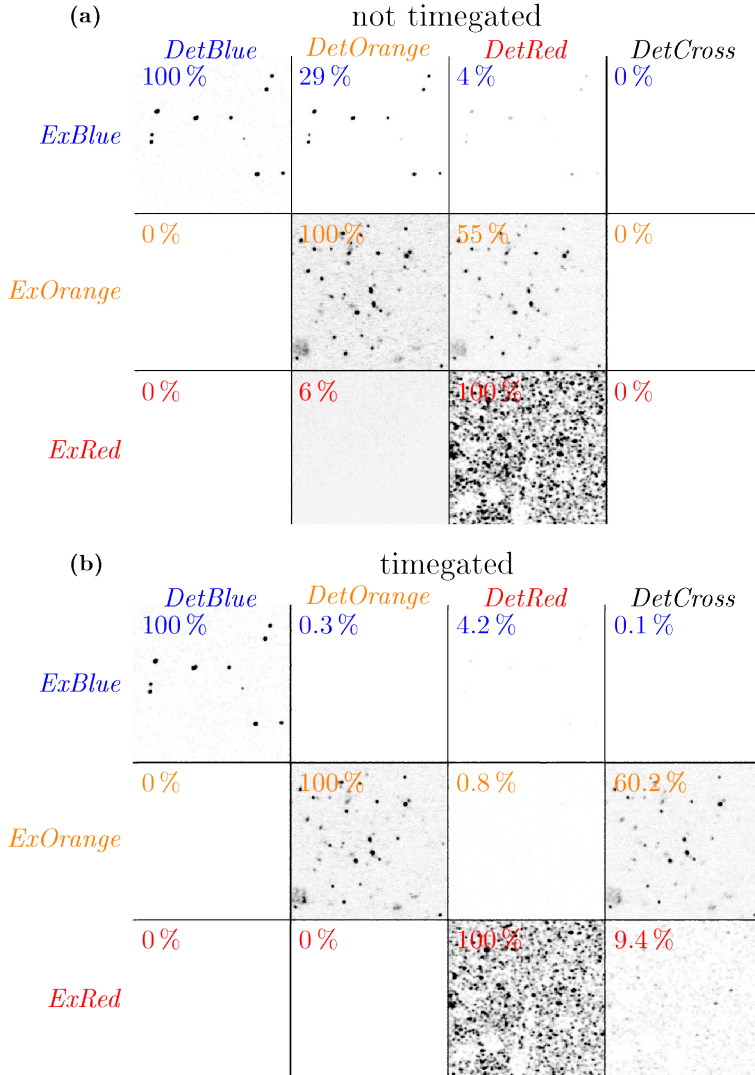


Fig. 3.15 **Crosstalk without and with time-gating:** (a) No time-gating enabled (b) time-gating active. Columns from left to right: *Blue*, *Orange*, *Red* detection, and cross talk signal *Red* detection at time of *Orange* assignment window (with time gating only). Rows from top to bottom: *Blue*, *Orange*, and *Red* excitation. Annotations represent the image counts relative to the regular detection channel. Note that the cross signal moves into the crosstalk channel when time-gating is switched on.

a pulse repetition time of 50 ns, three channels, and a detection counter running at 100 MHz, some of the time gating output pulses are bound to be too short to be counted. To quantify this, image counts with and without time-gating were compared. These are the diagonal fields in Fig. 3.15. For the *Blue*, *Orange*, and *Red* channel, the count sustainment efficiencies amounted to 69 %, 67 %, and 80 %. With longer channel assignment windows, these values can be increased at the cost of a worse crosstalk reduction.

3.2.4 Chromatic aberration

In a beam scanning microscope, chromatic aberrations are mainly due to the insufficient chromatic correction of objective and scan lens. In this case, a plan-apochromat objective and a Till Photonics scan lens are employed in the setup. Leica's proprietary scan lens, which best counters to their objective, is available for purchase only in their complete microscope systems. Due to this fact, images of the current setup show chromatic aberrations that become non-negligible at large off-axis positions. That is, when beam scanning, the PSF maxima of the different channels separate more in space the more the probing spot is moved away from the optical axis.

Fig. 3.16 shows the results of an investigation of the chromatic aberration in the system. In the case at hand, aberration is taken to be the lateral misposition of a confocal spot. The deviations of the acquired PSF of deflected beams from the position the beam is set to is shown in Fig. 3.16a for a beam deflection in x direction, while Fig. 3.16b shows the same for y direction.

The proportionality parameter to convert a desired position in the sample to output voltage for the scan head was set using *ExOrange*. Therefore, this channel is arbitrarily set to show no chromatic aberration.

Notably, the aberration is significant only in the direction the beam is deflected to. The other direction exhibits only the same cross axis tilt as *ExOrange*. The slopes of the plots equal the relative change in magnification $\delta M/M$. The fitted values for both deflection directions are plotted in Fig. 3.17. Due to cylindrical symmetry, measurements in x and y dis-

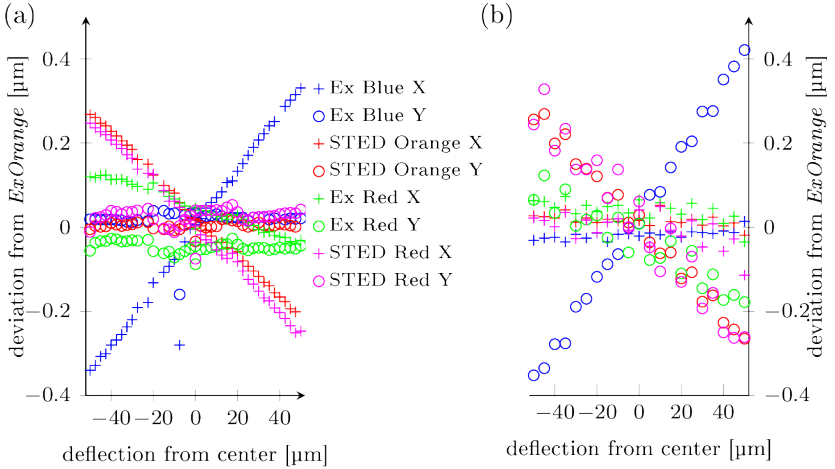


Fig. 3.16 Chromatic Aberration: The deviations Δx and Δy from the set point are plotted for For deflections in (a) x and (b) y . The farther the beam is deflected from the optical axis, the more drastic is the chromatic aberration. As this kind of aberration has a radial dependence, and piezo and scan head axes are well coaligned, only the deviated axes show chromatic aberration.

play the same response. Chromatic aberration is calculated analytically in literature[Born and Wolf, 1993a]. For the investigation here, a very crude approximation suffices. Assuming the optics to consist of a single thin lens, one finds that the change in magnification depends linearly on the change of the refractive index relative to a reference wavelength.

Fused silica is a common substrate for optics components. Its dispersion has been measured[Malitson, 1965], and is plotted in Fig. 3.17. The separate y axis is offset such that the curve matches the data at the reference wavelength of 586 nm and its scale is adjusted to coarsely fit the course of the data. Strikingly, there really seems to be a linear dependence of the relative magnification measured with the dispersion of fused silica. This is the case even though the objective, being an apochromat, is corrected

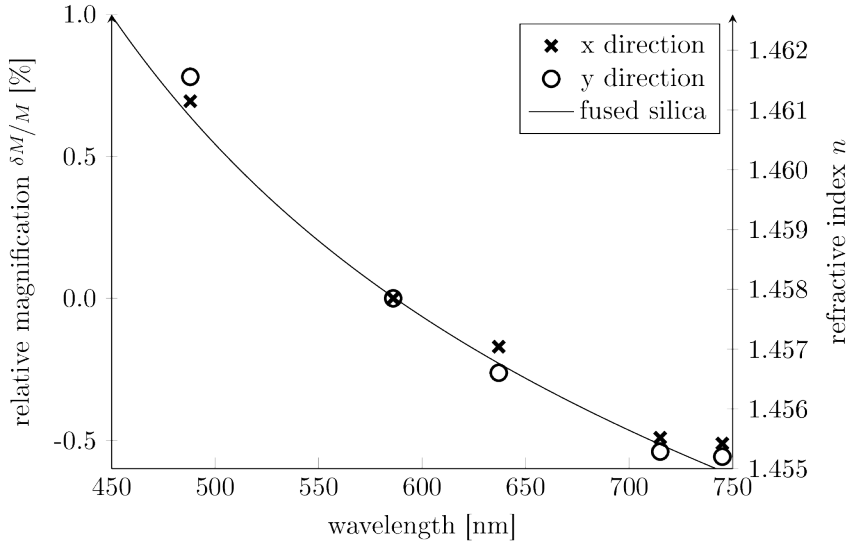


Fig. 3.17 Chromatic Aberration - wavelength dependence: The magnification relative to that of *ExOrange* $\delta M/M$ decreases with the wavelength for both x and y directions. To compare, the dispersion of fused silica is added to the plot.

against chromatic aberration at three wavelengths, and the scan lens is corrected as well. These corrections do not result in a distorted chromatic response of the system but probably in a decrease in the scaling factor leading to the relative magnification.

For STED imaging, the positional difference between the two STED beams is of most importance. It directly affects multi channel imaging. Signal originating from one spot in two channels may be interpreted wrongly as separate emitters. Due to the higher resolution, demands are higher than for the confocal beam. On the other hand, excitation to STED mismatch decreases intensity but not spatial information. This difference between the two STED beams is negligible for deflections Δx , $\Delta y < 10 \mu\text{m}$, so

the chromatic aberration can be neglected for the typical STED scans of $20 \times 20 \mu\text{m}^2$. To ensure that the area to be imaged is centred, a software-based approach has been chosen. When an area is selected for imaging, the sample is automatically centred correctly when the corresponding option is chosen.

3.2.5 Resolution scaling

In STED microscopy, the resolution of an image depends on the applied STED beam power. It obeys the law discussed in section 2.4.2

$$\text{FWHM}_{\text{STED}} = \frac{\text{FWHM}_c}{\sqrt{1 + \text{FWHM}_c^2 \frac{I_{\text{STED}}}{I_s} a^2}}. \quad (3.3)$$

with the saturation factor $\zeta = I_{\text{STED}}/I_s$ and the donut minimum form factor a . The saturation intensity I_s is a property of the fluorophore and the wavelength employed and therefore the law can depend on the dye in use.

A test of the resolution dependence determines the quality of the alignment and elucidates the resolution achievable. In earlier, similar characterizations [Harke et al., 2008], the law was fitted to the data by using the confocal resolution as well as the form factor a as fit parameters. Here, additionally, the possibilities of determining the parameters separately instead of fitting are explored.

With the parameters elucidated, the resolution scaling dependence can be evaluated. Single molecules were scanned at various STED beam powers and the widths of their images evaluated. The resulting curves are shown in Fig. 3.18 with the standard deviation of the widths as error bars, for the design dyes of the two STED channels, Atto 590 and Atto 647N. The data for for both fluorophores was fit to the resolution law. Notably, the difference in fitted confocal width reflects the different wavelengths, while the scaling parameter is very similar for both channels. The green curve in the plot is calculated without a fit by using experimentally obtained parameters. For calculating the resolution, three parameters are needed: the confocal width FWHM_c , the saturation intensity I_s , and the form factor

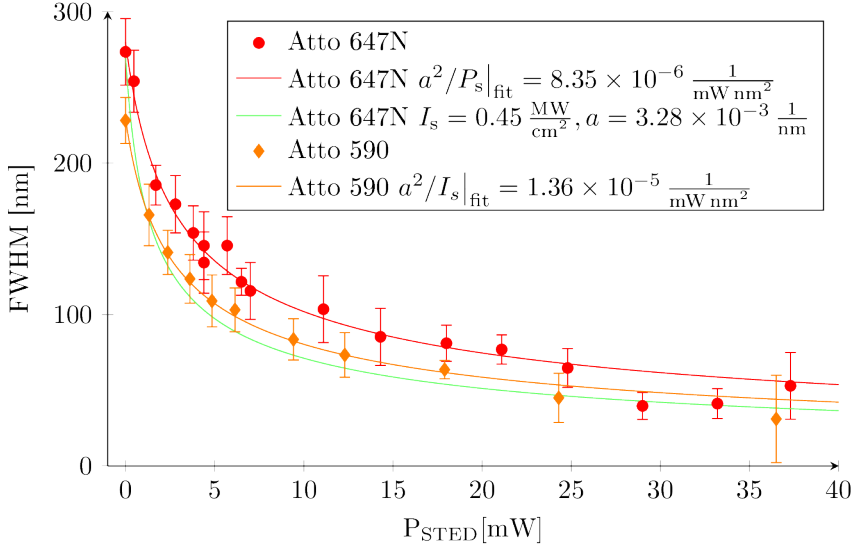


Fig. 3.18 **Resolution Scaling:** FWHM of single molecule images versus STED beam power for Atto 590 (orange) and Atto 647N (red), including fits. The fit to the *Orange* data yields $\text{FWHM}_c = 229 \text{ nm}$ and $a^2/P_s^{\text{donut}} = 1.36 \times 10^{-5} \frac{1}{\text{mW nm}^2}$. In contrast, the *Red* data fits to $\text{FWHM}_c = 279 \text{ nm}$ and $a^2/P_s = 8.35 \times 10^{-6} \frac{1}{\text{mW nm}^2}$. The green curve relies on parameters obtained in separate experiments for Atto 647N (see text for details).

a. The next few paragraphs point out experiments performed to get access to these parameters.

The confocal FWHM can easily be determined from a measurement without the use of the STED beam. It corresponds to the first data point in a resolution scaling experiment like shown in Fig. 3.18. For the Atto 647N experiment, this value has been determined to 270 nm.

The second parameter to be elucidated is the saturation intensity. To do this, the STED beam was deprived of the phase plate to yield a confocal beam shape in the focus, overlapping with that of the excitation beam. Then, fluorescence depletion by stimulated emission was measured for various STED beam powers.

In order to extract the saturation intensity from such a measurement, a few considerations concerning the Gaussian shape of the intensity distribution are necessary. To start with, similarly as in section 2.4.2, the detected signal is the integration over the focal plane of excitation and detection PSFs multiplied with the quantum yield for spontaneous fluorescence. The PSFs can be combined to the confocal PSF while the quantum yield is described by the decay rates.

$$\begin{aligned}
 S_{\text{det}} &= \iint rd\varphi dr \text{PSF}_{\text{ex}} \eta_{\text{fl}} \text{PSF}_{\text{det}} & (3.4) \\
 &= \iint rd\varphi dr e^{-\frac{r^2}{2\sigma_c^2}} \frac{k_{\text{fl}}}{k_{\text{fl}} + k_{\text{STED}}(r)} = \iint rd\varphi dr e^{-\frac{r^2}{2\sigma_c^2}} \frac{I_s}{I_s + I_{\text{STED}}(r)} & (3.5)
 \end{aligned}$$

The intensity distribution of STED light is a Gaussian with standard deviation σ_s . Its pre-factor is set by the fact that the integration over the whole plane equals the beam power. The intensity patterns show a radial symmetry, enabling the integration over the azimuth to be carried out instantly.

$$S_{\text{det}} = 2\pi \int r dr e^{-\frac{r^2}{2\sigma_c^2}} \frac{I_s}{I_s + \frac{P_{\text{STED}}}{2\pi\sigma_s^2} \exp\left(-\frac{r^2}{2\sigma_s^2}\right)} \quad (3.6)$$

$$\stackrel{\sigma = \sigma_c = \sigma_s / \sqrt{2}}{=} 2\pi \int r dr \frac{\exp\left(-\frac{r^2}{2\sigma^2}\right)}{1 + \frac{P_{\text{STED}}}{2\pi\sigma_s^2} \frac{I_s}{I_s} \exp\left(-\frac{r^2}{4\sigma^2}\right)} \quad (3.7)$$

Here, it has been assumed that the Gaussian widths of excitation, detection, and STED probabilities have the same value. This neglects their difference due to their wavelengths. An integral of that form can be solved analytically with the help of a symbolic integration program or a good

guess

$$\int dx \frac{x e^{-ax^2}}{1 + be^{-\frac{ax^2}{2}}} = \frac{\ln\left(1 + be^{-\frac{ax^2}{2}}\right) - be^{-\frac{ax^2}{2}}}{ab^2}. \quad (3.8)$$

Hence, integration over the whole range yields

$$S_{\text{det}} = \frac{8\pi\sigma^4 I_s}{P_{\text{STED}}} - \frac{32\pi^2\sigma^6 I_s^2}{P_{\text{STED}}^2} \ln\left(1 + \frac{P_{\text{STED}}}{4\pi\sigma^2 I_s}\right) \quad (3.9)$$

As the measurement data is normalized to its initial value, so should the model function be. With the rule of de l'Hospital, it is found that $S_{\text{det}}|_{P_{\text{STED}}=0} = \sigma^2$. Hence, the normalized dependence of fluorescence signal on the applied STED beam power with overlapped Gaussian beam shapes is

$$S_{\text{det}}^{\text{norm}} = 2 \frac{4\pi\sigma^2 I_s}{P_{\text{STED}}} - 2 \left(\frac{4\pi\sigma^2 I_s}{P_{\text{STED}}}\right)^2 \ln\left(1 + \frac{P_{\text{STED}}}{4\pi\sigma^2 I_s}\right) \quad (3.10)$$

The approximation made as well as a small misalignment of the beams by 20 μm (see Fig. 3.19, inset) introduces a slightly altered shape at the curve for high STED powers. This could be taken into consideration in first approximation by introducing an offset to the curve. For the standard deviation of the Gaussians, the confocal FWHM is employed (see later in this section),

$$\sigma = \frac{\text{FWHM}}{2\sqrt{2\ln(2)}} = \frac{270 \text{ nm}}{2\sqrt{2\ln(2)}} = 115 \text{ nm}. \quad (3.11)$$

A fit to the data is shown in Fig. 3.19 and yields a saturation intensity of $I_s = 0.45 \frac{\text{MW}}{\text{cm}^2}$.

As a side note, the cross-section for stimulated emission can be determined by use of the saturation intensity. To this end, the statement from eqn. 2.21 is employed, which states that at the saturation intensity, the rate of stimulated emission and for spontaneous fluorescence are the same. Combining this with the relation for the rate of stimulated emission in eqn. 2.14 yields

$$k_{\text{fl}} = \sigma_{\text{STED}} I_s \frac{\lambda_{\text{STED}}}{h c}. \quad (3.12)$$

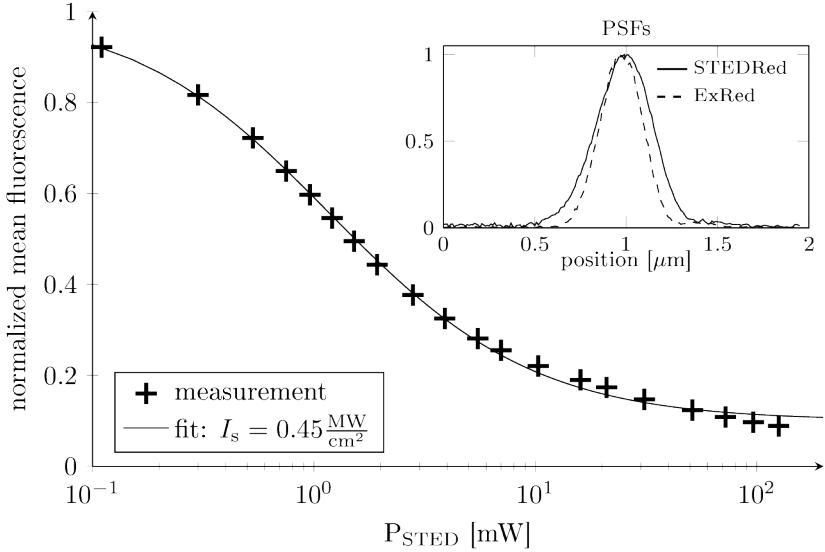


Fig. 3.19 **Saturation Intensity Atto 647N**: Detected fluorescence versus input STED beam power. The measurement was performed with both excitation and STED beam featuring a Gaussian shape (inset).

Considering that the rate of spontaneous fluorescence is the inverse of the product of fluorescence life time and quantum yield (specified by the manufacturer to be 3.5 ns and 0.65, respectively, for Atto 647N), the cross-section can readily be calculated.

$$\sigma_{\text{STED}} = \frac{hc}{\tau_{\text{fl}}\eta_{\text{fl}} I_s \lambda_{\text{STED}}} = 2.61 \cdot 10^{-16} \text{cm}^2 \quad (3.13)$$

In the following, only the saturation intensity will be employed. Nonetheless, the cross-section may prove an interesting parameter at later times.

Finally, the form factor of the depletion pattern a needs to be determined. It was introduced in section 2.4.2 as a factor of a parabola that fits

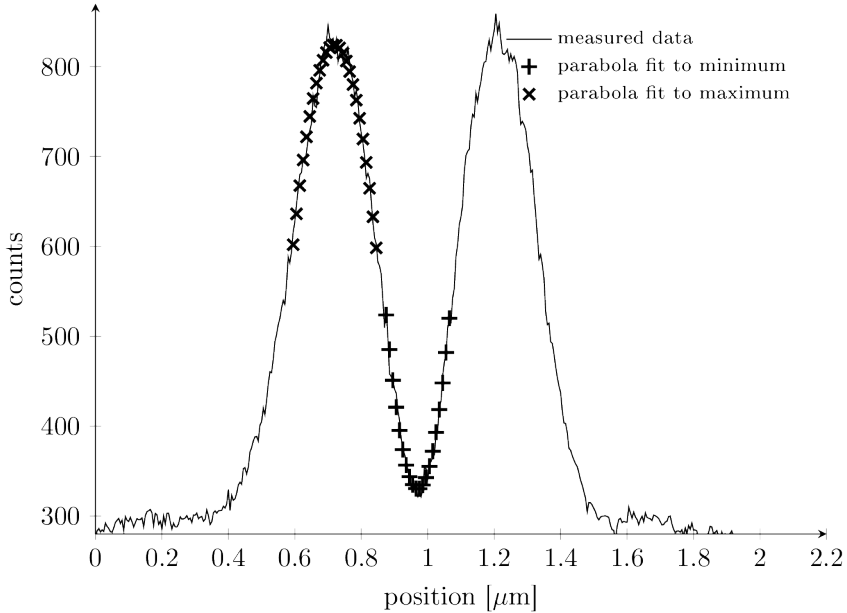


Fig. 3.20 **Donut form factor:** A line profile through the center of a donut depletion pattern (solid line). A maximum and the minimum is fit by a parabola (x and +, respectively), which yields the maximum value, the minimum value, and the form factor.

the depletion pattern minimum, $I_{\text{STED}}(x) = 4 I_{\text{STED}} a^2 x^2$. To measure the intensity distribution in the focus, gold bead reflection can be monitored on a detector with a large active area (see appendix C.1). A line plot through the minimum of in image of a donut acquired in such a way is shown in 3.20. Due to radial symmetry of the donut pattern, it suffices to only consider one dimension. A quadratic fit of the central region of the line plot yielded $S_{\text{det}} = 330 \text{ cts} + 2.13 \cdot 10^4 \frac{\text{cts}}{\mu\text{m}^2} x^2$. The peak intensity corresponds to the peak pixel value, subtracted by the background

$I_{\text{STED}} = 494$ cts. With these numbers, the form factor can be calculated

$$a = \sqrt{\frac{2.13 \cdot 10^4 \frac{\text{cts}}{\mu\text{m}^2}}{4 \cdot 494 \text{ cts}}} = 3.28 \frac{1}{\mu\text{m}} = 3.28 \cdot 10^{-3} \frac{1}{\text{nm}}. \quad (3.14)$$

In order to express the saturation factor as a function of beam power, a relation between maximum intensity in the depletion pattern and beam power needs to be established. As no analytical description of the donut is available, the measured data in Fig. 3.20 is considered. The beam power corresponds to the total number of counts in the donut while the maximum intensity is represented by the maximum value in the line plot divided by the area of a pixel

$$\frac{P_{\text{STED}}}{I_{\text{STED}}} = \frac{1.1 \cdot 10^7}{494 \frac{\text{cts}}{(1/200\mu\text{m})^2}} = 1.3 \cdot 10^{-9} \text{ cm}^2. \quad (3.15)$$

Accordingly, the STED resolution evolves with STED beam power as

$$\text{FWHM}_{\text{STED}} = \frac{\text{FWHM}_c}{\sqrt{1 + \text{FWHM}_c^2 \frac{a^2}{I_s} \frac{P_{\text{STED}}}{1.3 \cdot 10^{-9} \text{ cm}^2}}} \quad (3.16)$$

On the last few pages, values for the three parameters to calculate the resolution function were obtained. To recapitulate, these are $\text{FWHM}_c = 270 \text{ nm}$, $I_s = 0.45 \frac{\text{MW}}{\text{cm}^2}$, and $a_{\text{dir}} = 3.28 \times 10^{-3} \frac{1}{\text{nm}}$. The green curve in Fig. 3.18 shows the result. It does not match the data as well as the fits but nonetheless, the description is in the right ball park. To compare the result quantitatively to the fit result, the parameters need to be combined. The resulting quantity $a^2/P_s = 5.61 \times 10^{-6} \frac{1}{\text{mW nm}^2}$ is 33 % off the fitted result. This may be attributed to an overestimation of the form factor a by 15 %. The donut shape was acquired with a gold bead of 80 nm diameter. Its size may have convolved and broadened the intensity pattern.

To conclude, the data show that the setup is capable of providing images with a resolution down to about 50 nm for both channels, as seen on the right side of Fig. 3.18. A fit free calculation of the resolution scaling function did not yield the desired results, however.

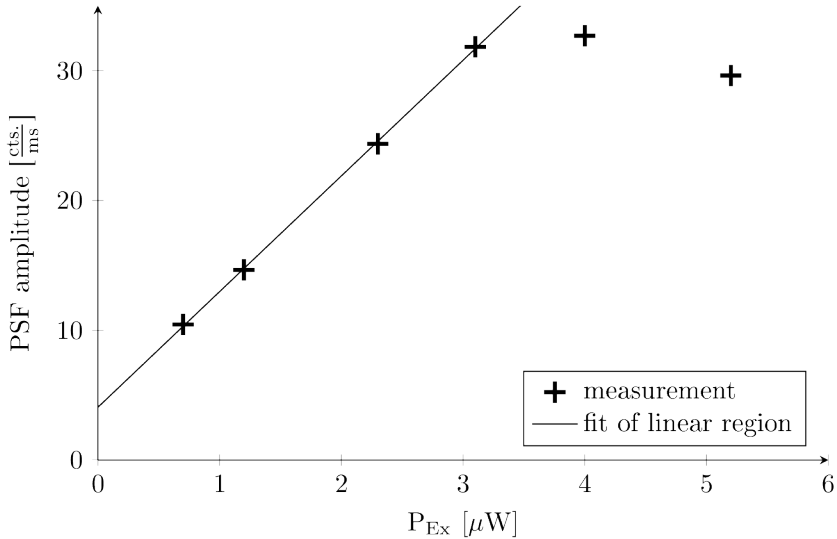


Fig. 3.21 **Detection efficiency:** The amplitudes of Gaussian fits to single molecule images are plotted against the excitation beam power. For low beam powers, the relation is linear, while the slope decreases and even becomes negative for higher powers. The decrease is due to saturation and bleaching. In the linear regime, a fit reveals the offset to be $1.22 \frac{cts.}{ms}$ and the slope $2.67 \frac{cts.}{ms \mu W}$. The pixel exposure time was 0.3 ms.

3.2.6 Detection efficiency

Another important property of a highly sensitive setup is the detection efficiency $\eta_{Det} = k_{Det}/k_{em}$, the quotient of detected to emitted photons. For best quality images, the detection efficiency needs to be as high as possible.

To quantify the detection efficiency, the detection counts of single immobilized fluorophores are acquired with different excitation intensities in confocal imaging mode (see Fig. 3.21). The detected signal rises linearly with the excitation beam power for low beam powers. Between $3 \mu W$ to

4 μW , the excitation gets saturated before premature bleaching reduces the signal again.

The emission rate is not directly accessible. However, it can be calculated *via* a few known parameters. The quantum yield connects it with the excitation rate, accounting for the fact that fluorescence is not the only pathway for an excited dye to go back to its ground state. The excitation rate, in turn, is set by the excitation cross-section σ_{Ex} , the excitation photon flux Φ_{Ex} , and the area A the flux is confined to, by

$$k_{\text{Ex}} = \sigma_{\text{Ex}} \Phi_{\text{Ex}} / A \quad (3.17)$$

The cross-section is not directly available, but for Atto Tec GmbH-fluorophores, the related absorption coefficient, $\varepsilon = N_{\text{A}} \cdot \sigma$, is provided in the data sheets. The area the photons move through is connected to the confocal excitation, and here the FWHM criterion (see eqn. 2.7) is used: $A = \pi (1/2 \cdot 0.51 \lambda_{\text{Ex}} / \text{NA})^2$. The photon flux can be obtained by dividing the beam power by the energy of a photon. Notably, the beam powers are measured in front of the objective while in the calculations the power and flux in the focus are of interest. Hence the transmission coefficient of 80 % of the objective needs to be taken into account. Taking these relations together, the emission rate of the fluorophores is

$$k_{\text{em}} = \eta_{\text{fl}} \frac{\varepsilon}{N_{\text{A}}} \frac{0.8 P_{\text{ex}} c}{\pi \left(0.51 \frac{\lambda_{\text{ex}}}{2\text{NA}}\right)^2 h \lambda_{\text{ex}}}. \quad (3.18)$$

All parameters and constants are available, and with the fitted slope of Fig. 3.21, the detection efficiency amounts to

$$\eta_{\text{det}} = k_{\text{det}} / k_{\text{em}} = 0.9 \%. \quad (3.19)$$

The detection efficiency of other setups is not available for comparison. However, the upper limit can be estimated with the known transmission parameters of the detection pathway of the setup. The objective has a specified transmission $t_{\text{obj}} = 0.8$ in the red spectral region, and is capable of collecting photons from a solid angle $\Omega = 1.3\pi$, which results in a collection efficiency of $\eta_{\text{obj},\Omega} = 0.33$. Dichroics and filters along the detection path

permit 40 % of the emission spectrum to pass. Reflection of lens surfaces accounts for a coefficient $t_{\text{refl}} = 0.96$. The detection fiber coupling efficiency is assumed to be $\eta_{\text{coupl}} = 0.7$ and the fiber output and the unit to focus onto the detector area are estimated to be accountable for $t_{\text{foc,det}} = 0.8$. Finally, the photon detection efficiency of the detector is specified to $\eta_{\text{det}} = 0.7$. With these parameters, the estimated detection efficiency of the setup amounts to

$$\eta_{\text{det,est}} = t_{\text{obj}} \cdot \eta_{\text{obj},\Omega} \cdot t_{\text{spect}} \cdot t_{\text{refl}} \cdot \eta_{\text{coupl}} \cdot t_{\text{foc,det}} \cdot \eta_{\text{det}} = 4.0 \%. \quad (3.20)$$

In these calculations, blinking of fluorophores has not been considered. It reduces the detected signal further, bringing the actual detection efficiency closer to its estimated value.

A sanity check can be performed on the cross-section calculations. The acquired data show saturation at elevated excitation intensities. Saturation arises when the ground state is depleted, that is to say when every pulse of light excites the fluorophore in the focus. The conditions for this case can be calculated from basic constants again.

$$p_{\text{ex}}^{\text{pulse}} = 1 = k_{\text{ex}} \cdot \tau_{\text{pulse}} = \frac{\sigma_{\text{ex}} \Phi_{\text{ex}}}{A f_{\text{rep}}} = \frac{\sigma_{\text{ex}} P_{\text{sat}} \lambda_{\text{ex}}}{A f_{\text{rep}} hc} \quad (3.21)$$

$$\Leftrightarrow P_{\text{sat}} = \frac{A f_{\text{rep}} hc}{\sigma_{\text{ex}} \lambda_{\text{ex}}} = 3.98 \mu\text{W} \quad (3.22)$$

Taking into account the loss in the objective mentioned before, an applied excitation beam power of $I_{\text{ex}}^{\text{sat}} = 4.9 \mu\text{W}$ results. The data in Fig. 3.21 show a saturation between 3 and 4 μW , which fits reasonably well. The reduced value might be due to premature bleaching which has not been taken into account here.

3.2.7 Issues to improve on

Currently, the setup is in a well working state. However, possibilities of improvement are ever present for a complex setup. Here, but a few of these possibilities shall be named.

(i) At the moment, superresolution is provided only laterally. Introducing a depletion pattern which additionally depletes in axial direction would be a big improvement. Cellular imaging, as well as imaging surfaces with fluorescence background in the solution would benefit from this feature. Polarizing beam splitter cubes to couple in a STED beam for z -resolution increase are positioned in the setup already. Therefore, the addition of the axial depletion beam will not require any extraordinary realignment in the setup.

(ii) For a few applications, especially imaging of fixed cells, an additional confocal channel would add value to the setup. At the moment, nuclei need to be stained with YO-PRO-1 which spectrally overlaps with GFP. With an additional channel in the UV range, the standard nuclear stain DAPI could be imaged, opening up possibilities for new multi color imaging. One or two dichroic mirrors would need to be introduced into the setup as it is. For excitation the super-continuum spectrum does not reach far enough into the ultraviolet region. Because the DAPI spectrum (excitation: 350 nm, emission: 460 nm) is away far enough from the other dyes, crosstalk is not an issue. A low cost 350 nm cw laser can be used. For detection, a fourth channel is already available.

(iii) For introducing more STED channels as well as being able to perform FCS measurements and lifetime imaging, TCSPC electronics can open up a wide range of new applications to the setup.

Chapter 4

Investigations

A plethora of research questions has remained elusive due to the limited resolution provided by confocal microscopes. The recent availability of the STED setup described in the previous section enables a more thorough investigation of ongoing projects and opens up a variety of new issues to enquire.

This chapter reports of some of the examinations performed. To that end, the projects are structured in investigative parts concerning DNA and cytoskeletal proteins and to conclude, a technological section follows.

To give an impression of the kind of images the setup acquires in cells, Fig. 4.1 shows triply stained epithelial cells. Actin, microtubules and DNA are labelled and a zoom into the smallest structures of a forming spindle apparatus reveals differently sharp images depending on whether acquisition is performed in confocal or STED mode.

4.1 DNA based approaches to STED microscopy

The multitude of specific functions various proteins can perform largely depend on correct folding. Self assembly of biomacromolecules is therefore crucial to life. It is Nature's solution to minimizing spacial requirements of highly specialized machines.

The folding of proteins is still too poorly understood to be exploited in synthetic imitations. Simpler interactions occur in DNA. These can be

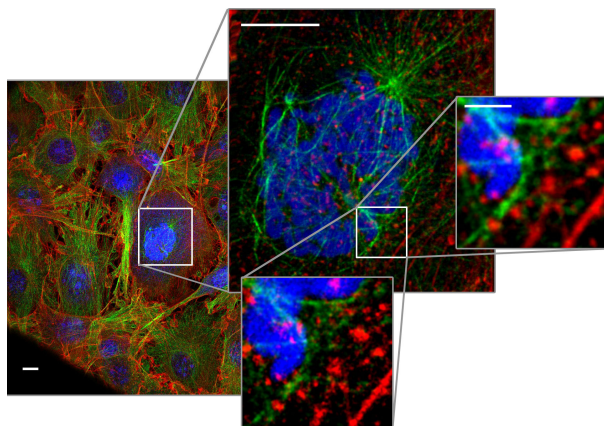


Fig. 4.1 STED imaging of triple labeled fixed cells: Fixed NIH-3 cells on a cover slip in three levels of zoom. The last zoom level is shown in confocal and STED acquisition. blue: YO-PRO-1 nuclear stain; green: secondary immunostaining of microtubules with Aberrior Star 580; red: actin stained with phalloidin-Alexa647. Scale bars: larger images: 10 μm , small images: 2 μm

used to form self assembled structures in two and three dimensions[Castro et al., 2011].

These structures usually have dimensions slightly below the resolution of confocal microscopy. Typical evaluation and characterization procedures rely on electron microscopy. For dynamic systems STED microscopy is a more adequate tool. Furthermore, possible damage introduced by fixation and contrast procedures can be revealed. The next two sections describe projects that combine DNA nanostructures and STED microscopy.

4.1.1 DNA filaments

In the past few years, the field has seen many advances and new structures. However, all designs use the same scaffold to form structures with. Therefore, the total amount of bases and accordingly the size of the structure is

4.1 DNA based approaches to STED microscopy

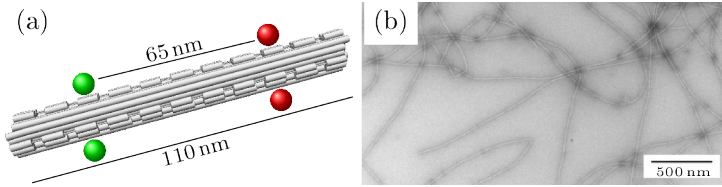


Fig. 4.2 DNA monomer design: (a) Designed structure of a monomer. Six fluorophores are positioned at a longitudinal distance of 65 nm, represented by green (Atto 594) and red (Atto 647N) spheres. Total length 110 nm (b) Control TEM image showing that polymerization takes place.

set. Some ideas to crystallize and concatenate single structures have been realized [Zheng et al., 2009]. Here, an approach is presented to polymerize blocks of DNA origami to polymeric filaments¹. In order to employ these as rails for moving parts in a later development, it is essential that all monomers of these filaments are equally oriented.

Briefly, at the longitudinal ends of the helices shown in Fig. 4.2a, short single stranded DNA strands are exposed to the solution. The single strands on both sides have complimentary sequences and are short enough that only several bound strands in parallel yield a stable connection at room temperature. This ensures that monomers polymerize in a polar fashion and that the resulting structures are stable.

A length of up to 20 μm has been observed for these polymers. To characterize them, monomers were labelled with two different kinds of dyes on each end and investigated with STED microscopy. These two spots of six dyes each are separated by 65 nm along the longitudinal axis (see Fig. 4.2a). As expected, the single building blocks cannot be resolved in confocal microscopy. In STED mode, however, chains of spots appear (see Fig. 4.3). A line profile along one of these chains reveals the alternating position of spots in the two channels (see Fig. 4.4). Indeed, the inter-peak distance matches the 110 nm monomer length quite well and even a shift

¹see PhD project of Evi Stahl, E69, TUM

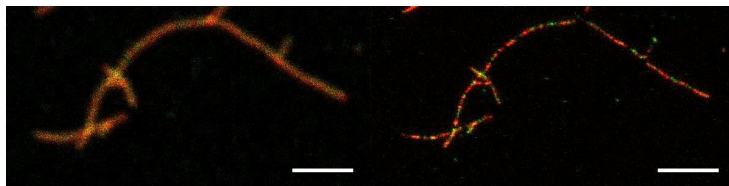


Fig. 4.3 **Polymeric DNA nanostructure:** confocal (left) and STED imaging of two-coloured DNA origami polymers. Only STED reveals the positions of single spots. Scale bars 2 μm

between the two channels of 45 nm in one direction and 65 nm in the other can be observed, as indicated by the coloured bars.

4.1.2 Infinite imaging *via* DNA-PAINT

One drawback of STED microscopy is the fast bleaching of dyes that is due to the high intensities applied. To counteract this, high labelling densities are often used, which can cause artefacts [Lau et al., 2012]. Oxygen scavenging and triplet quenching systems reduce bleaching, but do not circumvent the problem [Kasper et al., 2010].

In this investigation², points accumulation for imaging in nanoscale topography using DNA oligomers (DNA-PAINT) is used with the aim of visualizing structures for very long times without being limited by bleaching. This will be especially useful for samples that show dynamic behaviour. In this proof of principle study, however, only immobilized structures are imaged.

DNA-PAINT was originally developed for localization-based super-resolution microscopy [Jungmann et al., 2010]. Briefly, structures of interest are labelled with single-strand oligonucleotides. Oligos with the complementary sequence and dye molecules covalently bound to them, so-called ‘imager strands’, are added to the imaging buffer. The imager strands

²project in collaboration with Max Scheible, TUM E14

4.1 DNA based approaches to STED microscopy

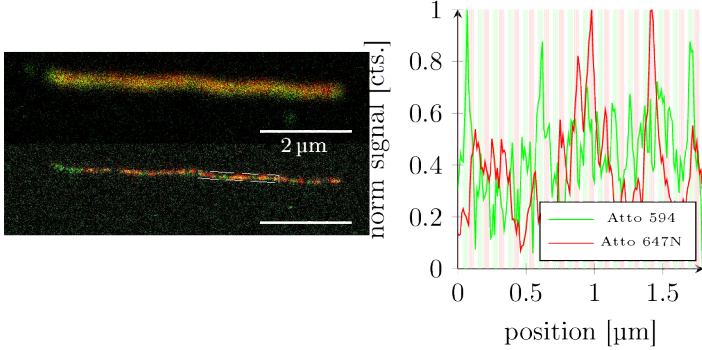


Fig. 4.4 Evaluation of orientation: Left: straight DNA filament. Right: Line profile along the drawn region in the left STED image in both channels. The corresponding peaks alternate with inter peak distances corresponding to the designed values.

show binding kinetics depending on the strand length, ionic strength, and concentration.

For that original application, on- and off-rates are adjusted to values where the airy patterns of bound imagers do not overlap for localization purposes, the on-time of imagers is long enough to get a good signal, and the probability for a single binding event is still as high as possible in order not to unnecessarily prolong the acquisition time. Localization-based super-resolution microscopy is performed by acquiring movies, localizing the center of the airy patterns and mapping the points found on a canvas to form an image.

For the purposes of the project at hand, different blinking kinetics are needed. Rather than stochastically blinking spots, continuously active imaging sites are desirable. Optimally, a dye should be in place until it bleaches and immediately thereafter be replaced by an intact molecule. Of course, the stochasticity of the processes involved does not permit to control every single event. However, the behaviour of the system in general

can be tuned. To that end, the relevant parameters in the system are the on- and off-rates of transient imager strand binding. The on-rate of the imager strands mainly depends on their concentration while the off-rate can be altered by changing the number of complementary bases.

The following paragraphs are dedicated to making a connection between the imager strand properties of on- and off-rates and the image properties signal and contrast. To that end, the characteristics of bleaching, the conditions for a good contrast, and the binding kinetics of imager strands are treated.

4.1.2.1 Bleach rates

The optimum off-rate is determined by bleaching. In the best case, imagers stay bound to the structure of interest as long as they still fluoresce. As soon as they have bleached, they block access for intact imagers and should unbind. The probability of finding a functional dye decays exponentially with exposure time. The time constant of decay is described with a bleach rate. For scanning microscopy, the framewise mode of acquisition needs to be taken into account. It turns out more convenient to describe the cumulative exposure time not in units of seconds but in units of frames. Correspondingly, the bleach rate is described in units of inverse frames. Therefore, waiting times between frames do not need to be considered in this rate. A lower limit to the off-rate is set by the product of bleach rate and frame rate.

Therefore, the dependence of bleaching as a function of applied imaging parameters had to be investigated. These imaging parameters include input beam powers, pixel size, and exposure time. An enquiry into the bleaching characteristics was performed by immobilizing streptavidin-modified dye³ molecules on a biotinylated surface and acquiring movies of an area covered with fluorophores with varying imaging parameters. The mean signal of each frame decays exponentially and reveals the corresponding bleach rate.

Another way of investigating bleaching would be to use fluorescence correlation spectroscopy on a solution of free dyes [Dittrich and Schwille,

³All experiments were performed with Atto 590 for reasons explained in section 4.1.2.3

4.1 DNA based approaches to STED microscopy

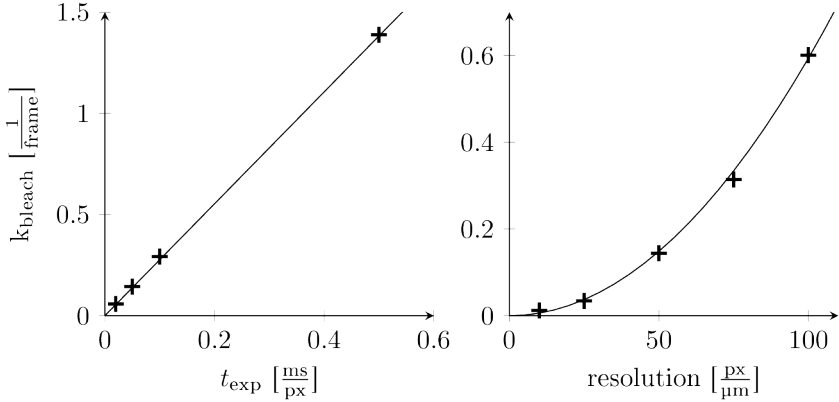


Fig. 4.5 Bleach rate versus exposure time and imaging resolution: The bleach rate depends linearly on the exposure time. The recorded data can be fit well with a slope of $2.8 \frac{1}{\text{frame ms}}$ (left). Furthermore, it depends quadratically on the resolution *via* a quadratic term of $5.9 \times 10^{-5} \frac{\mu\text{m}}{\text{px frame}}$ (right).

2001]. In such an experiment, photophysical blinking could be corrected for in the bleach rate. However, exposure times per pixel may influence the performance of the dyes due to long-lived states on the bleaching pathway. Furthermore, an FCS system with the same repetition rate and pulse length would be needed to exclude different performance due to these characteristics. Thus, the scanning approach was more appropriate for this examination.

First, the dependence of bleaching on scan parameters was investigated. To that end, the exposure time and imaging resolution were changed and the effect was observed. The results are shown in Fig. 4.5. It can be observed that the bleach rate depends linearly on the exposure time and quadratically on the imaging resolution. That implies that the probability for a fluorophore to bleach depends only on the time it is illuminated. Thus,

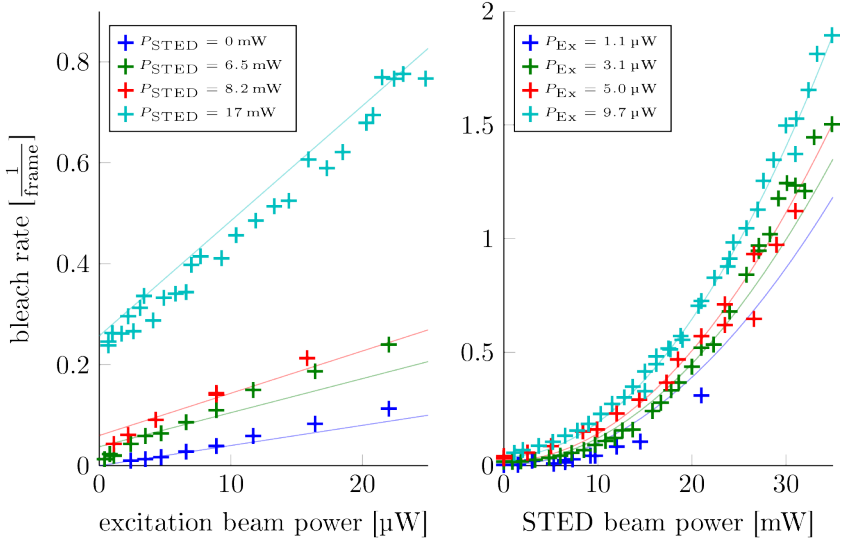


Fig. 4.6 Bleach rate versus beam powers in PAINT buffer: The bleach rate increases linearly with excitation beam power and quadratically with STED beam power. Lines: global fit. Fit parameters: $a_1 = 6.5 \times 10^{-5} \frac{1}{\text{frame } \mu\text{W mW}^2}$, $a_2 = 8.9 \times 10^{-4} \frac{1}{\text{frame mW}^2}$, $b_1 = 4.0 \times 10^{-3} \frac{1}{\text{frame } \mu\text{W}}$, $b_2 = 7.9 \times 10^{-7} \frac{1}{\text{frame}}$

the lifetimes of dark states that lie on the bleaching pathway are⁴ outside the interval between exposure time and frame acquisition time. Otherwise, a more complex dependence would apply.

Next, the influence of excitation and STED beam powers was investigated. Their effect to bleaching is plotted in Fig. 4.6. Interestingly, the two beam powers do not simply contribute to the bleach rate as independent factors. They show a more complex interrelation. An evaluation by eye hints to a linear behaviour with respect to excitation beam power, and the dependence on STED beam power looks quadratic. When fitting the

⁴see section 2.2

4.1 DNA based approaches to STED microscopy

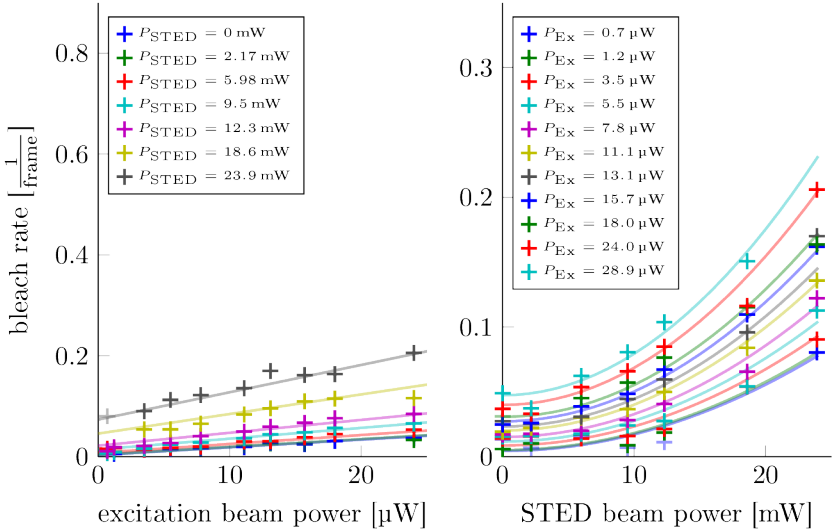


Fig. 4.7 **Bleach rate versus beam powers in ROXS PAINT buffer:** A ROXS environment decreases the bleach rate but maintains the linear dependence on excitation beam power. Lines: global fit. Fit parameters: $a_1 = 6.8 \times 10^{-6} \frac{1}{\text{frame } \mu\text{W mW}^2}$, $a_2 = 1.2 \times 10^{-4} \frac{1}{\text{frame mW}^2}$, $b_1 = 1.5 \times 10^{-3} \frac{1}{\text{frame } \mu\text{W}}$, $b_2 = 3.3 \times 10^{-3} \frac{1}{\text{frame}}$

latter with a parabola shifted in y for various excitation beam powers, it becomes plain that the quadratic term as well as the offset have a linear dependence on the excitation beam power. Hence, the data can be modelled by a function of the form

$$k_{\text{bleach}} = a_1 P_{Ex} P_{STED}^2 + a_2 P_{STED}^2 + b_1 P_{Ex} + b_2. \quad (4.1)$$

This relation only holds true for the imaging parameters employed during these experiments. A more general function will be formulated later in this chapter. A global fit to bleach rates for various excitation and STED beam powers is shown as lines in Fig. 4.6 and describes the data quite well.

To apply this model to a system with different bleaching characteristics and to determine whether the same functional form is valid, the same evaluation was performed on samples with a ROXS buffer. The ROXS concept (see section 2.2) was designed to control the lifetimes of fluorophore states that are on the bleaching pathway. Thus, bleach rates are expected to differ in a ROXS environment from those in a simple buffer. The data and fits are shown in Fig. 4.7 and it is plain to see that the functional form remains the same, but with different pre-factors. These fit parameters nicely emphasize that the chosen ROXS environment decreases the probability for a fluorophore to bleach by a factor of five to ten. Only the offset b_2 has a higher value. Its physical interpretation is unclear, however, and it might be just a consequence of a measuring artefact.

With these results, the bleach rate per frame can be calculated for every set of scan parameters *via*

$$k_{\text{bleach}} = (a_1 P_{Ex} P_{STED}^2 + a_2 P_{STED}^2 + b_1 P_{Ex} + b_2) t_{\text{exp}} \Delta x^2 0.08 \frac{\mu\text{m}^2}{\text{ms px}^2}. \quad (4.2)$$

Here, a different exposure times t_{exp} and imaging resolution Δx to those employed for the investigation of beam power dependence are corrected for by the last term. It is the quotient of the altered parameters and those used for the last investigation in the functional form elucidated in Fig. 4.5.

4.1.2.2 Background and contrast

The on-rate should be as high as possible in order to quickly repopulate vacant positions. High dye concentrations give rise to high background fluorescence, and correspondingly to bad contrast. This balance leads to an optimum dye concentration at which the contrast is just good enough. To quantify this relation, Fig. 4.8 shows background pixel values (closed symbols) and PSF peak values of immobilized single dye molecules (open symbols) of confocal (squares) and STED (circles) measurements with an excitation beam power of $3 \mu\text{W}$. Unsurprisingly, the background level rises linearly with imager concentration. A fit reveals that it is three times lower. The background is lower in STED images with respect to confocal images

4.1 DNA based approaches to STED microscopy

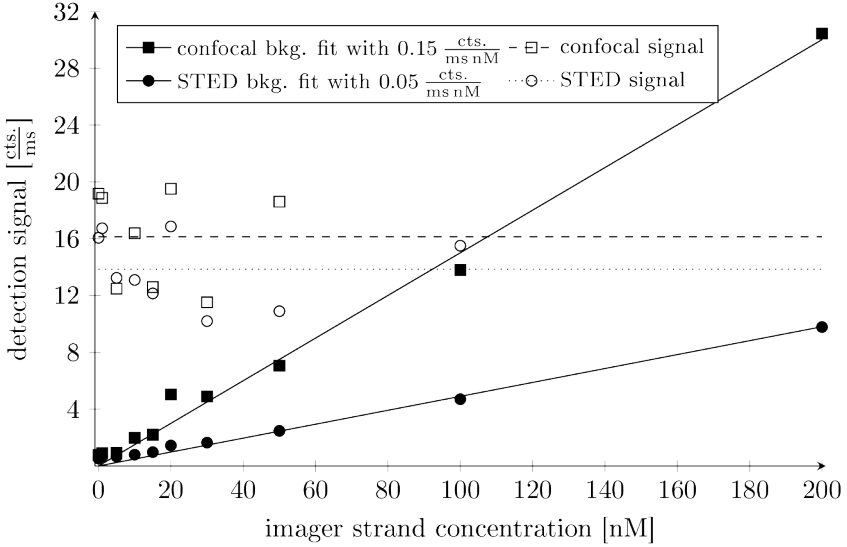


Fig. 4.8 Signal and background for single molecules: Imaging surface-bound single fluorophores shows a constant signal (indicated by the dashed line), but a background (bkg.) rising linearly with the concentration of imager strands in solution.

because much of the confocal volume does not contribute to detection. Due to the low number of PSF peaks found that were suitable for fitting, the variance in the statistics high. Nonetheless, the data does not contradict the reasonable assumption that the signal level is a constant with respect to the surrounding imager concentration. A rough estimate of the mean signal value of $16 \frac{\text{cts.}}{\text{ms}}$ for one single fluorophore with can be extracted for confocal imaging. In STED mode, the mean signal value amounts to about $14 \frac{\text{cts.}}{\text{ms}}$.

For noiseless images, threshold to perceiving structures is set by a Weber contrast of 1% to 2% as mentioned in section 2.1.3. However, due to the

Chapter 4 Investigations

small number of counts, PAINT-STED images tend to incorporate some noise. Therefore, a Weber contrast of 10% is set for the threshold. That sets the upper limit to the concentration of imager dyes.

$$\frac{S_{\text{PSF}} - S_{\text{back}}}{S_{\text{back}}} \geq 10\% \quad (4.3)$$

$$\frac{16 \frac{\text{cts.}}{\text{ms}}}{0.15 \frac{\text{cts.}}{\text{ms nM}} \cdot c} \geq 1.1 \quad (4.4)$$

$$c \leq 106 \text{ nM} \quad (4.5)$$

Here, the fit parameter for confocal acquisition was employed. For STED imaging, the corresponding critical concentration thus becomes $c_{\text{crit,STED}} = 285 \text{ nM}$. For transiently binding fluorophores, however, the mean signal decreases by the fraction of time they are bound while the background stays the same. Therefore, the signal to background ratio⁵ decreases by the same fraction, and the critical concentrations diminish just the same. These transient critical concentrations are then

$$c_c^{\text{trans}} = c_c^{\text{fix}} \frac{\tau_b}{\tau_b + \tau_d}, \quad (4.6)$$

with the time imagers are dissociated τ_d and the time imagers are bound τ_b . The time imagers are dissociated depends on the imager concentration, $1/\tau_d = k_{\text{on}} c^{\text{trans}}$. The time imagers are bound, in contrast, is the inverse of the imager off-rate, $1/\tau_b = k_{\text{off}}$. Furthermore, providing N docking sites per imaging spot increases the signal by N and thus raises the critical concentration. With these relations, the critical concentration for transiently bound fluorophores gets

$$c_c^{\text{trans}} = N c_c^{\text{fix}} - N \frac{k_{\text{off}}}{k_{\text{on}}} \quad (4.7)$$

The on-rate depends on the affinity of the imager to the target and has been determined to be $k_{\text{on}} = 2.3 \times 10^6 \frac{1}{\text{M s}}$ for the system at hand [Jungmann et al., 2010]. The off-rate is discussed in the next paragraph.

⁵equals the Weber contrast plus one.

4.1.2.3 Imager surface interaction

The time imager strands are bound is determined by the off-rate. It does not depend on the concentration and it exponentially varies with the strand length. Values have been determined for several imager strand lengths: $k_{\text{off}}^{9\text{bp}} = 1.6 \frac{1}{\text{s}}$, $k_{\text{off}}^{10\text{bp}} = 0.11 \frac{1}{\text{s}}$, $k_{\text{off}}^{11\text{bp}} = 6 \times 10^{-3} \frac{1}{\text{s}}$ [Jungmann et al., 2010]⁶. Ionic strength influences the off-time as well. This dependence was not investigated in the current project, however. All experiments were performed at the same buffer conditions.

For reasons of spectral ranges of the fluorophores, a different dye had to be employed than in the original system used for a localization-based approach to subdiffraction microscopy. Atto 594 was chosen to replace Atto 655 because its properties are most similar to the original dye. Still, it was necessary to assess whether undesired interactions of the dye with the surface might influence the measurements.

To that end, blinking dynamics were recorded. A comparison to the off-rates from literature then reveals the performance of the dye.

Movies of a surface with immobilized target structures were acquired in the presence of 5 nM 10 bp imager strands. While the imagers are bound, their fluorescence can be detected, whereas the spot remains dark when no intact imager is present. The duration of a binding event is simply set by the time a spot is continually bright in the acquired movie. For a good timing resolution, the frame rate needs to be chosen high and was set to 1.2s. Faster dynamics were probed, but no events were found.

All frames of a movie are summed up and the resulting image shows spots where imagers tend to bind. A region of interest is defined around these spots and the mean fluorescence within them is traced through the frames of the original movie. The file format employed (see section E.2.2) specifies time steps for every frame. In this way, time traces as shown in Fig. 4.9 can be generated and evaluated. Due to photophysical blinking of a fluorophore, the start and end points of an event are often not well defined. This fact leaves space for judgement by the experimenter to decide whether

⁶these values have been determined for a PBS buffer. Very similar rates are observed for the magnesium buffer employed in the PAINT experiments (Max Scheible, priv. comm.)

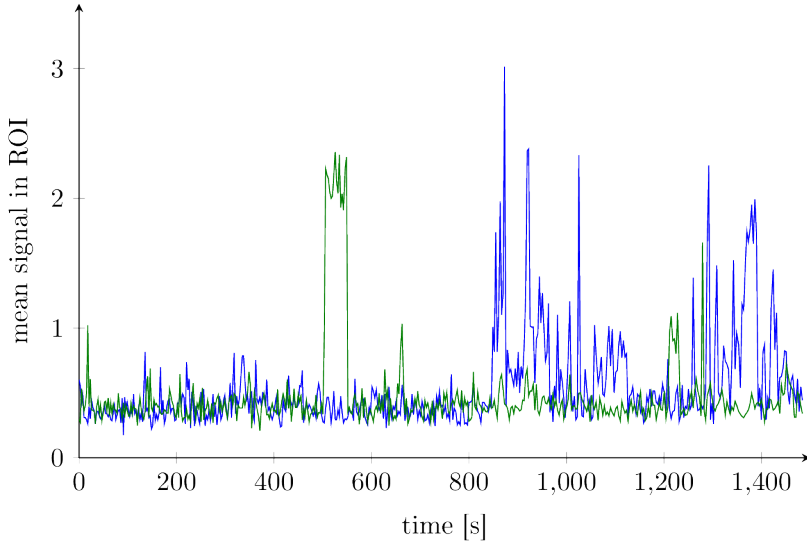


Fig. 4.9 Transient binding of imager strands: Mean signal of a ROI area over time. Very well defined binding events as well as traces impaired by blinking can be present.

multiple binding events or one binding event with a blinking fluorophore is at hand. Another issue of subjectivity is that background fluorescence can cause a high value for a few frames, thus suggesting a binding event where there is none.

Fig. 4.10 shows histograms of several of these binding times under different conditions. Strikingly, the binding times are much longer than expected from literature. That suggests that the system suffers from unspecific binding to the surface of the newly introduced fluorophore. This observation has been confirmed by TIRF experiments on the same system⁷.

The histogram furthermore shows that the distribution of events is shifted to longer on-times under ROXS conditions than in a traditional

⁷Max Scheible, priv. comm.

4.1 DNA based approaches to STED microscopy

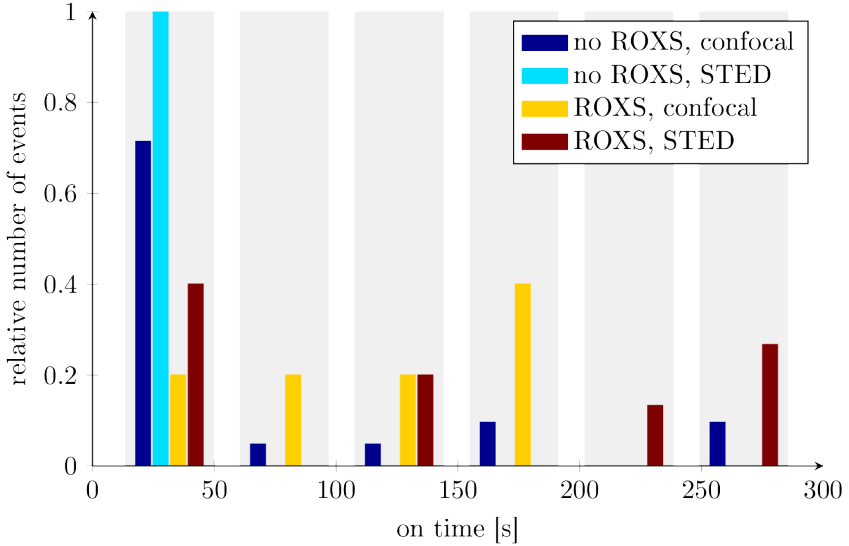


Fig. 4.10 **Histogram of imager on-times:** Under ROXS conditions, observed blinking times are longer than under traditional PAINT buffer conditions.

PAINT buffer. This, in turn, means that the bleach times in the two environments differ and lie in the range of on-times observed. And indeed, the imaging parameters applied⁸ lead to bleach times of $\tau_{\text{bleach}}^{\text{trad}} = 34\text{ s}$ and $\tau_{\text{bleach}}^{\text{ROXS}} = 124\text{ s}$ with the application of eqn. 4.2, which is well in the observed range.

4.1.2.4 Synopsis

In order to optimize the system, the individual results of the last paragraphs need to be combined. To recapitulate, the off-rate needs to be

⁸excitation beam power: $2\ \mu\text{W}$, STED beam power: $5\ \text{mW}$, imaging resolution: $50\ \frac{\text{px}}{\mu\text{m}}$, exposure time: $0.1\ \frac{\text{ms}}{\text{px}}$, frame rate: $0.44\ \frac{\text{frame}}{\text{s}}$

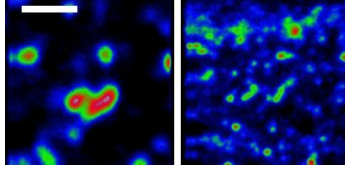


Fig. 4.11 **PAINT result**: Confocal (left) and STED (right) PAINT image of the same region Scalebar 1 μm .

higher or equal to the bleach rate in order to maximally exploit the fluorophores as well as the binding sites. Taking into consideration the finite on-rate, this lower limit needs to be aimed at in order to introduce as little vacancy time as possible.

$$k_{\text{off}} = k_{\text{bleach,t}} \quad (4.8)$$

$$= k_{\text{frame}} \cdot k_{\text{bleach,f}} \quad (4.9)$$

Here, $k_{\text{bleach,t}}$ describes bleaching per unit of time, while $k_{\text{bleach,f}}$ describes bleaching per acquisition frame.

This relation for the off-rate can be combined with the restrictions for the imager strand concentration applied (eqn. 4.7) to form a general equation showing the interdependence of imaging parameters and concentration

$$\left(c_c^{\text{fix}} - \frac{c^{\text{trans}}}{N} \right) k_{\text{on}} = k_{\text{frame}} k_{\text{bleach}} = k_{\text{off}}^{\text{strand}}. \quad (4.10)$$

Both of these equalities need to be respected for an optimal system, and additionally, eqn. 4.2 holds true. That sets an optimal combination of imager strand concentration, exposure time, frame rate, STED and excitation beam power, the number of docking sites, and imager strand length. Therefore, there are four free parameters to chose, enabling the experimenter to set the parameters of his or her highest priority freely.

Even though the system suffers from many unspecific surface interactions, a PAINT-STED experiment was performed and its result is shown

4.1 DNA based approaches to STED microscopy

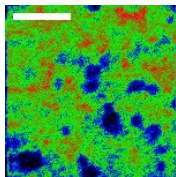


Fig. 4.12 **PAINT result:** PAINT-STED image of the same region as in Fig. 4.12 after very long exposure. Scalebar 1 μm .

in Fig. 4.12. An improvement of STED with respect to confocal can be seen. The structures investigated are rods incorporating four imaging spots with 12 docking sites each, separated equidistantly by 100 nm⁹. Unfortunately, these structures cannot be resolved due to the unspecific binding of the imager dye. However, two elongated shapes with approximately the length of the designed structures can be seen in the STED image. They may correspond to two bound structures. The ongoing transition to a differently passivated surface will probably reduce unspecific binding and increase the quality of PAINT-STED images.

4.1.2.5 Outlook

Interestingly, acquiring long PAINT-STED movies causes a increase in background signal, obstructing the detection of any transient imager binding (see Fig. 4.12). This increase is persistent over more than an hour. This effect has not been understood and a thorough investigation is essential to successful progress of the project.

Furthermore, this study only accounts for one-channel measurements. For an evolution to multi-channel DNA-PAINT, the influence of cross-excitation on bleaching will have to be taken into account[Eggeling et al., 2006].

⁹concentration of imager strands: $c = 5 \text{ nM}$, concentration of structures for immobilization: 50 pM to 100 pM. Imaging parameters were the same as for the measurement of imager on-times

4.2 STED microscopy and cytoskeletal proteins

4.2.1 Legionella

In 2011, the drinking water ordinance has been altered in Germany TrinkwV. As a consequence, the drinking water installations in apartment buildings need to be inspected at least once a year. One of the reasons for this amendment was Legionnaires' disease or Legionellosis. This disease has been first described in 1976 in Philadelphia, Pennsylvania where several hundred of a legionnaires' convention acquired the sickness and a few tens died from it[Time Magazine, 1976]. To date, about 8.000 to 18.000 cases per year are estimated to occur in the United States[Hampton et al., 2011] and nearly five thousand in the European Union[ECDC, 2013].

The disease involves fever, chills and a serious cough, and various side effects may arise. Its cause are gram negative aerobic bacteria of the genus *Legionella*. The most widely spread and lethal species is *Legionella pneumophila*. These bacteria live in aqueous reservoirs, preferably at temperatures between 20 and 45 °C in symbiosis with amoeba[Swanson and Hammer, 2000].

When inhaled, the bacteria infect macrophages and lung epithelial cells[K. and Swanson, 2008]. They make use of the host intracellular machinery to replicate. When a bacterium invades the host cell, a *Legionella* containing vacuole (LCV) is formed around it to ward off bactericidal lysosomes. About 300 effector proteins are released from the bacterium into the host cell to manipulate the host's cellular processes.

In a recent study, the described STED setup was involved in discovering the function of one of these effector proteins[Rothmeier et al., 2013, in press]. More specifically, the protein *Legionella* eukaryotic gene G1 (LegG1) and its effects to macrophage host cells were investigated. The results suggest that, when translocated to the host cytoplasm, this protein invokes a signal cascade causing microtubule polymerization for LCV trafficking. This probably promotes the intracellular survival and replication of *Le-*

4.2 STED microscopy and cytoskeletal proteins

gionella. When the host cell has served its function for the bacteria, it is destroyed.

Microtubule polymerization is thought to be induced *via* activation of the small GTPase Ran, a very important regulatory protein involved in spindle assembly, cytokinesis, and nucleo-cytoplasmic transport [Clarke and Zhang, 2008; Yudin and Fainzilber, 2009]. In the study, evidence has been found that LegG1 activates Ran and thereby influences the microtubule network. Several mutations of *Legionella* were investigated. Here, the results concerning measurements on the STED microscope are presented. Fig. 4.13(a-d) compares the phenotypes of the genotypes investigated.

The mutated strain of *Legionella pneumophila* $\Delta icmt$ is a non-pathogenic variant, and accordingly its host cells have a microtubule network resembling that of uninfected macrophages (compare Fig. 4.13a and e).

When the bacteria lack the gene for LegG1, Ran is not activated, and therefore the host microtubule network is less stable than when hosting a wild type *Legionella*. Thus, the microtubule network looks less stably polymerized than in the wild type (compare Fig. 4.13b and c).

The strain $\Delta legG1/M45-legG1$ introduces an overexpression of *legG1*. Thus the microtubule network of the host cell is stabilized more than in the wild type case (see Fig. 4.13d)

As standards for comparison, Fig. 4.13 shows images of control samples in panels (e-g). For a reference of how a normal microtubule network of a macrophage looks, untreated cells were imaged. All samples show networks between two extreme cases: a completely depolymerized microtubule network, and an extremely stabilized one. Thus, these two serve as a control to classify the samples within the spectrum of possible stages. Nocodazole induces depolymerization of the network, hence this is one extreme case, while the other extreme is caused by taxol.

4.2.2 α -synuclein

Parkinson's disease is a movement disorder which causes trembling extremities, stiff movement and poor balance. Patients are typically above 60 years old. In most cases, a genetic cause is not assumed. The disease is associated with a lack of dopamine in nerve cells in the brain.

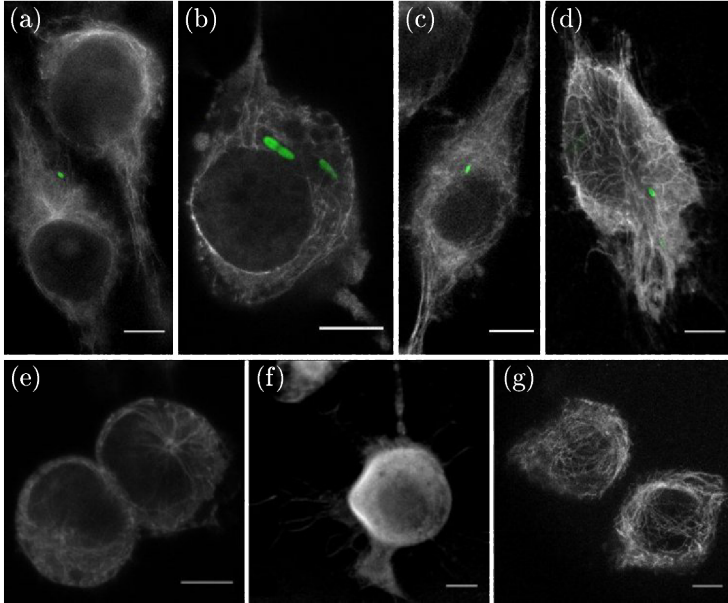


Fig. 4.13 *Legionella* in macrophages: Samples (a-d): $\Delta icmt$, $\Delta legG1$, wild type, $\Delta legG1/M45-legG1$. Controls (e-g): uninfected macrophages, treated with nocardazole, treated with taxol. Microtubuli are shown in grey, *Legionella* in green. Scale bars 5 μm .

At the moment, no cure of Parkinson's disease is known. Patients are treated to relieve them from the symptoms, however. Most commonly, a combination of levidopa and carbidopa are given. Levidopa convert to dopamine while carbidopa delay this conversion until the substances have reached the brain.

α -synuclein is a protein expressed in neural tissue whose function is not completely clear yet. It has been shown to interact with microtubule [Alim, 2001] and actin [Sousa et al., 2009], so it might be active as a microtubule-associated protein. Furthermore, it might play a role as a

4.2 STED microscopy and cytoskeletal proteins

chaperone [Bonini and Giasson, 2005; Chandra et al., 2005]. Additionally, interaction with lipid membranes has been shown [Uversky, 2007]. Lastly, a regulatory function of dopamine transporters by α -synuclein has been suggested [Wersinger and Sidhu, 2003; Lee et al., 2001].

In the brain tissue of patients who had suffered from Parkinson's disease, aggregates of α -synuclein can be found. These have a fibrillar form and are called Lewy bodies. Lewy bodies also play a role in other pathological neuronal diseases. All of them are summed up under the term synucleinopathies. Neither the cause for aggregation nor its pathway are fully understood yet.

In this approach to the subject¹⁰, interactions between α -synuclein and the cytoskeleton are investigated. Additionally, aggregation of α -synuclein inside cells is examined. Besides *in vitro* binding and morphological studies, the effects *in vivo* are of interest. In that field, morphology, mechanics and diffusion are investigated. For morphological studies, STED microscopy is the tool of choice, being capable of resolving structures of interest.

For *in vivo* studies, genetically modified SH-SY5Y cells were employed. The expression of GFP-tagged α -synuclein was introduced into these neuronal cells. α -synuclein aggregation was induced in three different ways: (i) cells were cultured in a medium containing a high concentration of monomeric α -synuclein, (ii) seeds of aggregated α -synuclein were placed on the substrate, and (iii) cells were treated with rotenone, a pesticide known to cause Parkinson's disease.

The following paragraphs subsume the classes of aggregates cells develop when treated with these methods.

Fig. 4.14 depicts a comparison between confocal and STED imaging with the samples investigated. Three labels have been probed. α -synuclein was tagged with GFP (blue where present, but mostly the channel has been left out). As a secondary and STED compatible stain for α -synuclein, an Atto 594-modified antibody against α -synuclein was applied to the fixed cells. Lastly and to characterize the actin networks, phalloidin-Alexa 647 was

¹⁰PhD project of Christian Raiss, Nanobiophysics group, University of Twente, Netherlands

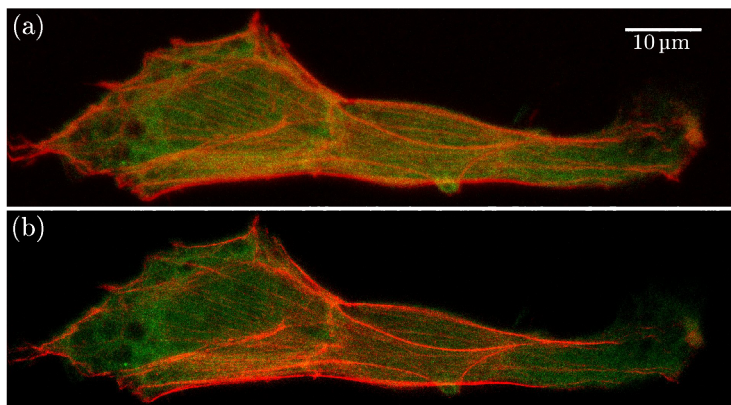


Fig. 4.14 Differentiated SH-SY5Y cell expressing GFP-tagged α -synuclein - comparison of acquisition modes: Confocal (a) and STED (b) image of the same cell. The actin channel (red) benefits from the increased resolution more than the α -synuclein-antibody channel (green) due to the different degree of confinement of the dyes.

employed. Later in this section when not stated otherwise, zoomed regions into parts of a cell were acquired with STED resolution. A comparison to confocal images is left out in most cases.

monomers When α -synuclein aggregation is induced via a high concentration of α -synuclein monomers in the medium the cells are embedded in, the aggregates form in a densely packed morphology termed Lewy-body like inclusion (LIBLI). An example is shown in Fig. 4.15.

LIBLIs (see Fig. 4.15b) show a very bright fluorescence that makes finding them very easy in epifluorescence microscopy.

An investigation of the surface of a nucleus (see Fig. 4.15c) shows α -synuclein sticking on the surface in a fibrillar manner.

Also in the cytoplasm, α -synuclein structured can be found (see outer regions in Fig. 4.15d). These are not aggregations in the manner of a LIBLI. They form a network with a fine mesh size which resembles that of a keratin

4.2 STED microscopy and cytoskeletal proteins

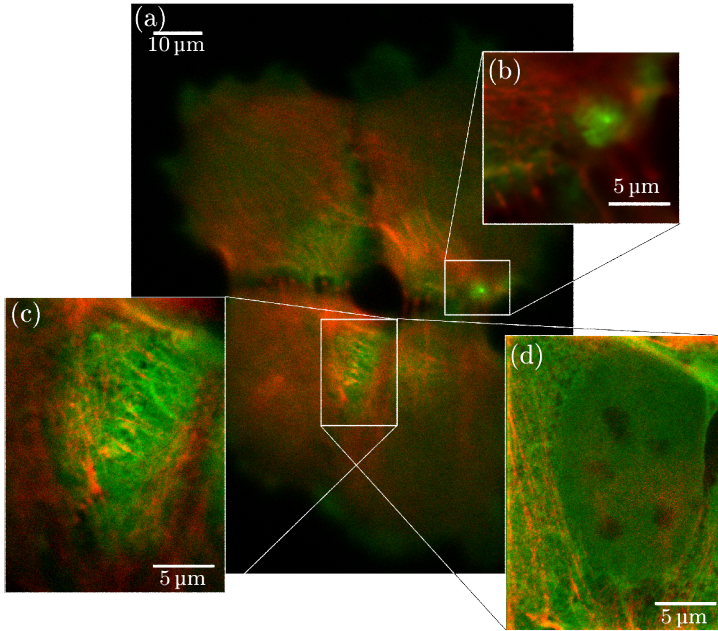


Fig. 4.15 Cells in medium containing α -synuclein monomers: (a) Four cells showing two aggregate morphologies. Red: actin stained via phalloidin, green: α -synuclein stained via antibody. (b) α -synuclein aggregate with a dense core. (c) Nuclear Membrane, surrounded by actin and antibody-stained α -synuclein. α -synuclein positive tangles appear on the nuclear membrane. (d) A cut through the nucleus at a lower z position shows a quite homogeneous distribution of α -synuclein inside the nucleus. No aggregates were found intranuclearly.

network in epithelial cells. Therefore, an investigation of its colocalization with intermediate filaments would be a promising future step.

α -synuclein-distribution within the nuclei (see Fig. 4.15d) is rather homogeneous, with the exception of the nucleoli. Interestingly, the relative fluorescence signal of GFP and antibody channels is higher in inner part of the nuclei than outside (not shown). This suggests that the nuclear membrane represents a barrier to the antibodies during the process of staining.

Some cells like the one depicted in Fig. 4.16 incorporate big vesicles that are void of α -synuclein, which are not present in control cells, however (not shown). Their nature has not been elucidated and they are subject of ongoing investigations. One hypothesis is that they might be autophagosomes.

seeds When the aggregation is induced by α -synuclein-aggregate seeds, LIBLIs can be found as well. Fig. 4.17 shows a cell with such an aggregate. Interestingly, GFP and antibody signals differ quite significantly here. Only a very small spot shows a high GFP fluorescence while the antibody signal is spread over a larger region. This is the case although the GFP channel was acquired with confocal resolution, while the antibody channel was

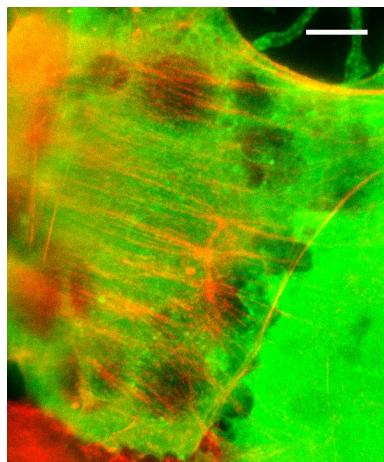


Fig. 4.16 Void vesicles in monomer-induced samples: In a few cells a vast part of the cytoplasm is taken up of vesicles devoid of α -synuclein. Scale bar 5 μ m.

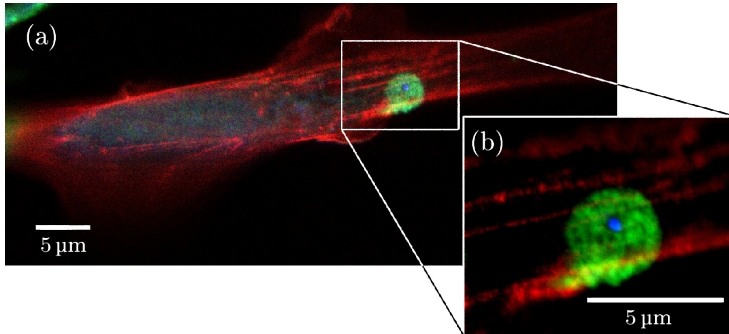


Fig. 4.17 **Seed-treated cells:** Cell with a two-phase aggregate. Blue: GFP-tagged α -synuclein, green: α -synuclein antibody, red: phalloidin-actin.

recorded in STED resolution. It is worth to note that the comparison between channels can hardly ever be performed in a quantitative manner. Too many parameters like cross-sections and quantum yields come into play here. Due to this fact, the brightness and contrast values for each channel can be chosen quite arbitrarily. Hence, it might well be possible that the larger region which is bright in the antibody channel does show fluorescence in GFP, but to a very much lower level than in the small spot. That can be explained by an extremely high density of that spot, not permitting antibodies to diffuse and bind there. As a side remark, these spots can be found very easily on a bright field fluorescence microscope also when they are not well in focus. Also this fact hints to an extremely high density of active GFP.

Apart from this and a few similar cases, GFP and antibody signals generally show very similar structures. Only due to the different imaging modes, the image from antibody fluorescence is confined to a smaller region and looks less fuzzy. That suggests that the antibody is specific to α -synuclein and differences in signal do not hint to artefacts.

In a few cells grown on seeds, colocalization between actin and α -synuclein can be found as shown in Fig. 4.18.

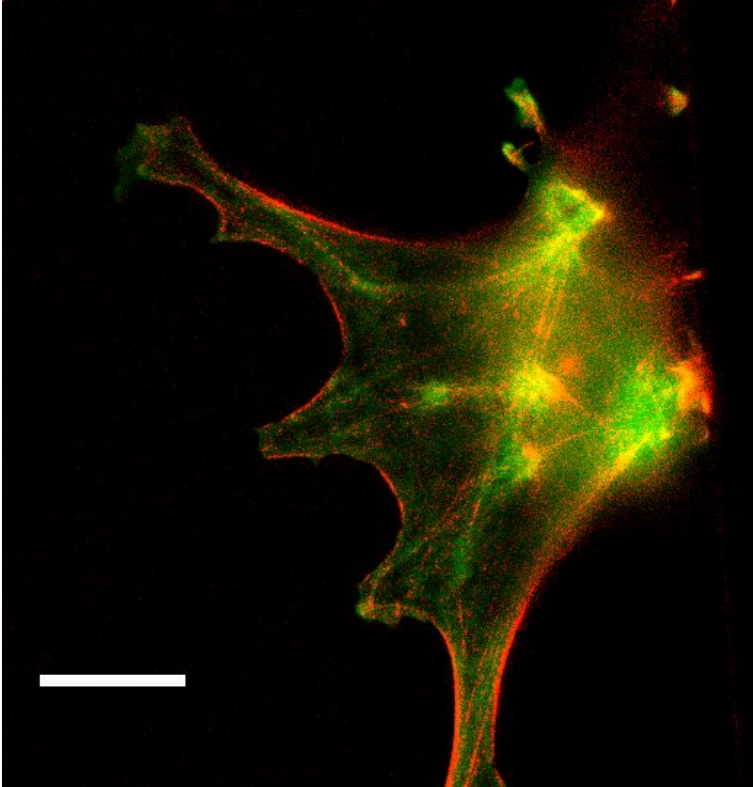


Fig. 4.18 Seed-induced samples: Colocalization between actin and α -synuclein. Scale bar 10 μ m.

4.2 STED microscopy and cytoskeletal proteins

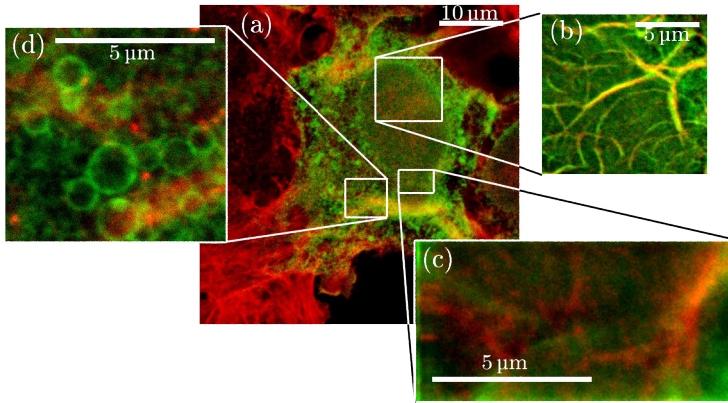


Fig. 4.19 Differentiated SHSY-5Y cells overexpressing GFP tagged α -synuclein exposed to rotenone: (a)&(c) α -synuclein accumulation on the nuclear membrane. (b) Colocalization of α -synuclein and actin on the nuclear envelope (different z). (d) cytoplasmatic vesicles with accumulated α -synuclein inhomogeneously distributed on the membrane.

rotenone SH-SY5Y cells treated with rotenone incorporate a vast quantity of vesicles in their cytoplasm. These vesicles do not seem to have any interaction with actin, but they are covered with α -synuclein (see Fig. 4.19d). Additionally, the nuclear membrane shows α -synuclein signal (see Fig. 4.19c).

One more striking feature of these samples is that a strong colocalization between actin and α -synuclein can be seen often, as depicted in Fig. 4.19b.

All three methods induces LIBLIs. These can have various shapes and sizes, from round and dense over round and porous to fibrillar. α -synuclein tends to associate with membranes. Mostly when treated with rotenone, but also with the other methods, cells develop cytoplasmatic vesicles.

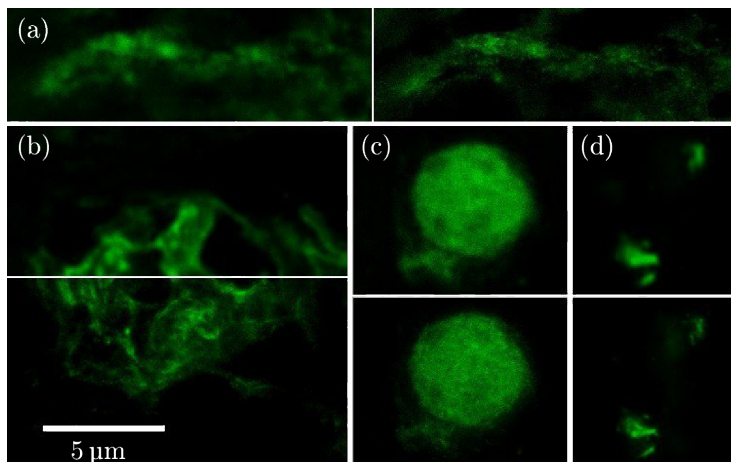


Fig. 4.20 **Human Lewy bodies:** (a) through (d) show comparisons of confocal and STED images of the same region. Representative examples of distinguishable forms of Lewy bodies were selected. α -synuclein is stained with antibodies. Scale bar applies to all images.

Lewy bodies To establish the quality of these model systems, they are compared to a pathological sample of cells with Lewy bodies (Fig. 4.20).

In this sample, α -synuclein aggregates mostly have a fibrillar form. These fibrils form fuzzy networks of various mesh sizes, often below confocal resolution (Fig. 4.20a-c). The networks are not homogenous, however, but feature more and less dense regions. A few aggregates have a very dense structure (Fig. 4.20d) and vesicles cannot be found at all. Also round and porously looking aggregates can be observed. A whole-tissue actin stain was unsuccessful, so the interdependence of the two structures could not be investigated.

The structures observed in the model systems and in the pathological sample resemble each other. For a more quantitative evaluation, more data is needed. The images presented here do encourage the continuation of the investigation of LIBLIs using STED microscopy, however.

4.2.3 Keratin

Living cells exhibit an enormous bandwidth of mechanical and morphological properties that are mainly determined by the cytoskeleton. In metazoan cells this composite network is constituted of three different types of filamentous systems: actin filaments, microtubules and intermediate filaments. Keratin-type intermediate filaments are an essential component of epithelial tissues, where they comprise networks of filaments and filament bundles. However, the underlying mechanisms leading to this inherently polymorphic structure remain elusive. In a recent study[Kayser et al., 2012], the structure was characterized at various length scales using the STED setup described here. It was shown that keratin filaments form kinetically trapped networks of bundles under near-physiological conditions *in vitro*. The network structure is determined by the intricate interplay between filament elongation and their lateral association to bundles and clusters.

The network was characterized by the mesh size ξ describing the exponential distribution of inter-structure-distances and the apparent width d of structures. These two measures do not depend on the pathway the network is formed if it is in equilibrium. If the network is kinetically trapped, however, the network structure can be tuned by the assembly path. For the keratin network investigated, it turned out that ξ decreases when the network is formed at low pH, high temperature, or high ionic strength. This not only confirms that a nonequilibrium network is on hand, but it also hints to the different interactions and corresponding energies for filament elongation and bundle ripening.

STED imaging facilitated the expansion of the accessible range of ξ and d , thereby providing for a wider variety of pathway parameters. The high structural insight can be observed in Fig. 4.21. Confocal and STED acquisition of the same area yield strikingly different results. An even finer structure is revealed by deconvolution¹¹. As this might introduce artefacts, however, only raw data STED images were used for the study.

The results show how complex properties even relatively simple systems

¹¹ *via* the Richardson-Lucy-Algorithm implemented in MATLAB®

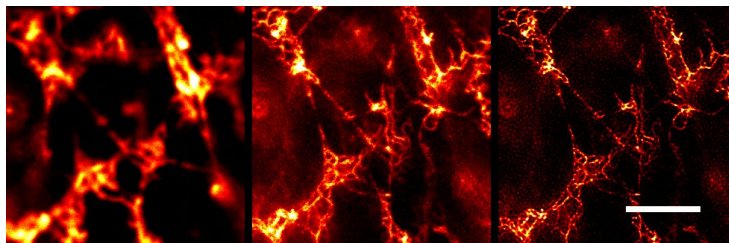


Fig. 4.21 Keratin network in STED microscopy: The same region in a keratin network acquired in confocal (left) and STED (center) modes. Application of the Richardson-Lucy deconvolution algorithm reveals even finer structural details. Scale bar 5 μm

can show. These might be employed by the cell as a regulatory mechanism *in vivo* for the constant remodelling of the cytoskeleton.

4.3 STED-FRET

With reasonable intensities, STED microscopy reveals structures down to 40 nm to 70 nm, depending on sample and system. However, biomolecular interactions take place way below this limit. Accordingly, even dual color STED microscopy may show colocalization where there is no interaction. Ramping up the STED power often is not an option and neither is waiting until a localization-based superresolution approach collects enough data to show finest details. Therefore, it is tempting to combine STED with a different fluorescence technique to elucidate these interactions. The method of choice is Förster Resonance Energy Transfer (FRET), yielding distance information in the subnanometer to 10 nm range, depending on the exact circumstances. This quest has been endeavoured on during the work for this thesis.

4.3.1 FRET

FRET describes the transfer of energy from a donor molecule to an acceptor molecule via dipole-dipole coupling. The process can be modeled within the framework of Coulombic interactions.

An experimentally accessible quantity is the so-called FRET efficiency which describes how probable the decay via the FRET path is with respect to all other paths. Due to the dipole coupling, the FRET Efficiency turns out to depend on the distance to the power of six.

$$E = \frac{k_{\text{FRET}}}{k_{\text{FRET}} + \sum k_i} = \frac{1}{1 + (r/R_0)^6} \quad (4.11)$$

The Förster radius R_0 is about 6 nm for common pairs of organic fluorophores. It crucially depends on the respective orientation of the two dyes, the overlap integral of donor emission and acceptor excitation spectra, and the fluorescence quantum yield of the donor.

4.3.2 Implementation

For STED-FRET measurements, the cross signal output of the time-gating device can be employed. It extracts those signals from the *Red* detector that are issued at the pulse time of the *Orange* or *Blue* channel, depending on the adjustment. The FRET signal is an emission of the acceptor dye that is caused by the excitation of a donor dye. Thus, the corresponding emission is detected upon a donor pulse. Accordingly, it is associated with the cross signal. By this design, donor, acceptor, and FRET signals can be acquired simultaneously.

The STED channels of the microscope are designed for the fluorophores Atto 590 and Atto 647N. Their Förster radius is 7.4 nm. This is a convenient value, as for the typical STED-FRET experiment, a distinction of large distances would be of interest. However, the two dyes are spectrally so close together that the cross-detection of the emission of Atto 590 to the *Red* detector is very high¹². This adds to the cross signal and corrupts the

¹²see section 3.2.3 for details

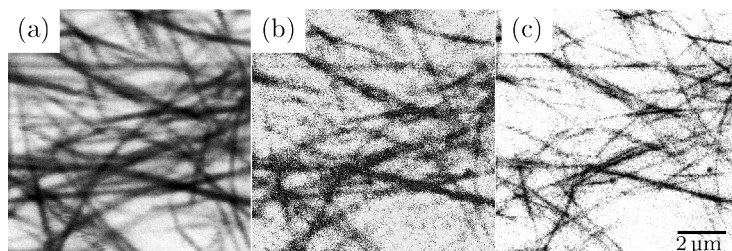


Fig. 4.22 **STED-FRET imaging:** (a) donor, (b) FRET, and (c) acceptor channels of an actin-fascin network in which filaments labeled purely with Atto 532 and filaments labeled purely with Atto 647N were mixed.

FRET measurement. Relative signal intensities are such that a correction for cross detection is not possible.

This limitation is inherent to STED and FRET photophysics. The optimal spectral characteristics of FRET fluorophores are such that the acceptor absorbance has its peak at the long-wavelength tail of the donor emission spectrum. This ensures low cross-detection. For STED microscopy, however, the long-wavelength tails of the emission spectra are employed for STED beams and overlapping absorbance spectra are to be avoided¹³. To allow for donor-STED-FRET, a setup would have to incorporate some more subtle channel separation mechanisms, as will be discussed in section 4.3.3. Hence, on the current microscope, only FRET between the *Blue* and the *Red* channels can be implemented, yielding confocal donor and FRET images and a STED acceptor signal.

As a proof of principle experiment, actin networks were imaged. To prepare samples showing different FRET efficiencies, actin networks were polymerized in two different ways. On the one hand, actin monomers directly labelled with Atto 532 or Atto 647N were mixed in equal amounts and filaments were polymerized. These (hetero) filaments were then polymerized into networks in the presence of crosslinkers. On the other hand,

¹³see section 3.1.1 for an in-depth discussion

single-dye labelled (homo) filaments were mixed and polymerized into networks. Thus, the two networks had the same morphology and the same appearance in regular detection images. Their different composition can be elucidated using the FRET channel, however. In samples consisting of homofilaments FRET had to overcome the interfilament distance while the dyes in heterofilament samples had FRET partners within the filaments. The experiment only being a proof of principle, labelling ratio, stochasticity in mixing, and turnover of crosslinked networks were not taken into account. Fig. 4.22 shows an image of a fascin homofilament network. The successful separation of the high resolution acceptor signal and the confocal FRET signal from the *Red* detector can be observed: Both FRET and acceptor channels originate from the same detector. Still, the FRET channel shows the sample with confocal resolution and the acceptor image is in STED resolution.

To quantify the signal, histograms of the apparent FRET efficiencies of each pixel were generated¹⁴. The apparent FRET efficiency was calculated as the FRET signal divided by the sum of FRET and donor signals,

$$E_{\text{FRET}}^{\text{app}} = \frac{S_{\text{FRET}}}{S_{\text{FRET}} + S_{\text{donor}}}. \quad (4.12)$$

An evaluation including controls is shown in Fig. 4.23¹⁵. It is clearly visible that the two kinds of networks are well distinguishable. Thus, a network in which bundles of a mixture of homofilaments would coexist with bundles of heterofilaments would look homogeneous in the direct channels but the different kinds of bundles could be distinguished by the FRET channel.

The controls show that even with this well-separated FRET pair, cross detection is still an issue (blue). Furthermore, some pulse misassignment occurs, but to a negligible degree (red and green). At a close look, this can

¹⁴No correction for cross detection, wrong timing assignment, or other factors were applied. Therefore, the resulting values are called apparent. To reduce the impact of division by very small values or zero, a threshold was applied to the images, setting the background to *NaN* values.

¹⁵In contrast to the image shown earlier, the data provided here was acquired with an α -actinin network. Differences in crosslinker sizes are neglected here.

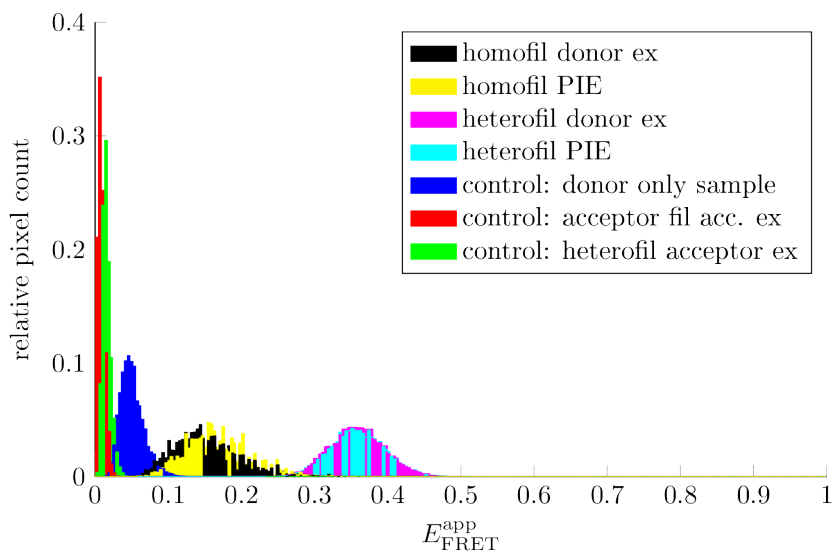


Fig. 4.23 Apparent FRET Efficiency histogram: Homofilament and heterofilament α -actinin networks show distinct peaks in their FRET efficiencies. FRET efficiencies do not significantly differ between donor only and pulsed interleaved excitation. Cross-detection and timing misassignment are present but clearly distinct from the signal.

also be seen in the slightly different distributions of donor only excitation and pulsed interleaved excitation of the samples. The difference between the two is that with PIE, *ExRed* is active. In a perfect measurement, this would not have any influence on the FRET measurement as it occurs at different times. However, due to the small amount of misassigned pulses, some of the direct *Red* detection pulses contribute to the FRET signal. For that reason, PIE distributions are very slightly shifted to higher apparent FRET efficiencies with respect to donor only distributions.

4.3.3 Prerequisites for doubleSTED-FRET

A STED-FRET scheme in which all channels have STED resolution would be desirable to hugely profit from the combination of methods. However, this is hard to realize because the donor emission spectrum should be negligible in the acceptor detection window, and high enough at its STED wavelength. The latter, in turn, should not overlap with the acceptor excitation spectrum in order not to bleach. For this reason, there are two conceivable ways to achieve doubleSTED-FRET.

If the donor had a very low and the acceptor a high lifetime, the signal in the acceptor detection could be distinguished according to lifetime between pure cross detection and the FRET signal of interest. This assignment has been shown to work in Bückers et al. [2011]. FRET decreases the fluorophore lifetime, so the donor needs to have the shorter lifetime.

The second possibility is to use a donor STED wavelength nearer to the emission maximum [Vicidomini et al., 2012], and choose the dyes such that the donor STED wavelength is below the acceptor excitation. Thus a configuration might be found in which the two dyes are spectrally separated far enough and the donor STED does not bleach the acceptor.

Appendix

Evidently, the scope here is too confined to accommodate all details of the setup. However, this chapter supplies materials and methods for the measurements performed and very technical details about alignment procedures and hard- and software. These are not meant for bed-time reading but are supposed to provide a general idea and important key words for further reading.

In-depth information can be found in the internal wiki system. There are two STED wiki projects. The first keeps technical information about the system:

<https://biophysics.wiki.tum.de/--/STED/STEDMasters>.
Information on the scientific projects and about how to use the system can be found here:

<https://biophysics.wiki.tum.de/--/STED/STEDUsers>.

All scans performed on the STED system are saved on the server:

`\\tuphe22-videos.e22.ph.tum.de\files\STEDScans`.

All evaluation data and other files concerning STED resides at

`\\nas.ads.mwn.de\tuph\e22\Groups\BauschGroup\STEDInfo`
Base.

Finally, all software and firmware written is subject to a subversion version control system that can be found under

<http://a-subversion.ph.tum.de:9880/heinrich/>.

<http://a-subversion.ph.tum.de:9880/matlab/trunk/heinrich>.

A read-only version updated with every commit can be found at

`\\tuphe22-rna.e22.ph.tum.de\repositories_read_only\Heinrich`.

A Protocols

A.1 Flow chamber immobilization protocol

Into a flow chamber consisting of double sided tape (model 05338, tesa SE) between a microscope slide and a coverslip of 170 μm thickness, flush the following solutions consecutively.

- 50 μL PAINT buffer A
- 15 μL 1 $\frac{\text{mg}}{\text{mL}}$ biotinylated BSA. Incubate for two minutes.
- 50 μL PAINT buffer A
- 15 μL 1 $\frac{\text{mg}}{\text{mL}}$ streptavidin. Incubate for two minutes.
- 50 μL PAINT buffer A
- 15 μL biotin-modified entities to be bound.
- 2 \times 50 μL PAINT buffer B
- 50 μL imaging buffer
- seal with nail polish

A.2 Gold bead preparation

Gold beads: dilute 1 : 10^3 Fluorescent: dilute 1 : 10^5

- sonicate for approximately 5 min
- put 20 μl of the dilution onto small 170 μm thick coverslide
- evacuate until dry
- On a microscope slide, put fixation solution (from Mowiol antifade fixation protocol) and put coverslide with beads on top.
- let dry for some hours in darkness.

A.3 Mowiol antifade fixation protocol

Add 2.4 g of Mowiol 4-88 to 6 g of glycerol. Stir to mix. Add 6 ml of H_2O and leave at room temperature for several hours. Add 12 ml of 0.2 M Tris-Cl (pH 8.5) and heat to 50 $^\circ\text{C}$ for 10 min with occasional mixing. After the Mowiol dissolves, clarify by centrifugation at 5000 g for 15 min. For fluorescence detection, add DABCO to 2.5 % to reduce fading. Aliquot in airtight

containers and store at -20°C . Stock is stable at room temperature for several weeks after thawing.

from: http://cshprotocols.cshlp.org/content/2006/1/pdb.rec10255.full?text_only=true; September 23, 2013.

A.4 STED pulse timing

Beam powers were set to about $1\ \mu\text{W}$, a lower value was adopted for the STED beams. The ALP seed monitor was connected to the BNC external trigger of the TCSPC laser to synchronize laser and detection¹⁶ Photon counting histograms with these settings have a time resolution of 16 ps.

A.5 Chromatic aberration

The characterization experiment for chromatic aberration was performed by monitoring gold bead reflectance. Using the piezo stage, the gold bead was manoeuvred to defined positions and images were scanned there using beam scanning. The pellicle configuration depended on the position. For a deflection of $\Delta < 10\ \mu\text{m}$, the pellicle between scan head and sample was used. This way, the disturbing reflection of the scan lens does not contribute to the acquired signal (see appendix C.1). For greater deflections, the pellicle between scan head and dichroics was employed. In that case, de-scanning is essential for the signal to hit the detector, and due to the deflection angle, a reflection does not disturb the signal. Images of $5 \times 5\ \mu\text{m}^2$ at pixel step sizes of 20 nm were scanned. For evaluation, the images were fit with a 2D Gaussian and the center position was determined. The scan head had been calibrated with the *ExOrange* beam. Therefore, the aberration of a beam was taken to be the deviation of its PSF center to that of *ExOrange*.

¹⁶For the SymphoTime settings, see the screenshot at `STEDInfoBase\concerningsettingupthesetup\Alignment&Analyses\Pulstiming\Bj"ornPulsessonungen\130422STEDpathsadjusted\SepiaEinstellungenHeinrich_BNC_Trigger_In_Sepia.png`

A.6 Resolution scaling

Experiments were performed on single molecules in order not to introduce convolution of bead size.

40 pM of streptavidin-modified fluorophores were immobilized on the surface using the flow chamber immobilization protocol. The imaging buffer imposed ROXS conditions in order to enable the acquisition enough signal for evaluation.

Images were acquired with an excitation beam power of 3 μ W and varying STED beam powers.

A.7 Detection efficiency

The same sample preparation as for resolution scaling was used. Experiments were performed in absence of STED light.

A.8 PAINT

Used reagents:

- Buffer A: 10 mM Tris-HCl, 100 mM NaCl, 0.05 % Tween-20, pH 7.5
- Buffer B: 5 mM Tris-HCl, 10 mM MgCl₂, 1 mM EDTA, 0.05 % Tween-20, pH 8
- BSA/Biotin, Sigma Aldrich, A8549
- Streptavidin, Invitrogen, S888

Flow chambers were loaded with 20 μ L of a 1 $\frac{\text{mg}}{\text{mL}}$ solution of biotinylated BSA for two minutes, rinsed with 50 μ L PAINT buffer A, loaded with 100 nM streptavidinylated fluorophore, let it bind to the biotins for 2 minutes, and rinsed with 50 μ L PAINT buffer B.

Movies of $5 \times 5 \mu\text{m}^2$ -scans with an exposure time of 50 μ s per pixel and an imaging resolution of 50 $\frac{\text{px}}{\mu\text{m}}$ were acquired.

To evaluate the data, the central part of each frame was averaged to discard border effects and decrease noise. Then, traces of mean signal

B List of dyes that have been used in the system

versus frame number were plotted and with an exponential. The resulting bleach rate was compared to movies with varied acquisition parameters.

To quantify this, the experiments described above were performed on samples in a buffer including 6 mM methyl viologen and 6 mM potassium ascorbate as a ROXS system. Oxygen scavenging was performed by including pyranose-oxidase, catalase, and glucose from aliquotted 1 : 50 stock solutions.

Biotin-tagged DNA origami structures were diluted to about 200 pM and immobilized *via* streptavidin to a biotin-BSA covered surface using the flow chamber immobilization protocol.

For examination, the sample was excited with 3.5 μ W *ExOrange* and for STED acquisition, a STED beam power of 5 mW to 10 mW was applied.

A.9 STED-FRET on actin networks

Actin networks were polymerized with 10 μ M actin and an actin-to-crosslinker ratio of 1 in presence of a simple F-buffer.

For imaging, a coverslip was put into a leakproof chamber and covered with mineral oil. Then, 10 μ L of the actin solution were put onto the coverslip with a pipette, allowing for less than 20 s between mixing of actin and crosslinker and droplet formation.

A.10 DNA filaments

Polymerized DNA filaments from Evi (Dietz Lab) were diluted by a factor of 100 with FOB 20-buffer (Dietz Lab) to approximately 500 pM and flushed into a flow chamber which was sealed with nail polish subsequently. Under the applied salt conditions, the DNA sticks to the surface unspecifically.

B List of dyes that have been used in the system

Dyes that have been used:

Appendix

- *Blue* channel: Atto 488, YO-PRO-1, GFP, Atto 532, Alexa 488
- *Orange* channel: Atto 590, Abberrior Star 580, Atto 594, mCherry, mNeptune. The prior three show a very good performance.
- *Red* channel: Atto 647N, Abberrior Star 635, Atto 655, Alexa 647. The first two are very good. Atto 655 emission is a bit too red-shifted for the system, so single-molecule experiments are impossible. STED with high labeling works, though. Alexa dyes bleach very quickly. Alexa 647 cannot be employed for simultaneous two-colour STED imaging because *STEDOrange* destroys Alexa 647 right away.

Dyes that should work as well but have not been tested yet:

- *Blue* channel: Alexa480, Alexa 500, Atto 495, Rhodamin, FITC, Oregon Green, TOTO1, Adirondack Green 520, Catskill Green 540
- *Orange* channel: Alexa 594, YOYO-1+3, YO-PRO-3, Texas Red, (Nile Red)
- *Red* channel: Atto 647, Cy5.5

C Alignment

C.1 Workflow for daily alignment

1. **startup:** Turn on laser, amplification after 10 minutes. Also start computer and the plugs for all the electric stuff above the setup. Switch on the beam scanner.
2. **alignment of circular polarization:** This step may be necessary only once in one or two weeks for a circular polarization better than -20 dB. Let the laser polarization stabilize for at least half an hour. Remove the objective, turn on and put the rotating polarizer (circular polarization testing tool) in the place of the objective, remove all pellicles from the beam path. Open the `AlignmentTools\VirtOsci_Rolling.vi`. Switch on the STED beam to be aligned. Slightly turn $\lambda/2$ and $\lambda/4$ plates until the peak in the FFT of the photo diode signal at the double turning frequency disappears. Repeat for the other STED beam,

and repeat back and forth until both beams are circularly polarized at the same time.

3. **relative beam alignment - find gold beads:** Put the objective back in place, load a gold bead sample, start the piezo controller, plug in the PMT detector (power and signal), put in both pellicles and remove the 50:50 beam splitter in front of the camera, make sure the x-y scanning AO lines are plugged to the galvo mirrors, start the camera software and the ‘STEDAcquirator’. Scan $20\ \mu\text{m} \times 20\ \mu\text{m}$ @ $5\ \frac{\text{px}}{\mu\text{m}}$, $1\ \frac{\text{ms}}{\text{px}}$ X-Y Scans with *ExOrange* or *ExRed* switched on using the galvo mirrors while looking for the gold beads in the camera software. Move the sample in z until you see fine lines in the camera software. Look for the second-lowest z -point with fine lines (about $30\ \mu\text{m}$ above the lowest) and from there fine-tune z until you see the reflection signal in the scans.
4. **relative beam alignment - find intensities:** Stop scanning without shutting down the program. Plug the AO lines into the piezo and set the calibration in the STEDAcquirator to ‘piezo’. Remove the small pellicle from the beam path and put in the 50:50 beam splitter. Scan with the piezo-calibration on, find the best z position using X-Z Scans. Scan a $2\ \mu\text{m} \times 2\ \mu\text{m}$ @ $50\ \frac{\text{px}}{\mu\text{m}}$, $1\ \frac{\text{ms}}{\text{px}}$ X-Y Scan around a gold bead, adjust the intensity of all beams you want to use so they all yield similar and sensible results (peak 500 cts. to 1000 cts.). Adjust the phase plate positions to form nice donuts if necessary.
5. **relative beam alignment - coalign:** Make linescans around this bead ($2\ \mu\text{m} \times 2\ \mu\text{m} \times 4\ \mu\text{m}$ @ $200\ \frac{\text{px}}{\mu\text{m}} \times 200\ \frac{\text{px}}{\mu\text{m}} \times 100\ \frac{\text{px}}{\mu\text{m}}$, $1\ \frac{\text{ms}}{\text{px}}$). Select one excitation beam to be the reference and sequentially scan linescans of all other excitation beams with it and align them to the reference with one of the beam-walk mirrors. Do the same thing with all detection beam paths to be used by plugging the multimode fiber to the single mode adjustment fiber *via* FC-FC connector. Make sure the pre-fiber pellicle is in and adjust the coupling for the emission spectrum in question (chromatic aberration of coupling lens). Also do the same thing with the STED beams.
6. **get ready:** Plug AO lines back to galvo mirrors, turn STED intensities full on, set calibration in STEDAcquirator back to galvo mirrors.

Measure intensities, remove all pellicles. Put in a fluorescent bead sample for checking performance and then get going.

C.2 Workflow for big alignment

After large jumps of temperature or a long dead time, there is need for a more profound alignment. For completely realigning the beam paths, use the following procedure:

1. **prepare:** Replace the objective with a double-pinhole-tube with a camera at the end (M25-SM1 Adapter - SM1-Iris diaphragm - two 6 inch lens tubes - SM1 Iris diaphragm - webcam). Open the webcam view tool.
2. **check intensities:** Close the lower iris so much that you see rings. Adjust the intensity so as not to get the camera saturated.
3. **mark middle:** Close the upper iris as much as possible and remember the position (can be done with the tool).
4. **align incident beams:** Open the upper iris and close the lower one so that you see rings. If well aligned, the rings are concentric to the position marked before and symmetric in intensity. If this is not so, align using the beam-walk mirrors in the following way. Take one axis of both mirrors, turn the mirror nearer to the iris for centering and the one farther away for making the intensity distribution symmetric. Do this for all excitation beams.
5. **align detection beams:** For detection, you cannot do it this way because the detection lenses have much larger focal lengths than the collimation lenses. So, you need to put another SM1-threaded iris to the detection cage system and use the mirror nearer to the detector to align the iris center to the marked center whilst using the mirror nearer to the objective to align the lower iris of the tube to the marked center. Do this alternatingly until the beam is well aligned. Proceed with the other detections.

C.3 Workflow for alignment from scratch

The best way to build the setup is backwards, from the objective to the collimators. The procedure lined out here has proven to show good results. For each step, the time needed if everything works out well is given. In case the whole alignment does not pose unexpected challenges, it can be completed in 80 h.

Necessary tools are:

- A collimated light source that can be mounted concentrically onto SM1 threads. For example, a fiber output with a 30 mm collimation lens in a cage system works fine.
 - A tube with one iris at each end, with SM1 threads on both ends. This is subsequently called 2-iris tube.
1. Put the objective holder in place. Instead of the objective, install the 2-iris tube and the collimated light source. Check that the beam of the collimated source is centered and emitted coaxially. Align the 45°-mirror beneath to make beam go horizontally. Use two iris diaphragms on the table to check horizontality. 1h
 2. This has not been done up to now, but it would make sense to set up a minimal scanning setup now and adjust all collimators (see protocol ‘Alignment of collimation’ described later). Or if the lab acquires a wave front sensor, maybe they can be set up easily by using that.
 3. Move the collimated source on the table and couple it into the beam path *via* a pellicle after two beam-walk mirrors. Align the beam using the 2-iris-tube with a camera above the tube. 1h
 4. Put two iris diaphragms on the table between pellicle and 45°-mirror. Center them to the beam. 0.5 h
 5. Put a mirror above the objective holder (subsequently called the epi-obj-mirror). This was done using the cage system hanging from the 1.5” posts. However, a mounting strategy including a *z*-moveable translation stage would be more desirable. Align the mirror perpendicularly to the beam and make sure its angle doesn’t change when it is moved up and down. 1h

Appendix

6. Put objective in its place, move the mirror as well as possible into the focal plane using immersion oil. Check whether the reflection is really collimated and coaxial with the incoming beam with the two iris diaphragms. Put two more iris diaphragms behind the pellicle.
2h
7. Put the telescope lens nearer to the objective in place. Check on centering, align z -position by measuring beam widths after the pellicle, the beam needs to be collimated. Check the angle of the lens by its back reflection
3h
8. Put the other telescope lens in place (onto a mount which holds it and also the scan head), align orthogonally with back reflection onto an iris. Put the collimated light source on the 2-iris-tube instead of objective again.
2.5h
9. Set scanhead onto the other side of the holder. Switch it on (otherwise the mirrors are not at their center position). Adjust its adjustable mirror so the beam comes out in 45° .
2h
10. Put the FC-coupled collimation device that came with the scan head into the scan head from the other side using the iris diaphragms for coaxial alignment. Set the objective and the epi-obj-mirror (into focal plane!!) in place again. Additionally, put a pellicle in front of the scan head. Adjust the axial position of the scan head so that the reflection after the pellicle does not move. (alternative approach: check spot on ground glass plate at place of BFP / attention: make sure everything on the scan head is isolated from the table and so on, otherwise some 50 Hz voodoo takes place.)
3h
11. Put the collimated light source on the objective holder again, readjust the mirror in the scan head for the beam to go out horizontally in 45° and put two iris diaphragms there.
0.5 h
12. Put the collimated light source on the other side of the scanhead, and objective and the epi-obj-mirror into the focal plane of the objective. Check that the back reflection is centered at beam center when moving the mirror through the focal region.
0.5 h
13. Set up the dichroics considering the conservation of beam height and the deflection angle of 90° or 20° (using holes or trigonometry: pick

- a point of distance d upbeam of the dichroic. The beam must pass this point at a distance of $d/\sin(20^\circ)$. 4 h
14. Put the PSF-pellicle between the telescope lenses in place. Build the beam path for PSF detection. Put in the PSF-alignment tube lens ($f = 60$ mm). Set the PMT detector in place. Install the small pellicle for PSF detection and add the beam path for the alternative PSF detection. 1.5 h
 15. Polarization cube (PolBS): put in iris diaphragms centered to beam behind the place the cube is supposed to go. Observe the beam with a camera. Put in the PolBS so the beam is not displaced. 0.5 h
 16. Collimation of fiber outlets according to the protocol ‘Alignment of collimation’ described later. 3h
 17. Install *DetRed* dichroic filter (10°), the excitation, detection, and STED beam walk mirrors, checking they are at 45° using holes or trigonometry as before. 5 h
 18. Align brightfield roughly: Use a collimated light source instead of the objective to place the detection lens correctly. Then place the camera in such a way that its sensor is in the focal spot. 1h
 19. Put the excitation and STED collimators in place: Adjust their position such that the beam fits through the iris diaphragms best possible. Make fine adjustment with the beam walk mirrors. 9 h
 20. Install the detection lenses on cage systems and use a cage-loaded iris diaphragm to check the right position. Find the detection fiber mount position roughly by eye. 4 h
 21. Install the sample chamber, checking its horizontal plate is quite perpendicular to the beam with a mirror (silver or gold coated microscope slide). 3 h
 22. Scan a scale on a microscope slide with the piezo and the scan head for calibration of the scan head voltage-to-position factor (separately for x and y , Due do chromatic aberration, use a beam in the medium spectral range, for example *ExOrange*). 1 h

Pre-fiber alignment

Appendix

1. **STED outputs** Install the STED beam walk mirrors and two iris diaphragms each for both channels. 0.5 h
2. Using backwards ray tracing through the diaphragms, coarsely put the cage systems for fiber coupling and half-wave plates in place. Leave enough space for shutters and dimmers. 1 h
3. **supercontinuum output** Put in place beam walk mirrors for exchanging the super-continuum output, pellicle for detection, and dichroics. 1 h
4. Install beam walk mirrors for detection and *ExBlue*. 0.5 h
5. Put in place the beam delay lines for *ExOrange* and *ExRed*, as described in section C.3, making sure that correct timing can be achieved in the range of the delay line. 2 h
6. Install two iris diaphragms per beam and align all six coupling units using backwards ray tracing through the iris diaphragms. 4 h
7. Put in place shutters. Set dimmers to 50% and screw them down in such a way that they yield 50% transmission. 2 h

And lastly, the fine alignment and characterization.

1. **Coarse characterization** Record beam spectra and evaluate coupling efficiencies. 2 h
2. **Collimation fine tuning** Consolidate collimations to yield the z -position in focus for *Ex* and *STED* beams on gold beads (enough light intensity). For *Det* beams, use scale first. It has a larger reflection area, a coarse alignment is possible. Then on gold beads (pure gold mirror on CCD does not work). 12h
3. **Pulse-timing coarse tuning** send beams over to the TCSPC setup and measure time differences (fiber lengths are only exact to 0.2 m) and align delay lines accordingly, keeping in mind the STED efficiency curves. If necessary, re-acquire them. 2 h to 10 h
4. **Circular polarization** The circular polarization needs to turn clockwise if the number of mirrors between phase plate and sample is even and the phase plate pattern looks toward the fiber. If neither condition is met, the polarization needs to be clockwise, too. Otherwise, it needs to be counterclockwise. 5 h

Alignment of collimation The fiber and its collimation lens are mounted on one stage which can be moved around afterwards with the relative position and orientation of fiber and lens remaining constant. This can be either a common mounting plate or a cage system. The fiber should be moveable in three dimensions and the lens should be mounted on a gimbal mount enabling rotation with negligible translation.

This is how it has been done up to now. With a wave front sensor, it might be easier.

- Put the fiber in place. Switch on and put an iris in the diverging beam behind where the lens is going to go. center the iris using a camera and the center of intensity and center tool of the monitoring LabView vi. Close it very much.
- Put a second iris diaphragm in 3m distance. Due to the very small diameter of the first iris, centering is now possible.
- Mount the lens. Adjust it orthogonally as well as possible with a calliper. Position the lens such that it goes centrally through the first iris.
- Collimate the beam by changing the z position of the fiber. Check coaxiality and so on.
- Close the first iris and align the beam to go centrally through the second iris by changing the angle of the lens.

To check a good collimation by gold bead scanning, do scans of $1\ \mu\text{m} \times 1\ \mu\text{m} \times 2\ \mu\text{m}$ @ $50\ \frac{\text{px}}{\mu\text{m}}$, 1 ms. Use the MATLAB[®]script `characterize3DPSF()` to check the ellipticity and axuality of the PSF. If center lines are bent, alter the position of the fiber. If the PSF is elliptical, change the angle of the collimation lens.

Timing of the gating electronics The opto-electronic timing only needs to be aligned after changes in the setup or in the laser. The time delay between optical and electronic pulse that come out of the laser may change when it comes from repair. Then, obviously, only the cable length from the laser to the time gating module needs to be adjusted.

For an optimal time gating alignment, insert a sample containing a highly concentrated solution of dye (tens of micro- to millimolar). Make

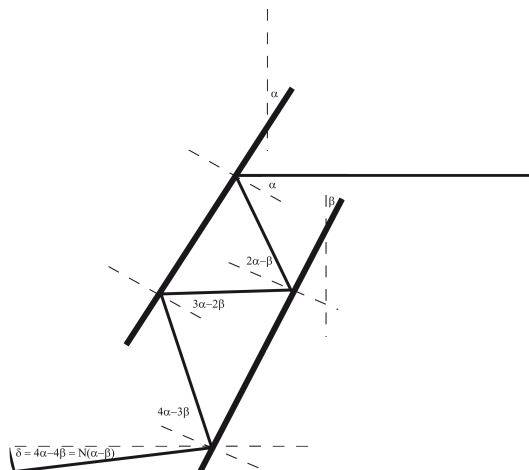


Fig. C.1 Delay Line Alignment: For optimal alignment, the two mirrors stand in a parallel to each other. Then, the spots of reflection are equidistant and the beam direction of the incoming beam is equal to that of the outgoing beam.

sure to focus the beam into the sample and to switch on the corresponding detector. Now, using an oscilloscope with at least 500 MHz timing resolution or with an equally fast logic analyzer, check how the gating and the detector signal are timed with respect to each other. They can be found at the very final AND gate of the circuit. If they do not occur simultaneously, adjust the cable length of the time gating until they are synchronized. Signal transduction in BNC coaxial cables occurs at two thirds the speed of light, so 20 cm of additional cable delay the signal for one nanosecond.

Repeat this procedure for each channel.

Alignment of excitation path delay mirrors The delay mirrors are well aligned if the beam direction of the incident light is the same as that of the ejected light. The sketch in Fig. C.1 shows that the beam comes out in the direction it came in when mirrors are plan parallel. The position of the

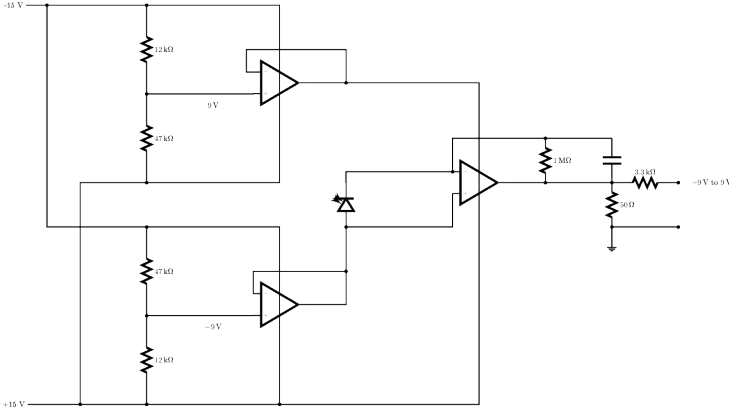


Fig. D.1 Connection diagram for a photo diode circuit: To amplify the signal of a photo diode, an operational amplifier is employed and the amplification resistor is set to 1 MΩ to 10 MΩ.

nth spot on alpha-mirror can be calculated using: $x_n = d (\alpha + n (\alpha - \beta))$ with d being the distance between mirrors. Displacement of the outgoing beam with respect to incoming: $Y_N = N d \sin(\alpha)$. Therefore, mirrors open up when distance of spots increases and *vice versa*.

When aligned well, make sure to put two diaphragms after the construct. After changing the distance, change mirror angles so they get into the diaphragms (then $\alpha_{\text{after}} = \beta_{\text{after}} \neq \alpha_{\text{before}}$). This way, the beam is coupled in again nearly well, and maximizing the coupling efficiency becomes easy from there.

D Hardware

D.1 Intensity photodiode

For detecting photodiode signals, circuits like the one depicted in Fig. D.1 have been brazed. The signal is amplified to voltages in the range fit for the

DAQ board. Operational amplifiers are employed as impedance converters. The output is equipped with a pull-down resistor and a current limiter.

D.2 Circular polarization analyzer

The circular polarizer was assembled by stripping down a very small fan for computers to its bare motor, glueing one side to a cheap linear polarizer and the other side to a post for mounting on the optical table. A simple photo diode (Conrad Electronics) was mounted behind the polarizer. Voltage supply was provided by using operation amplifiers and a stwitch-mode power supply. Detection was assembled similarly to the intensity photodiode.

D.3 Timegating device

The assignment windows the timegating device works with are generated by flip flops (of the SR NAND latch kind). These flip-flops get input rising edges to change their state. Therefore, these two edges need to be generated, one for opening up the window and one for closing it. This is done by varying coaxial cable lengths.

The electronic laser trigger pulse enters the timegating device after having been pre-amplified by a factor of probably two (maybe four). As it is very short, it needs to be broadened before being digitized. To that end, it is split into three, amplified, sent through a diode (which has a widening effect), and reconnected to one pulse by a short time delay. A potentiometer serves to set the offset for digitizing¹⁷. The pulse is digitized to a TTL level and split into three parts that go to BNC connectors. Here, cables of different lengths can be connected to provide varying assignment window timing for the separate channels. After coming back into the timegating device, a part is split out again to set the width of the window with a cable. The latter comes into the device again and both are fed into the flip-flop. The flip-flop output is then combined with the detection pulse of the respective detector with an AND gate. A labelled photograph of the device

¹⁷this needs to be altered when a new laser system is put in place

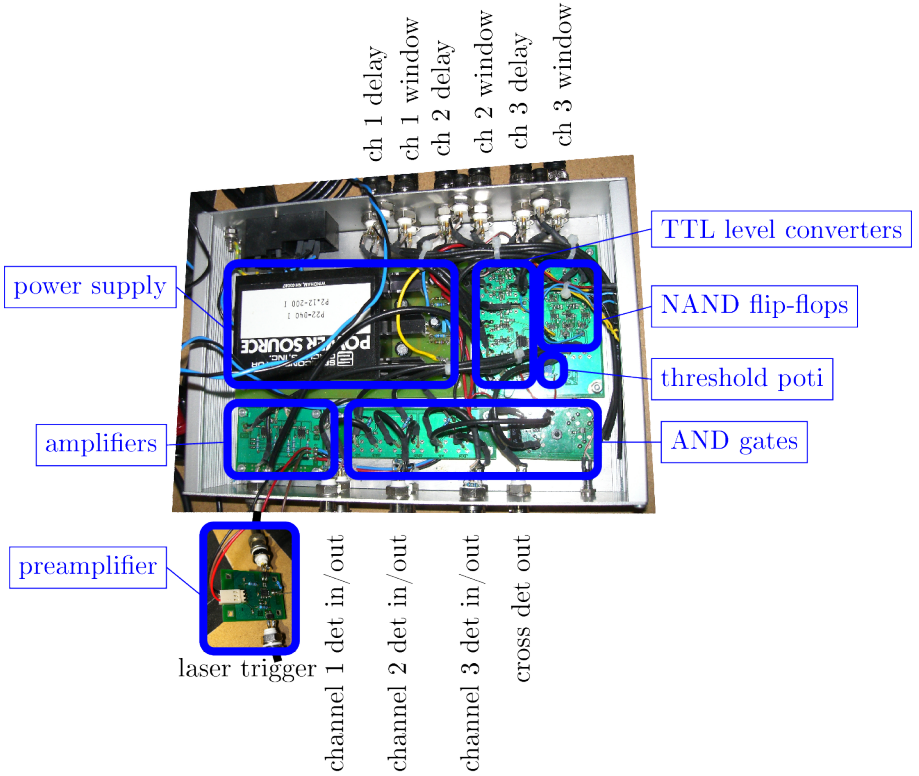


Fig. D.2 Timegating device: The functions of the different parts are labelled. Most often used is the threshold level poti, distinguishing between noise and pulses

can be marvelled at in Fig. D.2. All in- and outputs need to be terminated with 50Ω and gates need to be included to keep the signal from vanishing. The general design of the device is self-made while all the details and the assembly was performed by TUM Elektronikwerkstatt Z72.

D.4 Counter

The counter is based on a CPLD, to be exchanged for an FPGA in near future. The firmware was written in VHDL code. It was important to provide a proper synchronization with the scanning control output. Additionally, the internal synchronization of the asynchronous input pulses was very important for reliable operation of the device [Stein, 2003] (really a good read). Michael Böhmer of the TUM Elektronikwerkstatt is highly acknowledged for guidance and help in this project.

```
STEDInfoBase\concerningsettinguptheshetup\Elektronik\VHDL\110907ctr_double_sync\ctr
```

D.5 Servo microcontroller

The servo dimmers and shutters are controlled by a RS-232 interface of the acquisition computer. Communication is performed with a microcontroller (ATmega 324PA, Atmel), which can be seen in Fig. D.3. The C code for the firmware can be found on the SVN repository in the folder ‘Servo Microcontroller’. It was developed on AVRStudio 4.19 (best use exactly this revision). The compiled firmware was moved to the microcontroller by using the AVR Dragon, employing the JTAG programming interface of the microcontroller. Export works from within the AVRStudio. Many thanks to Michael Böhmer of the TUM Elektronikwerkstatt Z72 for extensive hints, tips and explanations for the development.

Briefly, the servos are controlled by pulse width modulation (PWM). Pulse widths of 1 ms to 2 ms are used to set the servo position. The repetition rate of these pulses is not very important and depends on the time the controller needs for a main loop passage. For each servo, an initial timer value corresponding to the servo position is set when a new pulse

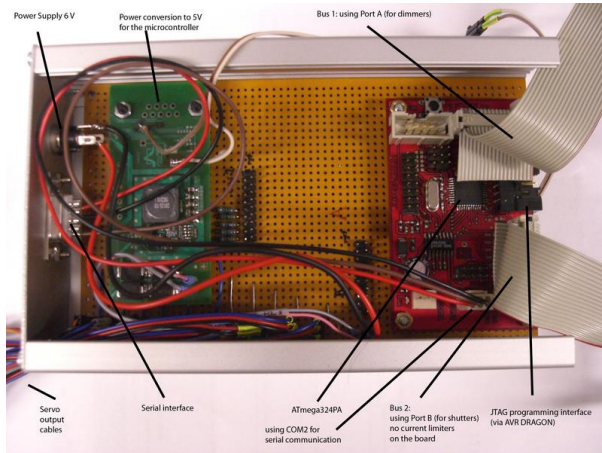


Fig. D.3 **Servo microcontroller**: Interior of the microcontroller device for controlling the eleven servos used for shutting and dimming the beams.

starts. Using a timing interrupt, output levels are set back to low when the interrupt is executed.

Communication is based on handshaking to make sure incomplete commands are detected. Incomplete commands may occur when LabView is too busy. Therefore, every command needs to begin with a '>' character and end with a semicolon. If these signs are found and the command is understood, the answer is given with a preceding 'ok:'. Otherwise, an 'err:' is followed by an error message.

syntax: '>COMMAND-SERVOiD-VALUE'. SERVOiD is the servo to respond (0 to NR_SERVOS-1). VALUE is the value to assign (long int). COMMAND is the command to use, one of the following

- 'MV' - move servo to a new position. Value is the position from min to max with max being about 17620 (do not know the actual number by heart. Check by typing >H;).
- 'T_PWR' - change the time a servo is powered on after getting a

- new position command. Value are steps of about 10ms (depends on main loop duration). 0: always on (default).");
- 'MVMX?' - query maximum value for MV command.
 - 'SH' - set shutter on or off.
 - 'REINIIT' - reinitialize the UART communication interface.
 - 'DEBUG' - set debug mode on or off. With debug mode on, the current status is put out of the debug UART during every loop passage.
 - 'LOGLOOP' - set logging of loop number on or off. Output in the debug UART.
 - 'LOGSERVSTAT' - set logging of servo status on or off.
 - '>H;' - query all commands.

Find more detailed information on the pin assignment on its wiki page:

<https://biophysics.wiki.tum.de/--STED/STED%20Masters/Microcontroller>

E Software

E.1 Acquisition software — usage

E.1.1 Microstage movement

In addition to the 'STEDAcquirator', there is the microstage control program 'MicrostageSteuerung'. With it, you can use a joystick to control the microstages in x, y and z directions. It also takes commands from the 'STEDAcquirator', e.g. for moving the sample away from the objective when the program is stopped or readvances it to the former position when restarting the program. On startup, the program switches to the 'initialization' tab where initialization of the motors and interface takes place. Once initialization is finished, the active tab is automatically switched to 'operation' and the motors respond to input. In case there has been an error on initialization, this switch does not take place. For moving x and y , just move the joystick. There is a normal, slow velocity and a high velocity that is used when you press the 'Fire' button of the joystick. For moving in z , use the 'Schub'-wheel of the joystick or the wheel of the Arcaze device. Both make the microstage move in a certain range that can be set to

10 μm , 100 μm or 1 mm. For moving farther than this range, you can press a button to deactivate movement, which makes moving the wheel trigger a change of the middle position around which the microstage can move. x , y , and z can also be altered just by typing into the corresponding controls or clicking on a position in the control panel presented next.

The current position in x and y is displayed in a control panel. Boundary positions can be defined to save the objective from harm if a more complex sample holder is used. Zooming in and out of the control panel is possible for wide-range and exact positioning. When multi-tile scans are recorded in the acquisition software, downsampled image data is sent to the ‘MicrostageSteuerung’. It is then displayed in the control panel in the positions corresponding to those in the sample. This way, it is possible to directly go back to defined spots in the sample.

E.1.2 General Description of STEDAcquirator

The use of the program is hopefully rather straight forward. Here is a short description anyway.

There are four tabs for different uses: ‘Configuration’, ‘Settings’, ‘Run’ and ‘Surveillance’.

Configuration Tab In ‘Configuration’, you can set the general configuration of the hardware: the physical lines of analog and digital in and output, calibration factors.

Settings Tab ‘Settings’ describes how the microscope is currently used, i.e. which beam paths, colors, dyes are measured. According to these settings, the number of channels and which detectors are read into which channel number are determined. Also, intensity can be measured and other beam parameters set. This information is then stored into the image meta-data.

Run Tab The main functionality of the program takes place in the ‘Run’ tab. Here, you have a visualization frame on the left side, which displays

Appendix

an image or line plots, depending on the type of measurement you are performing. The right side is split into two regions: in the lower part, you have a tab for checking the image acquisition parameters of the current image, telling you how much longer you have to wait for it to be done, what kind of measurement you are doing at the moment, and giving you warnings when a combination of parameters you set is weird. The other tab in the lower part exists for controlling the display of the image. Here you can control contrast and brightness, set colormaps and thresholds, decide which channel is to be shown, have the program display all channels at the same time in an extra window. ‘Show Overflow’ evaluates the pixels that are nearing one count per laser pulse (calculated from timing parameters and the laser repetition rate set in the ‘Configuration’ tab). Those high pixels are exaggerated, i.e. their value is set even higher, so they are clearly discernible in the image. This has no effect on the data saved, however.

The control part on the upper right of the window has one part for Image ‘Acquisition’, and one for looking at already acquired images, ‘Image Archive’. In the archive, you can look at every plane of a saved .ome.tiff image and load the acquisition parameters into the software, so you can manoeuvre from there. This may be helpful when you need to zoom in from an overview image several times and are not patient enough to acquire this overview for the x^{th} time.

In the ‘Acquisition’ tab, you can set the size, speed, and mode of acquisition. Here, you can choose between ‘Conventional HG Style’ control and ‘Leica Style’ control. They represent the same imaging parameters but these are displayed differently. Furthermore, you can select which beam paths shall be active and whether to record a movie, Z-Stack, movie or Z-Stacks, etc.

The last group of tabs holds ‘Acquisition settings’, ‘ROIs’, ‘Save’, ‘Scan Predefs’, and ‘Scan Protocol’. ‘Acquisition settings’ lets you control whether the scan shall always be left-to-right or bidirectional, here you also set whether as a scanning device, the piezo or the galvo scanning mirrors are connected (for a change, you need to replug the AO lines; if scanning by piezo, the galvos need to be short-circuited with 50 Ohms to put them into a center position.) Here, you can also control that the planewise z-stacks shall not be performed by moving the piezo in height

but the microstages, which gives you a wider z -range in one image. With 'cumulative acquisition', you can add up separate scans and with 'scan a pattern', you can leave out some of the points to be scanned which are determined by a binary image that will be prompted for loading during the next scan. This way, you can bleach or activate images and patterns into the sample.

'ROIs' lets you control everything that has a relation to the regions of interest in the image control. When you want to zoom into the scan area or navigate in the sample, you select a tool in the image control (rectangle ROI or tilted rectangle ROI) and draw in the image. As soon as the mouse leaves the image control, the new image parameters are calculated and displayed in the controls. In the tab under discussion, you can tell whether to zoom into the image or merely step sideways, whether a zoom in x, z shall also affect y (via 'clamping' x and y), if the ROI drawn next shall be not done right away but memorized in the protocol, and with 'move sample to the center of the selected area' whether the beam shall be undeflected in the middle of the image. The microstages then move the sample accordingly after every zoom or repositioning in the image. Note that this is not as exact as the beam scanning, so doing this while aligning is not a good idea.

'Save' incorporates the controls to select a saving path and to select whether the current acquisition is to be saved. This, however is also auto-co-triggered with the start-acquisition controls including saving. In the save folder, a folder with the current date is created and a folder with the sample name. In this subfolder, the image is saved as an ome-tiff (www.openmicroscopy.org) with the image name preceded by a millisecond timer-number as the file name.

In the tab 'Scan Predefs', you can define and recall scan acquisition parameters, so you do not have to type often-used acquisition formats. When loading and defining, you can decide separately for many parameters whether they too shall be defined or loaded or whether they shall stay constant.

'Scan Protocol' lets you define, review and start a succession of acquisitions so you do not have to sit there bored into oblivion just for starting one acquisition after another.

Surveillance tab To see whether an error has occurred during execution of the program, have a look at the ‘Surveillance’ tab.

E.1.3 Modes of acquisition

- **X-Y Scan.** Just as the name says, a single-plane scan perpendicular to the optical axis.
- **X-Z Scan.**
- **Y-Z Scan.**
- **Z Stack.** All Z-planes are in memory and saved at once. This limits the number of possible planes, for memory reasons.
- **Z Stack with planewise Acquisition.** Every Z-plane is saved after acquisition. This makes larger stacks possible but costs about 0.1 s to 0.2 s after each plane.
- **X-Y Scan in lowest plane.** For checking Z stack size. Normal X-Y Scan at one z end of the stack.
- **X-Y Scan in highest plane.** For checking Z stack size. Normal X-Y Scan at the other z end of the stack.
- **X-Y + X-Z + Y-Z Scans.** Maybe deprecated. One image which incorporates all three scans. Was kinda cool but not so useful.
- **XYZ Lineplots.** Three line measurements along the axes. Incorporates the possibility to track the bead if it moves due to drift. For beam alignment. May also be useful to evaluate drift: the possibility to log the tracking exists.
- **Single-point timetrace meas.** Introduced for FRET measurements. Acquire an image, go to an interesting spot and look what happens there with a time resolution of tens of kilohertz.

E.2 Acquisition software — design

E.2.1 Some LabView constructs used

Notifiers A notifier is a queue whose reference can be spread out to different parts of a program (or indeed shared between different programs) and once something is written on it, a notification of a change and the corresponding information can be read in any other part of the program.

Field Global Variables A field global variable (FGV) is a SubVI that makes the functionality of a global variable accessible to LabView in a performance efficient way (as the normal global variable does not). Typedefined actions can perform different kinds of reading and writing to the data.

E.2.2 ‘STEDAcquirator.vi’

There are six loops running in parallel: The user input loop, the work loop, the acquisition loop and the display loop.

At the moment, there are about 450 SubVIs which are saved in subfolders organized to the region they belong. So there are subfolders for every loop. VIs that are placed in SubVIs reside in folders named the same as those. FGVs are saved in a separate subfolder and below that ordered according to functionality. Some VIs are called several times from different places in the program. They are in a subfolder called ‘OftenCalled’. Also, there are folders for type definitions, mainly enums selecting options of actions, for notifiers, user-defined events and for the control of microstages.

The user loop This incorporates one event structure which has the timeout set to zero. Any reaction the program should do upon a user input corresponds to an event case of this structure. The usual procedure in the events is to read the control values and write it into an FGV, and where appropriate throw some user-defined event. To initialize the values of the FGVs at startup of the program, the value of every control is read by a property node and set again using ‘value (signalling)’ to fill the queue of the event structure.

The work loop The work loop has been created to save time in the other loops. So whenever there is something to be calculated, this should be done here. Again, the loop contains an event structure. The structure responds to user-defined events which are triggered at any place in the program. In a rebuild it would make sense to replace this construction with a queue, so the data to be calculated could be included to the triggering process and triggering several times without regard to whether the execution is done

would be possible. For now, the data is send to and read from FGVs. In particular the intensity measurement suffers from this approach and a new trigger can only occur when the last work loop cycle is done.

Tasks performed here are file access (reading as well as writing `ome.tiffs`), the processing of ROIs drawn into the image control, the measuring of beam intensities and the calculation of new offsets when doing a line-plot measurement and tracking the bead.

The acquisition loop As the name suggests, everything concerned with acquisition is done here. The loop contains a case structure which distinguishes different ‘acquisition tasks’. An FGV holds the current task, which can be ‘idle’, ‘initialize’, ‘read’ or ‘stop’. The natural thing to do is to idle. When the user hits a button to start acquisition, the user loop sets the current acquisition task to ‘initialize’. At the end of initialization, the task is set to ‘read’ and once the image has been acquired completely, or the user hits ‘stop’, the current task is changed again, and so on.

The display loop Here, both of the two introduced methods of running a loop are used. For one, there are things that need to be set once when there has been a change in values. This is handled by an event structure sensitive to user-defined ‘display events’. On the other hand, some elements need to be refreshed constantly, an example being the image control. For this, a case structure dissecting the display tasks ‘Display Acq Image’, ‘Display All Channels’, ‘Display Linescans’, ‘Display Timetrace’ and ‘Display LoadedImage’ is present in the display loop as well. They all visualize the recorded data in a different way. Finally, the loop incorporates controls that should be actualized always, no matter what options the user has selected.

The parallel edit loop For displaying VIs that are supposed to run in parallel, this loop has been devised. From here, you can edit predefined settings, scan protocols, display all channels at the same time, etc. Simultaneously, the display still works normally.

The External Interface input Loop In this loop, external interfaces such as the Arcaze board are read out.

E.2.3 ‘MicrostageSteuerung.vi’

With its four parallel loops, the ‘MicrostageSteuerung.vi’ is designed very similarly to the ‘STEDAcquirator’.

On calling the VI, there is the possibility to transmit three more arguments: notifiers for xy movement, for z movement, for triggering a shutdown of the program, and for the transmission of overview image data. This is used when the ‘STEDAcquirator’ calls it. Therefore, the ‘STEDAcquirator’ can induce microstage movement. On shutdown of the ‘STEDAcquirator’, the positions are read via the FGV, the Z notifier makes the sample be moved away from the objective and then the shutdown-notifier is triggered. After a multi-tile scan, the ‘STEDAcquirator’ transmits the data for it to be displayed in the position panel of the ‘MicrostageSteuerung’.

E.3 ImageJ plugins

Plugins for ImageJ have been developed. See the respective subversion repository for details.

E.4 Spectraviewer and other matlab scripts

There are also a few scripts for MATLAB[®], including a spectraviewer to show multiple fluorophore spectra and beam path transmittances simultaneously. See the ‘Heinrich’ directory on the MATLAB[®] subversion repository.

E.5 OME-TIFF dll

At the time of program design, there was a java library and MATLAB[®] code to save .ome.tif files. Neither of them was well fit for introduction into a LabView program. Therefore, a C++ dll needed to be written that saves tif images in an .ome.tif compatible way.

Appendix

Originally, loci's bio-formats should have been used, but as they are written in Java, the way to go would have been to build a C++ dll via java native interface (JVM, JNI, Jace) and LabVIEW could not access this dll nor a wrapper dll.

So, this dll has been created to directly write ome-tiff files.

General structure: This DLL provides a class, XMLAttributes, in which all meta data of the image is stored. Upon call of a new instance, a global variable of this class is created, called MetaData. Global functions exist to make MetaData's methos accessible to the caller (LabVIEW), and if necessary to convert data types from LabVIEW-compatible to the later used types. Metadata is written, and in the end, WriteImage is called which writes the image data into a tiff file using LibTIFF¹⁸, and into its 'imageDescription' tag, the XML header for the OME-TIFF data using XmlNode¹⁹.

For detailed information on OME-TIFF, see <http://ome.xml.org/wiki/OmeTiffSpec> and linked sites.

The used OME-TIFF schema is : 2010-06

¹⁸C++ dll for writing tiff files

¹⁹another open source library

F Definitions

The following list shows definitions of abbreviations and acronyms given in the text as well as where they are made.

STED	stimulated emission depletion	S.1-1.0.0
PSF	point spread function	S.8-2.1.0
NA	numerical aperture	S.9-2.1.1
FWHM	full width at half maximum	S.9-2.1.1
LUMO	lowest unoccupied molecular orbital	S.12-2.2.0
HOMO	highest occupied molecular orbital	S.12-2.2.0
ROXS	reducing and oxidizing system	S.15-2.2.0
CLSM	confocal laser scanning microscope	S.16-2.3.0
OD	optical density	S.38-3.1.1
ALEX	alternating excitation	S.39-3.1.2
PIE	pulsed interleaved excitation	S.39-3.1.2
DAQ	data acquisition	S.45-3.1.4
APD	avalanche photo diodes	S.45-3.1.4
CPLD	complex programmable logic device	S.45-3.1.4
SNR	signal to noise ratio	S.49-3.2.2
DNA-PAIN	Protein Accumulation for Imaging in Nanoscale Topography using DNA oligomers	S.78-4.1.2
LCV	<i>Legionella</i> containing vacuole	S.92-4.2.1
LegG1	<i>Legionella</i> eukaryotic gene G1	S.92-4.2.1
LIBLI	Lewy-body like inclusion	S.96-4.2.2
FRET	Förster Resonance Energy Transfer	S.104-4.3.0
PWM	pulse width modulation	S.128-D.5
FGV	field global variable	S.134-E.2

List of Figures

2.1	Schematic drawing of an infinity corrected wide field microscope	5
2.2	Diffraction and lens	7
2.3	Airy patterns at minimal distances of various resolution criteria	10
2.4	Jablonski diagram	13
2.5	Schematic drawing of a confocal microscope	17
2.6	Working principle of STED microscopy	21
2.7	Depletion pattern generation	23
3.1	STED Setup	32
3.2	Absorption and Emission Spectra of the design dyes	34
3.3	ALP laser source	35
3.4	Dichroic mirrors	36
3.5	Spectral transmittivity of beam paths	37
3.6	Time-gating schematic	40
3.7	Beam path schematic	42
3.8	Pulse timing of input beams	47
3.9	STED efficiency and pulse delay	48
3.10	Polarization and depletion pattern	51
3.11	Detector Synchronization	54
3.12	Detector Pulse Distribution	55
3.13	Pulse propagation velocity	56
3.14	Time Gating	57
3.15	Crosstalk without and with time-gating	59
3.16	Chromatic Aberration	61
3.17	Chromatic Aberration - wavelength dependence	62

List of Figures

3.18	Resolution Scaling	64
3.19	Saturation Intensity Atto 647N	67
3.20	Donut form factor	68
3.21	Detection efficiency	70
4.1	STED imaging of triple labeled fixed cells	76
4.2	DNA monomer design	77
4.3	Polymeric DNA nanostructure	78
4.4	Evaluation of orientation	79
4.5	Bleach rate versus exposure time and imaging resolution	81
4.6	Bleach rate versus beam powers in PAINT buffer	82
4.7	Bleach rate versus beam powers in ROXS PAINT buffer	83
4.8	Signal and background for single molecules	85
4.9	Transient binding of imager strands	88
4.10	Histogram of imager on-times	89
4.11	PAINT result	90
4.12	PAINT result	91
4.13	<i>Legionella</i> in macrophages	94
4.14	Differentiated SH-SY5Y cell expressing GFP-tagged α -synuclein - comparison of acquisition modes	96
4.15	Cells in medium containing α -synuclein monomers	97
4.16	Void vesicles in monomer-induced samples	98
4.17	Seed-treated cells	99
4.18	Seed-induced samples	100
4.19	Differentiated SHSY-5Y cells overexpressing GFP tagged α -synuclein exposed to rotenone	101
4.20	Human Lewy bodies	102
4.21	Keratin network in STED microscopy	104
4.22	STED-FRET imaging	106
4.23	Apparent FRET Efficiency histogram	108
C.1	Delay Line Alignment	124
D.1	Connection diagram for a photo diode circuit	125
D.2	Timegating device	127

D.3 Servo microconroller 129

Appendix A

Bibliography

- Ernst Abbe. Beiträge zur Theorie des Mikroskops und der mikroskopischen Wahrnehmung. *Archiv für mikroskopische Anatomie*, 9:413–482, 1873.
- AHF Analysetechnik. Tübingen, Germany, www.ahf.de.
- M. A. Alim. Tubulin Seeds α -Synuclein Fibril Formation. *Journal of Biological Chemistry*, 277(3):2112–2117, 2001.
- Atmel. San Jose, CA, USA, www.atmel.com.
- Atto Tec GmbH. Siegen, Germany, www.atto-tec.de.
- E. Betzig, G. H. Patterson, R. Sougrat, O. W. Lindwasser, S. Olenych, J. S. Bonifacino, M. W. Davidson, J. Lippincott-Schwartz, and H. F. Hess. Imaging intracellular fluorescent proteins at nanometer resolution. *Science*, 313(5793):1642–1645, 2006.
- P. Bianchini, B. Harke, S. Galiani, G. Vicidomini, and A. Diaspro. Single-wavelength two-photon excitation-stimulated emission depletion (SW2PE-STED) superresolution imaging. *Proceedings of the National Academy of Sciences*, 109(17):6390–6393, 2012.
- Nancy M. Bonini and Benoit I. Giasson. Snaring the Function of α -Synuclein. *Cell*, 123(3):359–361, 2005.
- Max Born and Emil Wolf. *Principles of Optics*, page 490. Pergamon Press, Oxford, 6 edition, 1993a.

Appendix A Bibliography

- Max Born and Emil Wolf. *Principles of Optics*, page 490. Pergamon Press, Oxford, 6 edition, 1993b.
- I.N Bronstein, K.A Samedjajew, G. Musiol, and H. Mühlig. *Taschenbuch der Mathematik*, page 1090. Verlag Harri Deutsch, Frankfurt am Main, 5 edition, 2001.
- Johanna Bückers, Dominik Wildanger, Giuseppe Vicidomini, Lars Kasttrup, and S. W. Hell. Simultaneous multi-lifetime multi-color STED imaging for colocalization analyses. *Optics Express*, 19(4):3130–3143, 2011.
- Carlos Ernesto Castro, Fabian Kilchherr, Do-Nyun Kim, Enrique Lin Shiao, Tobias Wauer, Philipp Wortmann, Mark Bathe, and Hendrik Dietz. A primer to scaffolded DNA origami. *Nature Methods*, 8(3):221–229, 2011.
- Sreeganga Chandra, Gilbert Gallardo, Rafael Fernández-Chacón, Oliver M. Schlüter, and Thomas C. Südhof. α -Synuclein Cooperates with CSP α in Preventing Neurodegeneration. *Cell*, 123(3):383–396, 2005.
- Andriy Chmyrov, Jan Keller, Tim Grotjohann, Michael Ratz, Elisa d’Este, Stefan Jakobs, Christian Eggeling, and Stefan W. Hell. Nanoscopy with more than 100,000 ‘doughnuts’. *Nature Methods*, 2013.
- p.R Clarke and C. Zhang. Spatial and temporal coordination of mitosis by Ran GTPase. *Nat Rev Mol Cell Biol*, 9(6):464–477, 2008.
- Conrad Electronics. München, Germany, www.conrad.de.
- Thomas Dertinger, Victor Pacheco, Iris von der Hocht, Rudolf Hartmann, Ingo Gregor, and Jörg Enderlein. Two-Focus Fluorescence Correlation Spectroscopy: A New Tool for Accurate and Absolute Diffusion Measurements. *ChemPhysChem*, 8(3):433–443, 2007.
- P. S. Dittrich and P. Schwille. Photobleaching and stabilization of fluorophores used for single-molecule analysis with one- and two-photon excitation. *Appl. Phys. B - Lasers and Optics*, 73(8):829–837, 2001.

- ECDC. *Legionnaires disease in Europe, 2011*, page 1. European Centre for Disease Prevention and Control, Stockholm, 2013.
- C. Eggeling, J. Widengren, L. Brand, J. Schaffer, S. Felekyan, and C. A.M. Seidel. Analysis of photobleaching in single-molecule multicolor excitation and forster resonance energy transfer measurement. *J. Phys. Chem. A*, 110(9):2979–2995, 2006.
- Fianium Ltd. Southampton, United Kingdom, www.fianium.com.
- Fabian Göttfert, Christian A. Wurm, Veronika Mueller, Sebastian Berning, Volker C. Cordes, Alf Honigmann, and Stefan W. Hell. Coaligned Dual-Channel STED Nanoscopy and Molecular Diffusion Analysis at 20 nm Resolution. *Biophysical Journal*, 105(1):L01–L03, 2013.
- Rudolf Gross. *Experimentalphysik III - Optik und Quantenphänomene*, chapter 7, pages 317–341. Garching, 2003.
- L.M. Hampton, L.A. Hicks, and L.E. Garrison. Legionellosis — united states, 2000–2009. *Morbidity and Mortality Weekly Report, Centers of Disease Control and Prevention*, 2011.
- Benjamin Harke, Chaitanya K. Ullal, Jan Keller, and Stefan W. Hell. Resolution scaling in STED microscopy. *Optics Express*, 16(6):4154–4162, 2008.
- Eugene Hecht. *Optics*, page 243. Addison Wesley, San Francisco, 4 edition, 2002a. ISBN 0-321-18878-0.
- Eugene Hecht. *Optics*, chapter 10.2.5, page 467 ff. Addison Wesley, San Francisco, 4 edition, 2002b. ISBN 0-321-18878-0.
- Iddo Heller, Gerrit Sitters, Onno D. Broekmans, Géraldine Farge, Carolin Menges, Wolfgang Wende, Stefan W. Hell, Erwin J. G. Peterman, and Gijs J. L. Wuite. STED nanoscopy combined with optical tweezers reveals protein dynamics on densely covered DNA. *Nature Methods*, 10(9): 910–916, 2013.

Appendix A Bibliography

- Invitrogen, Life Technologies. Darmstadt, Germans, www.lifetechnologies.com.
- Jennings, Phoebe C., Guy C. Cox, Leigh G. Monahan, and Elizabeth J. Harry. Super-resolution imaging of the bacterial cytokinetic protein FtsZ. *Micron*, 42(4):336–341, 2011.
- Ralf Jungmann, Christian Steinhauer, Max Scheible, Anton Kuzyk, Philip Tinnefeld, and Friedrich C. Simmel. Single-Molecule Kinetics and Super-Resolution Microscopy by Fluorescence Imaging of Transient Binding on DNA Origami. *Nano Letters*, 10(11):4756–4761, 2010.
- Heuner K. and M. Swanson. *Legionella: Molecular Microbiology*. Caister Academic Press, 2008. ISBN 978-1-904455-26-4.
- Achillefs N. Kapanidis, Ted A. Laurence, Nam Ki Lee, Emmanuel Margeat, Xiangxu Kong, and Shimon Weiss. Alternating-Laser Excitation of Single Molecules. *Accounts of Chemical Research*, 38(7):523–533, 2005.
- Robert Kasper, Benjamin Harke, Carsten Forthmann, Philip Tinnefeld, Stefan W. Hell, and Markus Sauer. Single-Molecule STED Microscopy with Photostable Organic Fluorophores. *Small*, 6(13):1379–1384, 2010.
- Jona Kayser, Heinrich Grabmayr, Markus Harasim, Harald Herrmann, and Andreas R. Bausch. Assembly kinetics determine the structure of keratin networks. *Soft Matter*, 8(34):8873, 2012.
- T. A. Klar and S. W. Hell. Subdiffraction resolution in far-field fluorescence microscopy. *Optics Letters*, 24(14):954–956, 1999.
- Jürgen Kleine-Vehn, Krzysztof Wabnick, Alexandre Martinière, Łukasz Łangowski, Katrin Willig, Satoshi Naramoto, Johannes Leitner, Hirokazu Tanaka, Stefan Jakobs, Stéphanie Robert, Christian Luschnig, Willy Govaerts, Stefan W Hell, John Runions, and Jiří Friml. Recycling, clustering, and endocytosis jointly maintain PIN auxin carrier polarity at the plasma membrane. *Molecular Systems Biology*, 7, 2011.

- August Köhler. Gedanken zu einem neuen Beleuchtungsverfahren für mikrophotographische Zwecke. *Zeitschrift für wissenschaftliche Mikroskopie*, 10:433–440, 1893.
- LaserComponents. Olching, Germany, www.lasercomponents.de.
- Lana Lau, Yin Loon Lee, Steffen J. Sahl, Tim Stearns, and W.E Moerner. STED Microscopy with Optimized Labeling Density Reveals 9-Fold Arrangement of a Centriole Protein. *Biophysical Journal*, 102(12):2926–2935, 2012.
- LeCroy. Chestnut Ridge, NY, USA, www.teledynelecroy.com.
- Frank J.S Lee, Fang Liu, Zdenek B. Pristupa, and Hyman B. Niznik. Direct binding and functional coupling of α -synuclein to the dopamine transporters accelerate dopamine-induced apoptosis. *FASEB J.*, 15(6):916–927, 2001.
- Leica Microsystems. Heidelberg/Wetzlar, Germany, www.leica-microsystems.de.
- Marcel Leutenegger. Fast focus field calculations. *Optics Express*, 14(23):1277–1284, 2006.
- Marcel Leutenegger, Christian Eggeling, and Stefan W. Hell. Analytical description of STED microscopy performance. *Optics Express*, 18(25):26417–26429, 2010.
- Marcel Leutenegger, Christian Ringemann, Theo Lasser, S. W. Hell, and Christian Eggeling. Fluorescence correlation spectroscopy with a total internal reflection fluorescence STED microscope (TIRF-STED-FCS). *Optics Express*, 20(5):5243–5263, 2012.
- P.H Lissberger and W.L Wilcock. Properties of All-Dielectric Interference Filters. *J. opt. soc. USA*, 49(2):121–130, 1959.
- I. H. Malitson. Interspecimen Comparison of the Refractive Index of Fused Silica. *Journal of the optical society of America*, 55(10):1205–1209, 1965.

Appendix A Bibliography

Marvin Minsky. Microscopy apparatus, 1961.

Barbara K. Müller, Evgeny Zaychikov, Christoph Bräuchle, and Don C. Lamb. Pulsed Interleaved Excitation. *Biophysical Journal*, 89(5):3508–3522, 2005.

Tobias Müller, Christian Schumann, and Annette Kraegeloh. STED Microscopy and its Applications: New Insights into Cellular Processes on the Nanoscale. *ChemPhysChem*, 13(8):1986–2000, 2012.

National Instruments. München, Germany, www.ni.com.

H. Nyquist. Certain topics in telegraph transmission theory. *Proceedings of the IEEE*, 90(2):280–305, 2002.

A. Penzkofer, W. Falkenstein, and W. Kaiser. Vibronic Relaxation in the S1 State of Rhodamine Dye Solutions. *Chemical Physics Letters*, 44(1): 82–87, 1976.

Perkin Elmer. Waltham, MA, USA, www.perkinelmer.com.

Physik Instrumente. Karlsruhe, Germany, www.physikinstrumente.de.

PicoQuant GmbH. Berlin, Germany, www.picoquant.com.

Rayleigh. *Collected Papers*, volume 3. Cambridge University Press, Cambridge, 1902.

Eva Rothmeier, Gudrun Pfaffinger, Christine Hoffmann, Christopher F. Harrison, Heinrich Grabmayr, Urska Repnik, Mandy Hannemann, Stefan Wölke, Andreas Bausch, Gareth Griffiths, Annette Müller-Taubenberger, Aymelt Itzen, Hubert Hilbi, and Tomoko Kubori. Activation of Ran GTPase by a Legionella Effector Promotes Microtubule Polymerization, Pathogen Vacuole Motility and Infection. *PLoS Pathogens*, 9(9):e1003598, 2013.

- M. J. Rust, M. Bates, and X. W. Zhuang. Sub-diffraction-limit imaging by stochastic optical reconstruction microscopy (STORM). *Nature Methods*, 3(10):793–795, 2006.
- Roman Schmidt, Christian A. Wurm, Annedore Punge, Alexander Egner, Stefan Jakobs, and Stefan W. Hell. Mitochondrial Cristae Revealed with Focused Light. *Nano Letters*, 9(6):2508–2510, 2009.
- C. J. R. Sheppard. Depth of Field in Optical Microscopy. *Journal of Microscopy*, 149(1):73–75, 1988.
- Charles Shillaber. *Photomicrography in Theory and Practice*, page 255. John Wiley and Sons, New York, 1944.
- Vitor L. Sousa, Serena Bellani, Maila Giannandrea, Malikmohamed Yousuf, Flavia Valtorta, Jacopo Meldolesi, and Evelina Chie. α -Synuclein and Its A30P Mutant Affect Actin Cytoskeletal Structure and Dynamics. *Molecular Biology of the Cell*, 20:3725–3739, 2009.
- Carroll Mason Sparrow. On spectroscopic resolving power. *Astrophys. J.*, (44):76–86, 1916.
- Mike Stein. Crossing the abyss: asynchronous signals in a synchronous world. *EDN Network*, 2003. URL www.edn.com.
- M. Swanson and B. Hammer. Legionella pneumophila pathogenesis: a fateful journey from amoebae to macrophages. *Annu Rev Microbiol*, 54: 567–613, 2000.
- Marko Swoboda, Jörg Henig, Hsin-Mei Cheng, Dagmar Brugger, Dietmar Haltrich, Nicolas Plumeré, and Michael Schlierf. Enzymatic Oxygen Scavenging for Photostability without pH Drop in Single-Molecule Experiments. *ACS Nano*, 6(7):6364–6369, 2012.
- tesa SE. Hamburg, Germany, www.tesa.com.
- Till Photonics. Martinsried, Germany, www.till-photonics.com.
- Time Magazine. The philadelphia killer. *Time Magazine*, 1976.

Appendix A Bibliography

- Tomasz S. Tkaczyk. *Field guide to microscopy*, volume 13 of *SPIE field guides*, page 41. SPIE Press, Bellingham and Wash, 2010. ISBN 0819472468.
- TrinkwV. *Bundesgesetzblatt 1*, page 2562. Federal Republic of Germany, 2001.
- Trust. Kleve, Germany, www.trust.com.
- Nicholas J. Turro. *Modern Molecular Photochemistry*, page 35. Benjamin/Cummings Publishing Co., 1978. ISBN 0-805309354-4.
- Vladimir N. Uversky. Neuropathology, biochemistry, and biophysics of α -synuclein aggregation. *Journal of Neurochemistry*, 0(0):070710052154012-???, 2007.
- G. Vicidomini, Gael Moneron, Christian Eggeling, Eva Rittweger, and S. W. Hell. STED with wavelengths closer to the emission maximum. *Optics Express*, 20(5):5225–5236, 2012.
- Jan Vogelsang, Robert Kasper, Christian Steinhauer, Britta Person, Mike Heilemann, Markus Sauer, and Philip Tinnefeld. A Reducing and Oxidizing System Minimizes Photobleaching and Blinking of Fluorescent Dyes. *Angewandte Chemie International Edition*, 47(29):5465–5469, 2008.
- Christophe Wersinger and Anita Sidhu. Attenuation of dopamine transporter activity by α -synuclein. *Neuroscience Letters*, 340(3):189–192, 2003.
- V. Westphal, S. O. Rizzoli, M. A. Lauterbach, D. Kamin, R. Jahn, and S. W. Hell. Video-Rate Far-Field Optical Nanoscopy Dissects Synaptic Vesicle Movement. *Science*, 320(5873):246–249, 2008.
- Dominik Wildanger, Eva Rittweger, Lars Kastrop, and Stefan W. Hell. STED microscopy with a supercontinuum laser source. *Optics Express*, 16(13):9614–9621, 2008.
- Dmitry Yudin and Mike Fainzilber. Ran on tracks—cytoplasmic roles for a nuclear regulator. *Journal of cell science*, 122(5):587–593, 2009.

Jianping Zheng, Jens J. Birktoft, Yi Chen, Tong Wang, Ruojie Sha, Pamela E. Constantinou, Stephan L. Ginell, Chengde Mao, and Nadrian C. Seeman. From molecular to macroscopic via the rational design of a self-assembled 3D DNA crystal. *Nature*, 461(7260):74–77, 2009.

Index

Legionella containing vacuole, 92
Legionella eukaryotic gene G1,
92

Airy disc, 8

Airy pattern, 8

ALEX, 39

alternating excitation, 39

APD, 45

avalanche photo diodes, 45

CLSM, 16

complex programmable logic
device, 45

confocal laser scanning
microscope, 16

Confocal PSF, 18

CPLD, 45

DAQ, 45

data acquisition, 45

DNA-PAINT, 78

Förster Resonance Energy
Transfer, 104

FGV, 135

field global variable, 135

flip-flop, 40

FRET, 104

full width at half maximum, 9
FWHM, 9

highest occupied molecular
orbital, 12

HOMO, 12

LCV, 92

LegG1, 92

Lewy-body like inclusion, 96

LIBLI, 96

lowest unoccupied molecular
orbital, 12

LUMO, 12

NA, 9

numerical aperture, 9

OD, 38

optical density, 38

PIE, 39

point spread function, 8

points accumulation for imaging
in nanoscale

INDEX

- topography using DNA oligomers, 78
- PSF, 8
- pulse width modulation, 128
- pulsed interleaved excitation, 39
- PWM, 128

- Rayleigh criterion, 8

- reducing and oxidizing system, 15
- ROXS, 15

- signal to noise ratio, 50
- SNR, 50
- Sparrow criterion, 8, 18
- STED, 1
- stimulated emission depletion, 1